Rotating Rayleigh-Bénard convection in uniform and non-uniform spherical shells

by

Jeffrey Nederend

to obtain the degree of Master of Science
at the Delft University of Technology,
to be defended publicly on Friday October 23, 2020 at 10:00 AM.

Student number:	4401492	
Project duration:	January 27, 2020 – October 23, 2020	
Thesis committee:	ir. M. Rovira-Navarro,	TU Delft, supervisor
	Dr. T. Pestana,	TU Delft, supervisor
	Dr. ir. W. van der Wal,	TU Delft
	Prof. dr. L.L.A. Vermeersen,	TU Delft
	Prof. dr. S. Hickel,	TU Delft

Keywords: Bénard convection, rotating flows, geophysical and geological flows
Cover: Cut-out, not unlike a sliced avocado, of a meridionally deformed subsurface ocean representing Enceladus undergoing vigorous thermal convection and strong rotation

TU Delft Delft University of Technology

Acknowledgements

The study of Geophysical Fluid Dynamics encapsulates a wide variety of research fields and finds many applications in planetary sciences. It is the harmony between numerical modelling and the physical applications to understand how a system works, that has drawn me to pursue this study. In this work, we take a look at a very small and distant, yet astronomically nearby, object that draws the attention as one of the most interesting bodies in our solar system where potentially life exists today.

All of this work was done in excellent guidance by my supervisors Marc Rovira-Navarro and Tiago Pestana. I am very grateful to your time and expertise that enabled me to better understand the dynamical system of Enceladus and aid me in developing and running the numerical tool on the (super) computer clusters. Your involvement in this project and readiness to discuss any hiccups is much appreciated. It was a genuine pleasure to have worked with you both during this time. Thanks to you both!

I further would like to thank Wouter van der Wal for bringing me into contact with Marc and for his role as supervisor in this study. I would also like to thank my friend Aditya who since the first day of this two-year Master provided friendship and a healthy dose of study competition for our time here in Delft. Also thanks to Stef Lhermitte for our side project on modelling Antarctica's temporal evolution of thinning ice shelves. This helped me greatly in preparing for my final thesis.

Finally, I close my acknowledgements by thanking my family who have always fully supported me during my studies.

Jeffrey Nederend
Delft, October 2020

Summary

From Jupiter's atmosphere to Earth's core, thermal convection plays an important role in the morphology and evolution of planets and moons. To study these objects, it is essential to combine observations with numerical models. In this thesis we adapt an existing numerical tool to study thermal convection in such objects, in particular Saturn's tiny moon Enceladus. Enceladus harbours a global subsurface ocean hidden beneath an icy crust that is liquid likely due to strong tidal dissipation in the moon's core providing large amounts of thermal energy. Observations from the Cassini satellite show anomalously high temperatures at the Southern Pole, where we find four large troughs. This region is geologically active with observed cryo-volcanism where plumes of water vapour and icy particles are ejected from Enceladus' subsurface ocean and actively maintain Saturn's E-ring. The massive influx of energy generates temperature gradients inside the ocean that drive ocean currents via thermal convection. This likely controls the lateral thickness of the ice shell and consequently lateral ocean depth with variations of roughly 20 kilometers from the South Pole to the equator, with deeper depths located at the polar regions that are also linked with stronger heat fluxes at the ocean floor.

Former studies that simulated thermal convection in subsurface oceans neglected the influence of variable ocean depth and heterogeneous distribution of heat at the ocean floor, even though both properties likely have a strong presence in Enceladus' ocean. In this study, we analysed how a variable ocean thickness affects flow patterns and heat transfer behaviour in an Enceladan ocean using direct numerical simulations with a spectral element solver. We simulated two ocean geometries, a (traditional uniform ocean with constant thickness, and a non-uniform ocean with a spherical harmonic degree-2 zonal thickness profile that varies only with latitude. We explored a wide parameter space that incorporated flow regimes from onset of convection to weakly influenced by rotation, by varying the degree of thermal forcing, expressed by the Rayleigh number Ra. The parameter space ranged from $Ra = 1.6 \times 10^5$ to $Ra = 5.0 \times 10^6$ with a constant Ekman number of $Ek = 3 \times 10^{-4}$ and a Prandtl number with unity magnitude, $Pr = 1$.

The results demonstrate that for both geometries convection onsets at the equator for low Ra and gradually onsets also at higher latitudes with increasing Ra. Zonal flows are found in the complete parameter range studied and are characterised by speeds that are nearly invariant in the direction of rotation and is structured with prograde flowing jets at the equator and retrograde flowing jets at higher latitudes. Radial currents increase in speed with the increase of Ra as the influence of rotation gradually diminishes. In the non-uniform geometry, convection is found to onset for a lower Ra in the polar region compared to the uniform geometry, due to the increased thickness found at the poles. This difference in polar ocean depth is also accompanied by a less effective heat transfer for the non-uniform geometry when Ra is further increased for both geometries. Scaling for both models of global heat transfer and flow speed diagnostics are in good agreement with literature, even though heat transfer efficiency is reduced for the non-uniform model caused by this weaker polar convective circulation. Assuming that a long-term stability exists for the ice shell thickness profile on Enceladus (Čadek *et al.*, 2019), a consistently higher heat flux must be transported to the poles as opposed to the equator to refrain the ice shell from melting at the equator and freezing at the poles. In light of this, we find that the ratio of heat flux at the poles to the heat flux at the equator is much stronger for the uniform model as this ratio for the non-uniform model only marginally favours polar convection for high Ra. This result suggests that much stronger heat fluxes at the poles are required compared to the equator (i.e., higher ratio), for instance from strong ocean floor heat flux heterogeneity favouring polar heating (Choblet *et al.*, 2017*a*; Liao *et al.*, 2020).

This work presented a new direction where the influence of global topographical variations was analysed. Future work can extend this by exploring a broader parameter space with Ra and Ek, varying the shell geometry and deformation amplitudes, improving boundary conditions to include water-ice phase-transitions and heterogeneous ocean floor heating and by incorporating mechanical forces that perturb Enceladus' ocean as it orbits Saturn.

Contents

List of Figures ix

List of Tables xi

List of Symbols xiii

1 Introduction 1
- 1.1 Modelling fluid dynamics . . . 3
  - 1.1.1 Governing equations . . . 3
  - 1.1.2 The Boussinesq approximation . . . 4
  - 1.1.3 Non-dimensional governing parameters . . . 5
  - 1.1.4 Estimation of Enceladan parameter space . . . 6
- 1.2 Research objective . . . 7
- 1.3 Thesis outline . . . 9

2 Heat transfer behaviour of rotating Rayleigh-Bénard convection in a spherical shell with variable meridional thickness 11
- 2.1 Introduction . . . 11
- 2.2 Methods . . . 13
  - 2.2.1 Problem formulation . . . 13
  - 2.2.2 Numerical domain . . . 13
  - 2.2.3 Numerical method . . . 14
  - 2.2.4 Parameter space and numerical resolutions . . . 14
  - 2.2.5 Diagnostics . . . 16
- 2.3 Results . . . 18
  - 2.3.1 Flow field behaviour . . . 19
  - 2.3.2 Heat transfer scaling . . . 25
  - 2.3.3 Flow speed scaling . . . 27
  - 2.3.4 Interior heat transfer . . . 28
  - 2.3.5 Outer boundary heat flux . . . 31
- 2.4 Conclusions . . . 34

3 Conclusions and recommendations 37
- 3.1 Conclusions . . . 37
- 3.2 Recommendations . . . 38

A Supplementary materials 41
- A.1 Summary of results . . . 41
- A.2 Thermal and Ekman boundary layer scaling . . . 43
  - A.2.1 Boundary layer estimation technique . . . 43
  - A.2.2 Thermal boundary layers . . . 43
  - A.2.3 Viscous boundary layers . . . 45
- A.3 Supplementary non-rotating simulations . . . 48

B Numerical tools 51
- B.1 Numerical method . . . 51
  - B.1.1 Basic concepts of the spectral element method . . . 51
  - B.1.2 Nek5000: A spectral element solver . . . 52
  - B.1.3 Gaussian quadrature . . . 52
- B.2 Benchmarking canonical fluid flows . . . 53

B.2.1 Rayleigh-Bénard convection in 2D 53
B.2.2 Taylor-Green vortex in 2D: Convergence analysis 55
B.2.3 Taylor-Green vortex in 3D: Validation with rotation 57
B.3 Modelling rotating convection in a spherical shell 60
B.3.1 Meshing of fluid domain 61
B.3.2 Initial and boundary conditions 61
B.3.3 A test case of rotating spherical shell convection 62

Bibliography **67**

List of Figures

1.1 Saturn's icy satellite Enceladus . . . 2
1.2 Estimated ocean thickness of Enceladus in a hammer projection . . . 3
1.3 Enceladan parameter space and computational range . . . 8

2.1 Schematic of numerical domains for uniform and non-uniform spherical shells . . . 15
2.2 Parameter space of this work comprising variable degree of thermal forcing . . . 16
2.3 Temporal evolution and convergence of the Nusselt number . . . 18
2.4 Three-dimensional snapshots of temperature anomaly and axial vorticity . . . 22
2.5 Overview of zonally averaged meridional fields in uniform domain . . . 23
2.6 Overview of zonally averaged meridional fields in non-uniform domain . . . 24
2.7 Nusselt versus Rayleigh number behaviour . . . 26
2.8 Normalised Nusselt number versus Rayleigh number scaling . . . 26
2.9 Convective Reynolds number scaling . . . 28
2.10 Temperature profile and interior gradient in uniform shells . . . 29
2.11 Temperature profiles for polar and equatorial regions for uniform shells . . . 29
2.12 Temperature profiles for polar and equatorial regions for non-uniform shells . . . 30
2.13 Mid-depth temperature gradients in polar and equatorial regions for uniform and non-uniform shells . . . 30
2.14 Time and zonally averaged normalised heat flux profiles . . . 32
2.15 Heat flux comparison between uniform and non-uniform geometries . . . 33
2.16 Heat flux tangent cylinder contrast and heterogeneity . . . 33

A.1 Boundary layer estimation technique . . . 43
A.2 Thermal boundary layer thickness scaling in uniform shell . . . 44
A.3 Thermal boundary layer thickness scaling in non-uniform shell . . . 45
A.4 Ekman boundary layer thickness scaling in uniform shell . . . 47
A.5 Ekman boundary layer thickness scaling in non-uniform shell . . . 47
A.6 Nusselt versus Rayleigh number behaviour in a non-rotating uniform spherical shell . . . 49

B.1 Rayleigh-Bénard convection in 2D box model . . . 54
B.2 Nusselt number evolution in Rayleigh-Bénard convection problem . . . 55
B.3 Taylor-Green vortex problem in a two-dimensional domain . . . 56
B.4 Taylor-Green vortex convergence curves for time and space discretisations . . . 57
B.5 Taylor-Green vortex with rotation visualised with Q-criterion . . . 59
B.6 Comparison of kinetic energy and dissipation rate for rotating 3D Taylor-Green vortex problem . . . 60
B.7 Spectral element domain of a spherical shell . . . 61
B.8 Reynolds number evolution in spherical shell simulations . . . 64
B.9 Heat flux anomaly profiles in spherical shell simulations . . . 65
B.10 Meridional temperature fields and boundary heat flux fields in spherical shell simulations 65

List of Tables

1.1 Physical properties of Enceladus 7

2.1 Summary of results comprising most relevant diagnostics 19

A.1 Summary of results of diagnostics related to model resolution 42
A.2 Summary of results for non-rotating simulations 49

List of Symbols

$\boldsymbol{u}$	velocity vector
u, v, w	velocity components
$\boldsymbol{r}$	position vector
r	radius
x, y, z	Cartesian coordinates
P	pressure
T	temperature
$\boldsymbol{g}$	gravity vector
g	gravitational acceleration
κ	thermal diffusivity
k	thermal conductivity
c_p	specific heat capacity at constant pressure
ν	viscous diffusivity / kinematic viscosity
μ	dynamic viscosity
ρ	density
ρ_o	background density
$\boldsymbol{\Omega}$	rotation vector
Ω	rotation rate
t	time
τ_a	advection time
D	shell thickness / length scale
α_T	thermal expansion coefficient
Ek	Ekman number
Ra	Rayleigh number
Ra_c	critical Rayleigh number
Ra_Q	flux-based Rayleigh number
Ra^*	modified Rayleigh number
Ro_c	convective Rossby number
Pr	Prandtl number
Nu	Nusselt number
Re	Reynolds number
Re_c	convective Reynolds number
Re_h	horizontal Reynolds number
Ro	Rossby number
$\mathcal{E}_k$	kinetic energy density
$\boldsymbol{\omega}$	vorticity vector
ω	vorticity
β_T	temperature gradient at mid-depth
χ	radius ratio
ϑ	co-latitude
φ	longitude
P_l^m	associated Legendre polynomial of degree l and order m
C_{lm}	deformation coefficient of degree l and order m
η_k	Kolmogorov length scale
ϵ_U	viscous dissipation rate
q	heat flux
Q	heat flux or Q-criterion value
N_r	radial mesh element count
N_h	horizontal mesh element count

p	polynomial order
δ_T	thermal boundary layer thickness
δ_ν	viscous boundary layer thickness
δ_E	Ekman boundary layer thickness
Γ	problem domain
N	spectral element count
ζ	enstrophy

1

Introduction

The solar system harbours many icy celestial bodies that have or have had subsurface water reservoirs hidden below a frozen crust. The list of subsurface water worlds ranges from the moons of the gas giants Jupiter and Saturn, to the outer regions of the solar system with dwarf planet Pluto and its satellite Charon. We adopt the terminology of *icy moons* for moons or natural satellites that have a surface composition that is predominantly ice. For several icy moons it is predicted that their interiors comprise salty liquid water oceans, transporting heat from the inner core towards the upper icy crust via large scale ocean circulations. This exchange pathway of heat and mass among the rocky core, the ocean and the ice shell provides a compelling possibility for life to arise and flourish (Cockell *et al.*, 2016). The thermal modification of ice shells have also been linked to interior ocean behaviour from transported heat through the ice shell (Collins *et al.*, 2000; Goodman *et al.*, 2004).

The Cassini-Huygens mission actively analysed the gas giant Saturn from 2004 until 2017, and successfully strengthened the evidence for the existence of subsurface water reservoirs in the icy satellites of the planet. Convincing evidence is, in addition to Enceladus, found for Titan to likely contain a global subsurface ocean beneath a spatially variable, thick ice shell (e.g., Béghin *et al.*, 2012, 2010; Bills & Nimmo, 2008; Iess *et al.*, 2012). Cassini's various flybys of Enceladus brought a slew of data on the potential existence of a subsurface ocean. Of particular interest were the observations of the geologically young and active region at Enceladus' Southern Pole. Temperatures measured at the South Polar Terrain (SPT) were anomalously high, which Spencer *et al.* (2006) attributed to the combination of radiogenic and (recent) tidal heating. The SPT is characterised by four large troughs, informally referred to as *tiger stripes*, where active cryo-volcanism is observed to occur. Plumes of water vapour and icy dust particles ejected from this region are likely the main source of Saturn's E-ring (Porco *et al.*, 2006; Spencer *et al.*, 2006) (see Figure 1.1 (a)). From the shape, geologic activity, estimated heat flux and gravity field of Enceladus, a local liquid ocean was (at the very least) inferred at the South polar area (Collins & Goodman, 2007; Iess *et al.*, 2014). From subsequent flybys, major constituents in the plumes of Enceladus were identified comprising mostly water and carbon dioxide ices, but more important to the existence of a liquid ocean, the presence of ammonia and salts (Postberg *et al.*, 2009; Waite Jr *et al.*, 2009). The melting temperature of ice is substantially lowered by salts (Postberg *et al.*, 2009; Waite Jr *et al.*, 2009) and its presence in the ocean suggests that the rocky core is most likely in direct contact with the ocean layer (Postberg *et al.*, 2011; Waite Jr *et al.*, 2009; Zolotov, 2007). Enceladus is experiencing periodic (gravitational) torques due to its eccentric orbit and stretched shape causing physical librations. Thomas *et al.* (2016) showed that the magnitude of the physical libration is too large for a moon with a localised ocean where the ice shell would be predominantly in direct contact with the core. Hence, the most recent results indicate that Enceladus has a global ocean, decoupling the ice shell from the rocky interior (Thomas *et al.*, 2016) (see Figure 1.1 (b)).

The circulation in these global subsurface oceans therefore governs the exchange pathway of heat and mass (e.g., constituents from the rocky core) between the sea-floor and the overlying ice mantle. Oceanic currents can be driven by internal heat sources, mechanical or magnetic forces (e.g., Soderlund *et al.*, 2020). In this study, we focus solely on the transport of heat via thermal convection. Convection is the motion of fluid caused by differences in density of surrounding fluid elements, making light elements rise and heavy elements sink. In these subsurface oceans, differences in density may be caused by

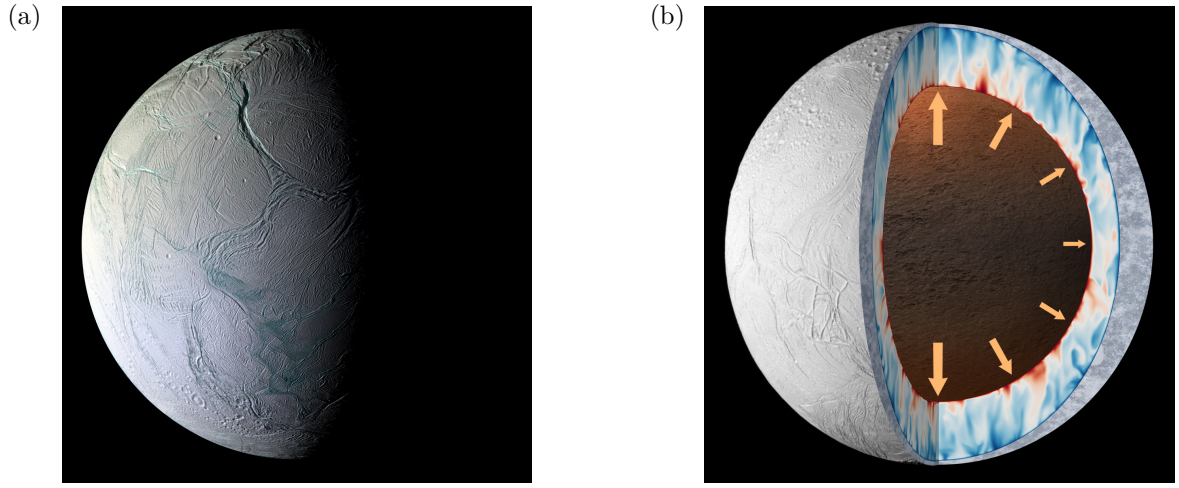

Figure 1.1: Saturn's icy satellite Enceladus. (a) A view of the Southern region of Enceladus captured by the Cassini Orbiter on October 9, 2008. Here, the pristine white surface is almost clear of impact craters and is filled with fractures and troughs, demonstrating the moon's geological activity. On the bottom half of the image and near the night side of the moon, the tiger stripes are partially visible which have been found origin to active cryo-volcanism and source to Saturn's E-ring. Image credit: NASA/JPL/Space Science Institute. (b) Impression (not to scale) of the interior structure of Enceladus demonstrating thermal convection in a non-uniform ocean situated between a rocky core and ice shell. The schematic looks directly at the equator with the North Pole up. Heterogeneous heat flux at the ocean floor is illustrated by the size of the arrows (with higher heat flux associated with larger arrows). (e.g., Choblet *et al.*, 2017*a*).

temperature variations or compositional changes of the fluid elements (e.g., salinity). Radioactive decay in the rocky core beneath the ocean can provide sufficient heat to the ocean floor and destabilise it to onset convection (Nimmo & Pappalardo, 2016). That is, warmer waters at the ocean floor expand, become lighter and rise. Furthermore, moons with eccentric orbits about their host planet can generate energy from tidal heating caused by friction inside the (porous) cores from tidal deformations (e.g., Choblet *et al.*, 2017*a*; Liao *et al.*, 2020; Soderlund *et al.*, 2020). Mechanically-driven flows are controlled by a moon's orbital characteristics, driving ocean circulation from ocean tides and from the non-uniform rotation of the moon with periodic precessional and libration-driven forces. Finally, ocean currents can be also driven by means of electromagnetic pumping as found for the Jupiter-Europa system (Gissinger & Petitdemange, 2019).

The subsurface ocean thickness and its lateral variation can be inferred from ice shell thickness models that are constrained by topographical data and gravity (e.g., Baland *et al.*, 2014; Beuthe *et al.*, 2016; Čadek *et al.*, 2019, 2016; Hemingway & Mittal, 2019; Kvorka *et al.*, 2018). This can provide further insight into the heat exchange pathways between the inner core, subsurface ocean and outer ice shell. Čadek *et al.* (2016) modelled the internal structure of Enceladus using libration, shape and gravity data to discern the core, ocean and ice shell depths, finding a mean ice shell thickness of 18-22 km with thicknesses as thin as 1.5-5 km at the South Pole. Consistent with their more recent study of Čadek *et al.* (2019) and the work of Beuthe *et al.* (2016), the authors find a strong low (spherical harmonic) degree ice shell thickness variability with a minimum amplitude at the South Pole and maximum amplitude near the equator. Based on their estimated global heat loss of 25-30 GW and the local heat loss of 3-5 GW at the South Pole, Čadek *et al.* (2016) argued that the produced heat from tidal deformation is insufficient to retain the ocean's current shape suggesting that the ocean is either crystallising at the equator or the core produces a significant amount of heat to counterbalance this. Choblet *et al.* (2017*a*) and Liao *et al.* (2020) demonstrated that for a porous rocky core, tidal dissipation in the core can generate sufficient heat to sustain a global ocean. The increased heat production in polar regions further supports the localised ice shell thinning observed at the South Pole of Enceladus, however the longitudinal variability in shell thickness might be better explained by tidal dissipation in the ice shell itself (Hemingway & Mittal, 2019). Similar to the study of Čadek *et al.* (2016), Čadek *et al.* (2019) modelled the interior structure of Enceladus using a different shape model and inferred from the ice shell thickness the heat flux variations at the bottom of the ice shell. This derived heat flux distribution demonstrates higher heat flux in the polar regions and lower heat flux near the equator, in agreement with the results of Hemingway & Mittal (2019) who performed a similar study with a different isostacy

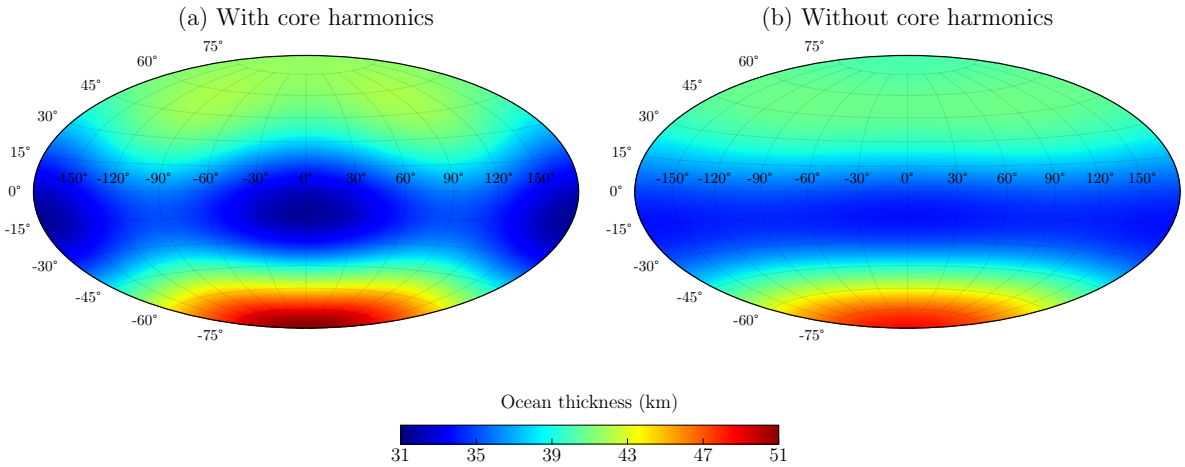

Figure 1.2: Thickness profiles of Enceladus' ocean visualised in a hammer projection using the results of Čadek *et al.* (2019) for spherical harmonic expansion coefficients C_{20}, C_{22}, C_{30}, with mean radii of 194 and 232.1 km for the core-ocean and ocean-ice interfaces respectively. (a) The ocean thickness profile obtained from spherical harmonic expansion coefficients up to degree 3 for both the core-ocean and ocean-ice boundaries. Thickness of the ocean ranges between 31.4 and 50.8 km. (b) The ocean thickness profile obtained from spherical harmonic expansion coefficients up to degree 3 for only ocean-ice boundary while assuming a homogeneous, constant radius spherical core of 194 km. This reduces the thickness range to 33.8 and 49.0 km.

model. Figure 1.2 shows the ocean thickness profile for low degree spherical harmonics derived from the results of Čadek *et al.* (2019). The precise shape of the core is poorly constrained and has been treated separately in (b) to visualise its influence on ocean thickness by considering a constant radius for the core. In both scenarios, Enceladus' ocean model comprises large meridional variations with an estimated maximum thickness of 50.8 km at the South Pole and minimum thickness of 31.4 km at the equator

In this work we focus on Saturn's moon Enceladus as it possesses characteristics that are unique to this satellite: a subsurface ocean that extents globally under the icy crust and varies significantly in thickness laterally. Potentially due to tidal dissipation in the porous unconsolidated rocky core, large spatial heterogeneities in ocean floor heat flux give rise local variations in ice shell topography modifications and hence ocean thickness variations. The influence of the ocean's shape on the oceanic circulation patterns and transport of heat from the inner core to the ice shell remains uncertain and is the main focus of this work.

1.1. Modelling fluid dynamics

In this study, we simulate three-dimensional fluid flows using direct numerical simulations. In particular, we focus on Rayleigh-Bénard convection that is governed by differences in density of the fluid, where lighter fluid elements rise and heavier fluid elements sink due to the force of gravity. Rotating and non-rotating Rayleigh-Bénard convection provide analogues to natural systems found in celestial bodies and allow us to investigate the fluid flow characteristics found in these systems. On Earth, for instance, we find convective systems in the oceans and atmosphere and in the planet's liquid outer core, convective motions governed by thermal and compositional density gradients drive currents that help generate the magnetic field (Elsasser, 1939). Here, we briefly introduce the governing equations of fluid dynamics that describe these characteristic fluid motions (Section 1.1.1). As presented in Appendix B.2, simulations have been performed that employed different assumptions on the fluids behaviour, e.g., isothermal and non-rotating fluids, resulting in a slightly different set of equations. Below, the equations of motion for a fluid in a rotating frame of reference are given. This is followed by the Boussinesq approximation often applied in convection problems (Section 1.1.2) and the non-dimensionalisation of these equations (Section 1.1.3).

1.1.1. Governing equations

Three conservation principles define the equations of motion for fluids, namely the conservation of mass, momentum and energy. By invoking the continuum hypothesis, we assume that the fluid is fully

continuous and homogeneous which holds for lengths scales that are significantly larger than the distance between individual molecules in the fluid (Batchelor & Batchelor, 2000). When the fluid system neither has sources nor sinks and the fluid is assumed to be incompressible, the conservation of mass is given by the incompressible continuity equation

$$\nabla \cdot \boldsymbol{u} = 0, \tag{1.1}$$

where $\boldsymbol{u}$ is the fluid velocity. The momentum equation is obtained by applying Newton's second law of motion on the continuous incompressible fluid. We further assume that the fluid is Newtonian, such that viscous stresses act proportionally to the strain rate on the fluid element, and that the fluid's viscosity is constant. Finally, the momentum equation holds for an inertial frame of reference, stating that a body with zero net forces acting on it should not accelerate. Therefore, by changing the non-rotating frame of reference to a rotating, non-inertial frame, fictitious forces are introduced to the problem, namely the Coriolis and centrifugal forces. The incompressible Navier-Stokes momentum equation in a rotating reference frame is then given by

$$\rho\left(\frac{\partial \boldsymbol{u}}{\partial t} + \boldsymbol{u}\cdot\nabla\boldsymbol{u} + 2\boldsymbol{\Omega}\times\boldsymbol{u} + \boldsymbol{\Omega}\times(\boldsymbol{\Omega}\times\boldsymbol{r})\right) = -\nabla P + \rho\boldsymbol{g} + \mu\nabla^2\boldsymbol{u}, \tag{1.2}$$

where ρ is the fluid density, t is the time, $\boldsymbol{\Omega}$ is the angular velocity vector of the frame of reference, $\boldsymbol{r}$ is the position vector, P is the pressure, $\boldsymbol{g}$ the gravitational acceleration and μ is the dynamic viscosity. The terms $2\boldsymbol{\Omega}\times\boldsymbol{u}$, $\boldsymbol{\Omega}\times(\boldsymbol{\Omega}\times\boldsymbol{r})$ and $\rho\boldsymbol{g}$ are the Coriolis, centrifugal and buoyancy forces, respectively. The centrifugal force can be expressed as a gradient of a potential

$$\boldsymbol{\Omega}\times(\boldsymbol{\Omega}\times\boldsymbol{r}) = -\nabla\left[\frac{1}{2}(\boldsymbol{\Omega}\times\boldsymbol{r})^2\right], \tag{1.3}$$

and is therefore generally combined with the pressure gradient to form the reduced pressure (Davidson, 2013). If, however, the problem is described in a non-rotating, inertial frame of reference, the fictitious centrifugal and Coriolis forces vanish in Equation 1.2 above. The final principle of conservation of energy states that the total rate of change of energy in a fluid equals the rate of energy acquired from heat and work. We further assume that no heat sources or viscous dissipation from element deformation add energy into the system. This yields the energy or heat equation

$$\rho c_p\left(\frac{\partial T}{\partial t} + \boldsymbol{u}\cdot\nabla T\right) = \nabla\cdot(k\nabla T), \tag{1.4}$$

with c_p the specific heat capacity at constant pressure, T the temperature, $k = c_p\rho\kappa$ the thermal conductivity and κ the thermal diffusivity. The system of equations is now complete, where the variable solutions for velocity $\boldsymbol{u}$, pressure P and temperature T can be found using numerical methods. For isothermal fluids, only the continuity and Navier-Stokes equations are necessary to solve for the four unknowns comprising the pressure term and the three velocity components.

1.1.2. The Boussinesq approximation

The Boussinesq approximation is often used in Rayleigh-Bénard convection studies to simplify the set of Equations 1.1 - 1.4. In this approximation, the density parameter is assumed constant except for the buoyancy term in the Navier-Stokes momentum equation. We assume that density variations are only caused by the expansion and contraction of a fluid due to temperature variations[1]. This means that the density is only considered variable in the buoyancy term in Equation 1.2. In particular, the vertical extent of the fluid domain is assumed to be significantly smaller than the scale height of pressure and density (Spiegel & Veronis, 1960). The assumption that density decreases minimally over the domain is generally acceptable for convection in oceans, planetary interior mantles and liquid cores. However, the approximation loses validity in systems where the scale height is substantially smaller, such as in the atmospheres of gas giants or in stellar convection zones (Glatzmaier, 2013). These convection problems are then better described by the anelastic approximation. As the incompressible set of equations in Section 1.1.1 already assumes a constant density, the continuity and heat equations remain unchanged in the Boussinesq approximation. The momentum equation is simplified by assuming small density

[1] This assumption is standard for thermal convection and can be supplemented by compositional variations like salinity in sea-water

variations through thermal expansion of a fluid element. That is, a temperature difference causes expansion or contraction of a fluid element, such that the density decreases or increases accordingly. This is given by the equation of state (Pedlosky, 2013)

$$\rho = \rho_o(1 - \alpha_T(T - T_o)), \tag{1.5}$$

where ρ is the density, ρ_o the fluid background density, α_T the thermal expansion coefficient, T the temperature and T_o the background temperature. We substitute the equation of state (Equation 1.5) in the buoyancy term of the momentum equation (Equation 1.2) and replace the variable density ρ by the constant background density ρ_o for all other terms in Equation 1.2. We also subtract the hydrostatic background state from the momentum equation (Equation 1.2) where the fluid is motionless, $\boldsymbol{u} = 0$, and gravity acts in the vertical direction, $\boldsymbol{g} = g_o\hat{\boldsymbol{e}}_z$, given by

$$\frac{dP}{dx} = 0, \quad \frac{dP}{dy} = 0, \quad -\frac{1}{\rho_o}\frac{dP}{dz} - g_o\rho_o = 0, \tag{1.6}$$

with g_o the reference gravitational acceleration and $\hat{\boldsymbol{e}}_z$ the vertical unit vector. This results in the Boussinesq equations that together describe the thermal Rayleigh-Bénard convection problem

$$\frac{\partial \boldsymbol{u}}{\partial t} + \boldsymbol{u}\cdot\nabla\boldsymbol{u} + 2\boldsymbol{\Omega}\times\boldsymbol{u} = -\frac{1}{\rho_o}\nabla\Pi + \nu\nabla^2\boldsymbol{u} - \alpha_T g_o T\hat{\boldsymbol{e}}_z, \tag{1.7}$$

$$\nabla\cdot\boldsymbol{u} = 0, \tag{1.8}$$

$$\frac{\partial T}{\partial t} + \boldsymbol{u}\cdot\nabla T = \kappa\nabla^2 T, \tag{1.9}$$

where Π is the reduced pressure term with the centrifugal term incorporated and $\nu = \mu/\rho_o$ is the kinematic viscosity.

1.1.3. Non-dimensional governing parameters

Non-dimensionalising the governing fluid equations generalises the fluid problem by a set of (non-dimensional) parameters defined as ratios of various quantities. That is, the equations are no longer described in physical dimensions (e.g., meter for length or meter per second for velocity) as they are divided by predetermined scales with the same units. Non-dimensional numbers follow from this operation and give insight into the problem by showing which terms dominate the fluid behaviour. Typical scales used are D for length (e.g., box height or shell thickness) and temperature difference ΔT for temperature scale. The time variable in geophysical problems is generally scaled by the viscous diffusion time D^2/ν, when the expected fluid flow timescale is similar to viscous diffusion (Zhang & Liao, 2017). Alternatively, if the expected fluid flow time scale is similar to the rotation period Ω^{-1}, then this timescale is considered more appropriate. Moreover, time can also be scaled by D/U, where U is a typical velocity scale. Note that a combination of length and time scales are sufficient to define the velocity scale (i.e., velocity is defined by length and time). A sample set of non-dimensional scales are,

$$t = \Omega^{-1}\,\hat{t}, \quad x = D\,\hat{x}, \quad \boldsymbol{u} = \Omega D\,\hat{\boldsymbol{u}}, \quad T = \Delta T\,\hat{T}, \tag{1.10}$$

where the caret symbol indicates non-dimensional variables solved in the computations. In essence, the non-dimensionalisations in Equation 1.10 are substituted in the governing equations that lead to ratio terms describing key characteristics of the fluid. For instance, the Reynolds number, $Re = UD/\nu$, describes the ratio of inertial to viscous effects, where large Reynolds numbers are associated with turbulent fluids. The Rossby number, $Ro = U/\Omega D$, describes the ratio of inertial to Coriolis forces, with low Rossby numbers associated with strong Coriolis effects. Similarly, the Ekman number, $Ek = \nu/\Omega D^2$, describes the ratio of viscous to Coriolis forces. The Ekman number is inversely related to the Reynolds number, such that fluids with a small Ekman number have strong rotational effects and are generally more turbulent (i.e., high Re). The Rayleigh number, $Ra = \alpha_T g_o \Delta T D^3/\nu\kappa$, describes ratio of the buoyancy force to viscous and thermal diffusivity effects. Here, a high Rayleigh number is associated with a strong thermally buoyant fluid. The tendency for a fluid to start overturning circulation, however, is defined by a minimum Rayleigh number where the fluid becomes unstable to convection: the critical Rayleigh number Ra_c. Finally, the Prandtl number, $Pr = \nu/\kappa$, describes the ratio of viscous and thermal diffusive effects.

High Prandtl number fluids are very viscous (e.g., in Earth's mantle $Pr \approx \mathcal{O}(10^{23})$ (Yoshida, 2017)) such that diffusivity is dominated by the momentum of the fluid, as opposed to low viscosity fluids (e.g, in stellar interiors $Pr \approx \mathcal{O}(10^{-3})$ (Miesch, 2005)), where thermal diffusivity dominates. The convective Rossby number, $Ro_c = Ra^{1/2} Ek Pr^{-1/2}$, is a common proxy in rotating Rayleigh-Bénard convection that is independent of thermal and viscous diffusivities (i.e., κ and ν) and describes the relative force balance of buoyancy to Coriolis (e.g., Gilman, 1977). Hence, systems with $Ro_c \ll 1$ are rotationally dominated and systems with $Ro_c > 1$ approach behaviour that are reminiscent of non-rotating convection. An important non-dimensional output parameter often recorded is the Nusselt number, $Nu = qD/\kappa\rho c_p \Delta T$, where q is the integrated heat flux. The Nusselt number describes the ratio of total heat flux to heat flux from just conduction, meaning that a non-convective fluid always has the minimum Nusselt number of 1.

We can substitute the non-dimensionalisation of the variables given in Equation 1.10 into the equations of motion in Equations 1.7-1.9. The coefficients that appear on the left-hand side of the equal sign in Equations 1.7 and 1.9 are brought over to the right-hand side to yield the non-dimensional Boussinesq equations (see Section 2.2.1)

$$\nabla \cdot \boldsymbol{u} = 0, \tag{1.11}$$

$$\frac{\partial \boldsymbol{u}}{\partial t} + \boldsymbol{u} \cdot \nabla \boldsymbol{u} + 2\,\hat{\boldsymbol{e}}_z \times \boldsymbol{u} = -\nabla P + Ek \nabla^2 \boldsymbol{u} + Ro_c^2 \frac{\boldsymbol{r}}{r_o} T, \tag{1.12}$$

$$\frac{\partial T}{\partial t} + \boldsymbol{u} \cdot \nabla T = \frac{Ek}{Pr} \nabla^2 T, \tag{1.13}$$

where $\hat{\boldsymbol{e}}_z$ is the unit vector in the direction of the rotation axis and ∇P is the non-dimensional reduced pressure term.

1.1.4. Estimation of Enceladan parameter space

Table 1.1 summarises the physical characteristics of Enceladus. Here, we roughly estimate the non-dimensional Ekman, Rayleigh and Prandtl numbers from literature. Following Melosh *et al.* (2004) and Soderlund *et al.* (2014), we estimate the temperature drop across the ocean ΔT to find the Rayleigh number. This is estimated by relating Nusselt-Rayleigh scaling behaviours where an estimated ocean ceiling heat flux is used to relate the two numbers. To find the range of possible temperature differences, two extreme heat transfer efficiencies are considered for rapidly rotating rotating and non-rotating convection. Rapidly rotating convection is predicted to follow the scaling $Nu = 0.15 Ra^{3/2} Ek^2$ (Gastine *et al.*, 2016), yielding the temperature drop expression by setting this scaling equal to $Nu = qD/\kappa\rho c_p \Delta T$ and after some algebraic manipulations,

$$\Delta T = 2.1 \left(\frac{\Omega^4 \kappa}{\rho^2 c_p^2 \nu \alpha_T^3 g^3} \right)^{1/5} (q^2 D)^{1/5}, \tag{1.14}$$

and non-rotating convection is predicted to follow $Nu = 0.07 Ra^{1/3}$ (Gastine *et al.*, 2015), yielding the temperature drop expression

$$\Delta T = 7.3 \left(\frac{\nu}{\alpha_T g_o \kappa^2 \rho^3 c_p^3} \right)^{1/4} q^{3/4}. \tag{1.15}$$

We find the mean ocean ceiling heat flux q using the estimated global heat loss of $20 - 35$ GW via thermal diffusion through the ice shell of Enceladus (Čadek *et al.*, 2019; Hemingway & Mittal, 2019). Here we use the mean radius at the ocean top of 232.1 km from Čadek *et al.* (2019) to average the heat flux over the spherical surface, yielding a mean heat flux of $q = 29.5 - 51.7$ mWm^{-2}. By exploring the parameter space, we find the range of adiabatic temperate gradients, with 0.93 mK $\leq \Delta T \leq 10.1$ mK.

Simulating a geophysical object with their (estimated) parameter space is currently not feasible due to computational constraints (e.g., Glatzmaier, 2002). As a result, the parameter space, commonly identified by the non-dimensional numbers (i.e., with Ra, Pr and Ek), is only accessible through extrapolations from less computationally demanding parameter ranges as displayed in Figure 1.3. Most geophysical models are roughly limited to parameter ranges of $Ek \geq 10^{-6}$ and $Ra \leq 10^7$ (Cheng *et al.*, 2018), yet more extreme magnitudes can be reached using 2,4 or 8-fold symmetries in pseudo-spectral codes (e.g., Gastine *et al.*, 2016) or simplifications of the model using for instance the quasi-geostrophic approximation (e.g.,

Ocean domain properties	Symbol and units	Enceladus
Gravitational acceleration	g_o (m/s^2)	0.13
Rotation rate	Ω (rad/s)	$5.3 \cdot 10^{-5}$
Kinematic viscosity	ν (m^2/s)	$1.8 \cdot 10^{-6}$
Thermal diffusivity	κ (m^2/s)	$1.4 \cdot 10^{-7}$
Ocean density	ρ (kg/m^3)	1000-1010
Thermal expansion coefficient	α_T (10^{-4} K^{-1})	3
Ocean thickness	D (km)	31.4 – 50.8
Ocean shell radius ratio	$\chi = r_i/r_o$	0.79 – 0.86
Heat flux	q (mW/m^2)	29.5 – 51.7
Ekman number	$Ek = \nu/\Omega D^2$	$1.3 \cdot 10^{-11} - 3.4 \cdot 10^{-11}$
Rayleigh number	$Ra = \alpha_T g \Delta T D^3/\nu\kappa$	$4.5 \cdot 10^{18} - 2.2 \cdot 10^{20}$
Prandtl number	$Pr = \nu/\kappa$	13

Table 1.1: Physical properties of Enceladus. Ocean ceiling gravity g_o is found using $g_o = GM/r_o^2$, where G is the gravitational constant and M is the moon's mass, with GM from Rappaport *et al.* (2007). r_o is the radius of the ocean ceiling of 232.1 km (Čadek *et al.*, 2019). The rotation rate Ω is obtained from Murray & Dermott (1999). Thermal and kinematic diffusivities are from Soderlund (2019) and we use the positive thermal expansion coefficient of saline water (e.g., Choblet *et al.*, 2017*a*). The ocean thickness range and radius ratios are derived from Čadek *et al.* (2019) with $r_i = 194$ km and r_o from derivation shown in Figure 1.2. Full heat flux estimation process and used references are given in this Section.

Guervilly *et al.*, 2019). This quasi-geostrophic model assumes a first order force balance between the Coriolis force and the pressure gradient, that holds in the limit $Ek \to 0$, and very small Rossby numbers $Ro \ll 1$. Using these methods, Gastine *et al.* (2016) reached with symmetry truncations Rayleigh and Ekman numbers of $Ra = 2 \times 10^{10}$ and $Ek = 3 \times 10^{-7}$ respectively, whilst Guervilly *et al.* (2019) reached with the quasi-geostrophic approximation Rayleigh and Ekman numbers of $Ra = 2 \times 10^{10}$ and $Ek = 3 \times 10^{-7}$ respectively. Figure 1.3 shows a rough indication of the geophysical parameter space of Enceladus and the limited subspace that is currently accessible with direct numerical simulations. Furthermore, the fluid flow regimes identified by Gastine *et al.* (2016) are presented to demonstrate the scaling laws that demarcate different fluid behaviours and ultimately help predict the behaviour in geophysical objects. We find that the estimated parameter space of Enceladus is clearly unreachable with current methods and requires extrapolation of the predicted regime to the accessible range. Symbols are added to Figure 1.3 to indicate the parameter range of similar studies that simulated subsurface oceans in icy moons (i.e., Amit *et al.*, 2020; Soderlund, 2019) and additionally the parameter range simulated in this study is shown. Our study hence incorporates the weakly non-linear and transitional regimes.

1.2. Research objective

We have shown that the estimated non-dimensional Rayleigh and Ekman numbers for Enceladus are on the order of 10^{20} and 10^{-11} respectively. Due to computational limitations, it is currently not possible to simulate geophysical fluid flows with these magnitudes. With decreasing Ekman numbers, the simulated fluid viscosity and hence fluid length scales decreases, thereby requiring much higher, unattainable spatial resolutions to resolve these flows. Parameter scaling laws are introduced to extrapolate the non-dimensional numbers from computationally acceptable to geophysical magnitudes. The scaling behaviour of the non-dimensional parameters is obtained using simplifications of the real-world domains, either by direct numerical simulations that solve the governing equations or by laboratory experiments (Cheng *et al.*, 2018). Scaling laws for rotating Rayleigh-Bénard convection are traditionally reduced to plane-layer geometries where the gravity vector is parallel to the axis of rotation or more recently by rotating spherical shell models (e.g., representing an ocean layer) where gravity acts radially (Gastine *et al.*, 2016). The former plane-layer studies then appropriately describe the behaviour of convection only near the polar regions, where gravity is roughly aligned with the rotation axis, whereas the latter studies appropriately model convection throughout the spherical domain in planetary systems. Applications of scaling laws have provided insight into the ocean circulation of Europa finding that heat flow is promoted at the equatorial region, which is consistent with the thermally modified Chaos terrain on the icy surface of the moon (Soderlund *et al.*, 2014). Soderlund (2019) furthermore simulated a range of Ekman and Rayleigh numbers to find similar correlations with other icy moons in our solar system. Amit *et al.* (2020) applied the scaling relations from Gastine *et al.* (2016) to infer the fluid regime and heat transfer

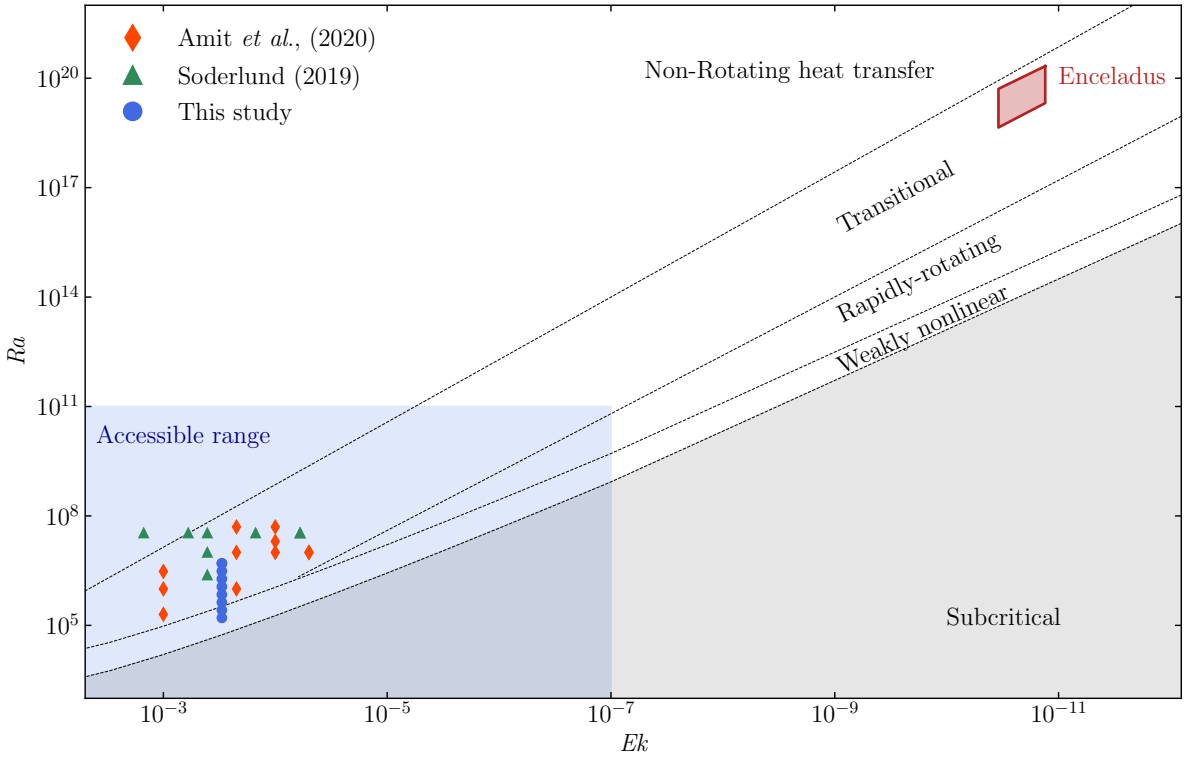

Figure 1.3: Geophysical parameter space with physical fluid regimes from Gastine *et al.* (2016). The estimated parameter space of Enceladus from Table 1.1 is denoted in the red box in the top right corner, and the computationally accessible range is shown in the violet box in the bottom left corner. For reference, the parameter selections of icy moon simulation studies are shown with orange diamonds denoting Amit *et al.* (2020) and green triangles denoting Soderlund (2019). Blue circles indicate the parameter selection for this study. Note that for visual reasons the markers *only* for cases with $Ek = 3 \times 10^{-4}$ are shifted to the left for Soderlund (2019) and shifted to the right for Amit *et al.* (2020) and do have the same value for all studies, i.e., $Ek = 3 \times 10^{-4}$. Precise definitions of the scaling laws and fluid regimes denoted in this schematic can be found in the work of Gastine *et al.* (2016).

behaviour of a subsurface ocean on Titan. In the cases of Titan and Enceladus, large heterogeneities that are expected in ocean floor heating (e.g., Choblet *et al.*, 2017*a*; Kvorka *et al.*, 2018) are neglected by using isothermal boundaries for the icy moon simulation studies (i.e., Amit *et al.*, 2020; Soderlund, 2019; Soderlund *et al.*, 2014). Particularly Enceladus contains possible large spatial variations in ocean thickness as well that could alter the ocean circulation patterns and heat transfer at the ice shell.

The prior studies assume perfect spherical ocean layers to infer oceanic fluid behaviour and heat transfer to the overlying ice shell. The predictions made on internal ocean circulation patterns and heat transfer behaviour in current studies (Amit *et al.*, 2020; Soderlund, 2019; Soderlund *et al.*, 2014) are hence based on the assumption of isothermal boundaries and constant ocean thicknesses. In this study we challenge this traditional approach of simulating perfect spherical shell domains that employ a constant ocean thickness, by manipulating the shell shape into one that conforms to the non-uniform subsurface ocean as predicted for Enceladus (Čadek *et al.*, 2019). In particular, we model an ocean that varies meridionally in thickness to approximate the large scale effects on ocean circulation and heat transfer behaviour for an Enceladan ocean. Secondary to the ocean's response to a varying thickness with latitude, we analyse the applicability of the scaling laws applied in prior studies to predict these characteristics. The more popular geophysical pseudo-spectral codes, which expand the numerical grid into constant radial level spheres, cannot be used to solve the equations on a non-uniform grid. A spectral element method code allows for the partitioning of the domain into many smaller elements such that more complex domains can be modelled. We have selected Nek5000 as the spectral element solver based on its ability to efficiently solve the governing equations and to handle additional related problems that were discovered early in the study. This included heterogeneous thermal boundaries (e.g., for simulating spatial variability of core-ocean heat transfer), double-diffusive convection in a stratified salty ocean and a complete model that combines mechanical forcings (e.g., tidal, precessional or librational)

with thermal convection (e.g., Vormann & Hansen, 2020). Hence, the development of this model can provide a new tool to perform future geophysical fluid dynamical research. More information on the spectral element code can be found in Appendix B.

The research questions for this study are therefore given by

1. *How are interior fluid flow structures and convective heat transfer behaviour affected by a non-uniform spherical shell domain in comparison to a uniform spherical shell domain?*

2. *To what extent can theoretical scaling laws of rotating Rayleigh-Bénard convection in uniform spherical shells predict internal flow structures and heat transfer behaviour for an Enceladan ocean?*

3. *How can rotating thermal convection in subsurface oceans with a variable thickness profile and/or heterogeneous boundary heat flux conditions be modelled?*

1.3. Thesis outline

In this work, we study the influence of a non-uniform ocean thickness on ocean circulation patterns and distribution of interior heat at the ice-shell bottom. The structure of this thesis is as follows. In Chapter 2, we provide the main results of this work in the form of a scientific paper. In this paper, we briefly introduce Rayleigh-Bénard convection with special attention to spherically uniform and non-uniform shell containers. Further, we formulate the problem and describe our methodology. The most important results from the study follow in Section 2.3 and we conclude the paper in Section 2.4. Supplementary information to this paper is given in Appendix A. To conclude the thesis in full, we discuss and answer the research questions posed in the introduction and provide recommendations for future research in Chapter 3. The third research question is primarily covered in Appendix B, where we describe the approach of this work to model thermal convection in uniform and non-uniform spherical shell containers. The reader interested in the underlying numerical methodology, preparatory benchmark simulations and model set-up is encouraged to read this appendix. The inexperienced reader may appreciate the step-by-step approach taken to develop and benchmark the model. We advise reading Chapter 1 first, followed by Appendix B, then Chapter 2 with Appendix A and finally the conclusions and recommendations of this work in Chapter 3.

2

Heat transfer behaviour of rotating Rayleigh-Bénard convection in a spherical shell with variable meridional thickness

Abstract

Saturn's moon Enceladus harbours a global subsurface ocean beneath its icy crust. Tidal dissipation within the moon's core generates a substantial amount of heat which leads to ocean convection. Observations of the moon indicate ocean thickness variations of up to ~ 20 km from equator to pole and heterogeneous heat generation within the core likely results in latitude-dependent temperature gradients. The effects of meridional thickness variations and heterogeneous temperature gradients on rotating thermal convection have not been simulated in previous studies. Here we simulate a non-uniform spherical shell employing a degree-2 zonal thickness profile. Using direct numerical simulations, we analysed various properties associated with heat transfer behaviour for flows in a uniform and non-uniform spherical shell domain driven by thermal convection with the Rayleigh number in the range $1.6 \times 10^5 \leq Ra \leq 5.0 \times 10^6$ and constant Ekman number of $Ek = 3 \times 10^{-4}$ and Prandtl number of $Pr = 1$. Our results demonstrate that different regimes of convection exist, which depend on the relative influence of rotation. With increasing thermal forcing, convection moves from being restricted to equatorial regions to filling the whole fluid domain. Global scaling behaviour for both domains was found to be consistent with literature, although weaker polar convection in non-uniform shells caused a decrease in heat transfer efficiency and thus a diminished heat transfer scaling behaviour. The diminishing transport of heat at the poles in the non-uniform shell deviates from the predicted heat flux profile at Enceladus (Choblet *et al.*, 2017*a*; Liao *et al.*, 2020), suggesting that stronger thermal heterogeneities are required to enhance polar heat transfer.

Key words: Bénard convection, rotating flows, geophysical and geological flows

---

2.1. Introduction

The study of convection finds many applications in natural systems of celestial bodies, as demonstrated by the large diversity in fluid systems on Earth alone, from its interior fluid layers to the oceans and atmosphere. Flows driven by convection can, among many other things, explain the intricate zonal bands in the upper regions of gas giants (Aurnou *et al.*, 2008; Glatzmaier *et al.*, 2009), magnetic field generation in planetary cores (Elsasser, 1939; Stevenson, 2003) and subsurface ocean circulation and ice shell modifications in icy satellites (e.g., Amit *et al.*, 2020; Soderlund *et al.*, 2014). The latter even attracts additional attention from an astrobiological perspective given the potential of liquid oceans, circulating heat and mass, to harbour a home to life (Cockell *et al.*, 2016). Studying these systems remains inherently constrained, as in-situ measurements are limited and laboratory experiments and

numerical simulations are currently unable to attain the astrophysical flow regime magnitudes. Empirical scaling laws are therefore sought that enable direct extrapolations to astrophysical parameter values using contemporary technology and methods.

The canonical problem of thermal convection is described by Rayleigh-Bénard convection that provides a simplified approach to understand complex large scale astrophysical flow patterns. This problem is traditionally described by an infinitely wide fluid layer situated between a heated bottom plate and cooled top plate (i.e., a plane layer geometry). Gravity is acting in the vertical direction, and a sufficiently high adverse temperature gradient, ΔT, destabilises the system to onset overturning circulation. With the addition of rotation, the onset of convection is delayed by the stabilising influence of the Coriolis force and the system initially assumes quasi-geostrophic motions that are nearly invariant in the axis of rotation in the form of axial columns (e.g., Cheng *et al.*, 2015). When the strength of convection dominates such that the influence of rotation becomes secondary, a non-rotating regime is approached that establishes an effective upper limit on heat transport for rotating convection.

The system without rotation is completely determined by the Rayleigh number, $Ra = \alpha_T g \Delta T D^3 / \nu\kappa$, and Prandtl number $Pr = \nu/\kappa$, where α_T is the thermal expansion coefficient, g the gravitational acceleration, ΔT the temperature drop across the vertical distance D between the two plates, and ν and κ the viscous and thermal diffusivities respectively. The rotating system additionally introduces the Ekman number, $Ek = \nu/\Omega D^2$, which describes the relative influence of viscous to Coriolis forces. Heat transfer efficiency is furthermore commonly expressed by the Nusselt number, $Nu = QD/\kappa\Delta T$, where Q is the total heat flux. The Nusselt number describes the relative heat transfer efficiency with respect to a static conductive state and provides a proxy for the heat transfer scaling of Rayleigh-Bénard convection.

Plane layer geometries replicate conditions of high-latitudes in planetary bodies where gravity acts parallel to the axis of rotation. However, due to the curvature of the spherical shell domains, the radial dependence of the gravitational acceleration and general misalignment of the rotation axis with the gravity vector for most of the domain, the scaling laws separately acquired for the plane layer and spherical shell geometries may not be directly transferable across the two domains (e.g., Cheng *et al.*, 2015; Gastine *et al.*, 2016, 2015). Furthermore, depending on the radius ratio of the shell, $\chi = r_i/r_o$, where r_i and r_o are the inner and outer radii respectively, and the gravity profile of the model, the asymmetry in spherical boundary surfaces causes asymmetry in the boundary layer thicknesses and temperature gradients at the boundaries (Gastine *et al.*, 2015).

Simulations of planetary interiors traditionally approximate fluid behaviour in uniform spheres or spherical shells with isothermal boundaries. However, many celestial objects are likely to contain spatial and thermal heterogeneities in their fluid interiors caused by strong mechanical forcings, e.g., from tides, precession or libration (Cébron *et al.*, 2010*a*), and internal processes, e.g., from radiogenic heat production or tidal dissipation (e.g., Choblet *et al.*, 2017*a*), that may alter the predicted fluid flow and heat transfer regimes. Lateral variations in boundary heat flux can substantially enhance the heat transfer efficiency and alter flow patterns compared to models with isothermal boundaries (Dietrich *et al.*, 2016; Mound & Davies, 2017). The influence of geometry on interior fluid behaviour in planetary bodies have been primarily studied in the context of body deformations in ellipsoidal containers. This is caused by strong tidal interactions and planetary rotation that may give rise to mechanical forcings driving fluid flows (Grannan *et al.*, 2017; Lemasquerier *et al.*, 2017; Noir & Cébron, 2013; Vormann & Hansen, 2020). In these natural systems, interior fluid motions are generated by tidal, librational and precessional mechanical disturbances (Cébron *et al.*, 2010*a*; Van Hoolst *et al.*, 2013), and can result in fluid instabilities that give rise to domain filling turbulence (Cébron *et al.*, 2010*a*). The impact of varying domain geometries on rotating thermal convection remains however largely unexplored (Vormann & Hansen, 2020), despite the significant impact of both shape and thermal forcing that are predicted in planetary interiors (Noir & Cébron, 2013; Vormann & Hansen, 2020). Elliptical deformations in a spherical two-dimensional equatorial plane have been demonstrated to affect convective flow patterns by shifting from zonal jets to more dipolar flow structures (Evonuk, 2015). Vormann & Hansen (2020) studied the influence of thermal forcing on precessional flow in spherical and spheroidal shells where they reproduced known scaling behaviour of thermal convection when the precessional force is subdominant and flow structures are reminiscent of rotating convection.

Contrary to the previous paragraph where body deformation assume a flattened polar axis, Saturn's natural satellite Enceladus is predicted to contain a subsurface ocean with a thermally deformed outer ice shell, yielding a shallow ocean depth near the equator (~ 31 km), intermediate ocean depth at the North Pole (~ 42 km) and a deep ocean at the South Pole (~ 51 km) (Čadek *et al.*, 2019). Saturn's

largest moon Titan also comprises a low amplitude, long wavelength deformed ice shell (Kvorka *et al.*, 2018) with possible heat flux heterogeneities at the high pressure ice mantle ocean floor (Choblet *et al.*, 2017*b*). Moreover, significant tidal dissipation in an unconsolidated Enceladan core could give rise to large lateral heterogeneities in ocean floor heat flux that may affect the oceanic heat transport processes (Choblet *et al.*, 2017*a*; Liao *et al.*, 2020).

Motivated by the unique properties of Enceladus' subsurface ocean, this work analyses the influence of a non-uniform shell container undergoing rotating Rayleigh-Bénard convection to determine its impact on heat transfer and flow behaviour and to question the direct applicability of plane layer (e.g., Cheng *et al.*, 2015; King *et al.*, 2012) and uniform shell scaling laws (e.g., Gastine *et al.*, 2016) to predict astrophysical flow regimes for non-uniform geometries. In particular, we model two fluid containers consisting of a uniform spherical shell and a non-uniform spherical shell that is deformed with a degree-2 spherical harmonic perturbation. The thermal forcing is increased from marginal supercriticality to weakly influenced by rotation.

This paper is organised as follows. We introduce the dynamical problem and numerical method of rotating convection in a spherical and non-uniform shell domain in Section 2.2. This is followed by the results of the heat transfer behaviour in Section 2.3 and we conclude the paper in Section 2.4.

2.2. Methods

2.2.1. Problem formulation

We simulate thermal convection of a Boussinesq fluid in both uniform and non-uniform spherical shells, rotating with constant rotation rate about $\boldsymbol{\Omega} = \Omega\hat{\boldsymbol{e}}_z$. The fluid is contained between the inner shell radius r_i and outer shell radius r_o, where we set the radius ratio $\chi = r_i/r_o = 0.8$. Gravity is assumed to vary linearly between the bounding radii and is normalised by the outer radius surface gravity g_o. The gravity profile is then described by $\boldsymbol{g} = -(g_o/r_o)\boldsymbol{r}$. The boundaries are impenetrable, have no slip and isothermal boundary conditions with an imposed superadiabatic temperature gradient ΔT between the boundaries. The governing Boussinesq equations are non-dimensionalised in length, temperature and time by the mean shell thickness $D = r_o - r_i$, superadiabatic temperature gradient ΔT and rotation period Ω^{-1} respectively, and are given by

$$\nabla \cdot \boldsymbol{u} = 0, \tag{2.1}$$

$$\frac{\partial \boldsymbol{u}}{\partial t} + \boldsymbol{u}\cdot\nabla\boldsymbol{u} + 2\,\hat{\boldsymbol{e}}_z \times \boldsymbol{u} = -\nabla P + Ek\nabla^2\boldsymbol{u} + Ra^*\frac{\boldsymbol{r}}{r_o}T, \tag{2.2}$$

$$\frac{\partial T}{\partial t} + \boldsymbol{u}\cdot\nabla T = \frac{Ek}{Pr}\nabla^2 T. \tag{2.3}$$

The non-dimensional Ekman, modified Rayleigh and Prandtl numbers are defined by

$$Ek = \frac{\nu}{\Omega D^2}, \quad Ra^* = \frac{\alpha_T g_0 \Delta T}{\Omega^2 D}, \quad Pr = \frac{\nu}{\kappa}. \tag{2.4}$$

where ν is the kinematic viscosity, κ the thermal diffusivity and α_T the thermal expansion coefficient. The modified Rayleigh number is related to the traditional Rayleigh number ($Ra = \alpha_T g_0 \Delta T D^3/\nu\kappa$) and convective Rossby number by

$$Ra^* = RaEk^2Pr^{-1} = Ro_c^2. \tag{2.5}$$

The convective Rossby number is independent of viscous and thermal diffusivities and defines a global force balance between buoyancy and Coriolis forces (Gilman, 1977). Appendix A.3 briefly describes the fluid problem for a non-rotating model of spherical shell convection to estimate an effective upper limit to rotating heat transport scaling behaviour.

2.2.2. Numerical domain

To analyse the influence on fluid behaviour of low degree shell deformation(s), as predicted for Enceladus' ocean (Beuthe *et al.*, 2016; Čadek *et al.*, 2019, 2016; Hemingway & Mittal, 2019), we adopt a spherical harmonic representation to deform the outer shell boundary of the uniform spherical shell with $\chi = 0.8$. We limit the numerical simulations to a zonal variation (i.e., $m = 0$), where the outer boundary is then

given by

$$r_o(\vartheta) = r_i + D\left[1 + \sum_{l=1}^{l_{\max}} \sum_{m=0}^{l} C_{lm} P_l^m(\cos\vartheta)\right], \tag{2.6}$$

where ϑ is the co-latitude, and l and m are the respective degree and order of the associated Legendre polynomial P_l^m (see e.g., Arfken *et al.*, 2013, for an overview on Legendre functions), and C_{lm} is the deformation coefficient. It is noted that the inner (core) radius r_i remains unaltered after modifying the grid's shape. The non-uniform spherical shell is then obtained by linearly transforming the uniform shell to a non-uniform shell where the outer boundary is described by Equation 2.6. Further, by using the spherical harmonic representation, we retain the mean shell thickness of D, which makes comparisons between both uniform and deformed geometries more consistent. In the current study, the influence of a deformed shell on rotating convection compared to a uniform shell is analysed with one variation, namely $C_{20} = 0.5$. A degree-2 harmonic deformation is chosen as it closely represents an Enceladan ocean that harbours a dominant degree-2 zonal shape (Beuthe *et al.*, 2016; Čadek *et al.*, 2019). Figure 2.1 shows the two numerical domains where we highlight the latitude-dependent outer radius and hence shell thickness for the non-uniform shell. We further assume that fluid layer has the same density as the inner core of the domain. We assume that there is no significant impact on the direction and magnitude of the gravity vector inside the fluid caused by a change in shell shape. The linear, radially-dependent gravitational profile in the momentum equation is therefore retained in this study.

In our model, the inner sphere (representing a rocky core) is an important characteristic in a spherical domain as it decouples the communication between two hemispheres when flow structures assume columnar modes that are aligned with the rotation axis in rotating convection (see Figure 2.1). This is characterised by the tangent cylinder with cylindrical radius r_i that intersects the inner sphere equator and is parallel to the axis of rotation. The intersection angle ϑ_t demarcates the division of the domain into three dynamical regions and is completely determined by the radius ratio for the uniform domain, $\vartheta_t = \sin^{-1}(\chi)$. Convective motions influenced by rotation inside the tangent cylinder are therefore disconnected from motions at the other hemisphere that are closely described by a shallow fluid layer similar to plane layer geometries (Cheng *et al.*, 2015). In a full sphere domain (i.e., no inner core), convective flows are allowed to traverse both hemispheres, which is similar to the region outside the tangent cylinder (Heimpel *et al.*, 2005). The spherical shell model furthermore has been found to comprise distinct tangent cylinder effects on varying convective flow characteristics and heat transfer behaviour (e.g., Al-Shamali *et al.*, 2004; Aurnou *et al.*, 2007; Aurnou & Olson, 2001).

2.2.3. Numerical method

We use the spectral element code Nek5000 (NEK5000, 2019) to solve the non-dimensional Boussinesq equations in a spherical shell domain, as given in Equations 2.1-2.3. The numerical domain is divided into quadrilateral and hexahedral elements, with each element discretised on a grid of Gauss-Lobatto-Legendre nodes. For each element, the variables are expressed as basis coefficients for Lagrange polynomials of order p. Integration in time is performed using a semi-implicit method, where linear terms are solved implicitly using a third-order backward difference formula and non-linear terms are solved explicitly with a third-order extrapolation scheme. See Appendix B for a more detailed coverage on the numerical method and performed benchmarks.

Various geophysical fluid dynamical problems have been studied using Nek5000 that incorporate mechanical forcings (e.g., Grannan *et al.*, 2017; Lemasquerier *et al.*, 2017; Reddy *et al.*, 2018; Vormann & Hansen, 2018) and (rapidly) rotating Rayleigh-Bénard convection (e.g., Favier *et al.*, 2019*a*; Vormann & Hansen, 2020). The numerical domain of the spherical shell model is a Cartesian cube projected onto a spherical shell grid as used in Vormann & Hansen (2018, 2020). In the radial direction near the boundaries, the grid is more refined to improve the resolution in the Ekman and thermal boundary layers. The grids used in this study range in element count from 8 640 to 96 228 with polynomial orders ranging between 7 and 12.

2.2.4. Parameter space and numerical resolutions

The parameter space of this work has been carefully selected based on the findings of previous work. Gastine *et al.* (2016) performed a systematic parameter study comprising a large range of Ek and Ra at $Pr = 1$, to study the dynamical convection regimes found in rotating spherical shell convection. Due to

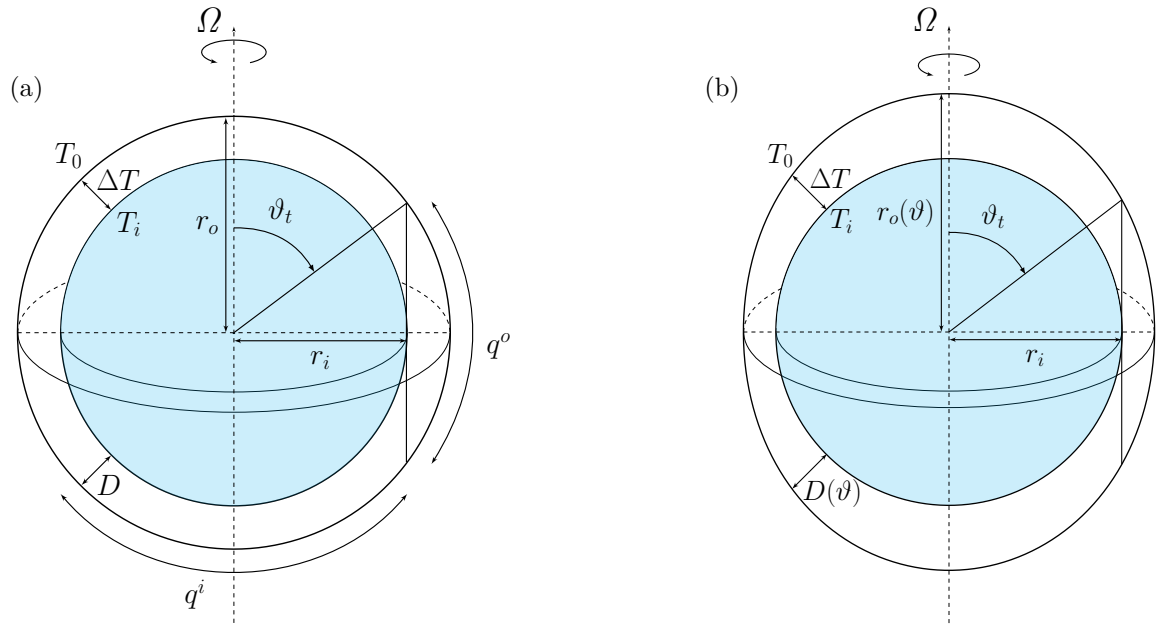

Figure 2.1: Schematics of the numerical model geometries of a uniform (a) and non-uniform (b) shell. Rayleigh-Bénard convection is initiation by the temperature difference $\Delta T = T_i - T_o > 0$, within a shell of thickness that is constant $D = r_o - r_i$ or dependent on co-latitude ϑ, $D(\vartheta) = r_o(\vartheta) - r_i$ for uniform and non-uniform geometries respectively. The complete system rotates at constant rotation rate about $\boldsymbol{\Omega}$. The co-latitude angle between the tangent cylinder of cylindrical radius r_i with the outer boundary surface is given by ϑ_t. The radius ratio of the uniform model is $\chi = r_i/r_o = 0.8$, which is similar for the non-uniform shell, noting that $S_o^{-1} \int_{S_o} r_i/r_o(\vartheta)\, dS_o = \chi$, where S_o is the outer surface area. The tangent cylinder demarcation on the outer surface is used to compare the heat flux inside and outside the tangent cylinder areas. In (a) the heat flux inside and outside the tangent cylinder is illustrated for the uniform geometry in (a) with q^i and q^o respectively. Note that q^i is computed from both the Northern and Southern hemispheres.

their use of a quadratic gravity profile, Gastine *et al.* (2016, 2015) were able to validate their numerical resolution using an analytical solution to the viscous dissipation rate. Taking into account time and computational limitations, we based this work's parameter space on these validated numerical resolutions and the detected rotating convection regimes in their parameter range. Our main focus is to study the different regimes of thermal convection at a sufficiently small Ekman number to approach more astrophysically relevant fluid behaviour (e.g., an $Ek \sim 10^{-10}$ is estimated for Enceladus as discussed in Section 1.1.4). Following this reasoning, we selected constant Ekman and Prandtl numbers of $Ek = 3\times10^{-4}$ and $Pr = 1$ respectively, and varied the thermal forcing in the range $1.6 \times 10^5 \leq Ra \leq 5.0 \times 10^6$, which is equivalent to $0.12 \leq Ro_c \lesssim 0.67$, as shown in Figure 2.2. In this range, we study thermal convection from onset at $Ra \gtrsim Ra_c$, to the transitional regime where rotational influence gradually succumbs to buoyancy forcing. The non-rotating regime is however not fully approached as shown in the figure, which required substantially higher resolutions to sufficiently resolve the fluid.

As discussed above, our radial and horizontal resolutions were selected to be comparable to Gastine *et al.* (2016). We furthermore perform a resolution check by comparing the mean grid width Δh of the numerical domain with the Kolmogorov length scale η_k, given by

$$\eta_k = \left(\frac{\nu^3}{\epsilon_U} \right)^{1/4}, \tag{2.7}$$

where ϵ_U is the time-averaged viscous dissipation rate given by

$$\epsilon_U = \overline{\left\langle \nu \left(\nabla \times \boldsymbol{u} \right)^2 \right\rangle_v}. \tag{2.8}$$

A posteriori, we have found that all simulations have resolutions comparable to the Kolmogorov length scale with $\eta_k/\Delta h \sim \mathcal{O}(1)$, where Δh is the mean grid width of the domain (see table A.1). Furthermore, we resolve the thermal boundary layers for all simulations with a number of grid points with at least 11 points, comparable to Stevens *et al.* (2010) who demonstrated sufficiently resolved thermal boundary

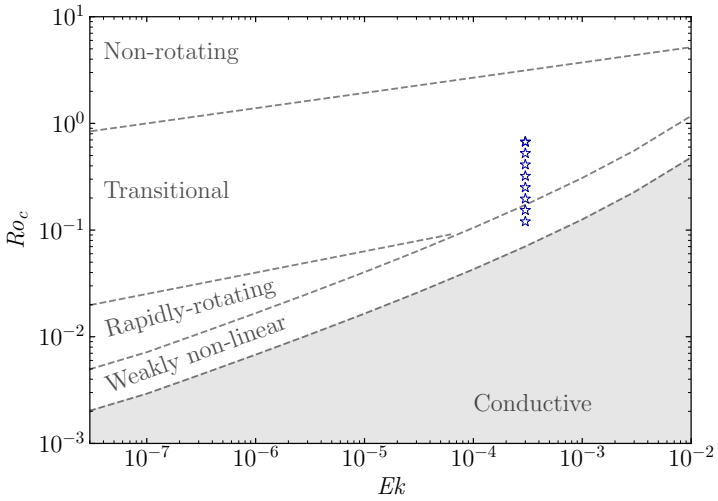

Figure 2.2: Parameter space of this study with a variable range of thermal forcing with $1.6 \times 10^5 \leq Ra \leq 5.0 \times 10^6$, equivalent to $0.12 \leq Ro_c \lesssim 0.67$, with a constant Ekman number of $Ek = 3 \times 10^{-4}$ and Prandtl number of $Pr = 1$. The range of simulations are indicated by the blue star symbols (see Table 2.1). The vertical axis shows the convective Rossby number, $Ro_c = (RaEk^2 Pr^{-1})^{1/2}$, and describes the relative influence of buoyancy to Coriolis forces. Convection regimes found in rotating spherical shell convection for a shell with $\chi = 0.6$ from Gastine *et al.* (2016) are annotated with dark gray text and dashed lines.

layers that properly dissipate the thermal energy. A summary on the grid resolutions is given in table A.1 of Appendix A.1.

2.2.5. Diagnostics

A number of diagnostic properties are recorded to determine the variability in flow behaviour associated with changing physical parameters. We introduce the following notations for averaging these parameters in time and space. Averaging in time for a given duration τ is denoted by an overline, defined for the temperature as

$$\overline{T} = \frac{1}{\tau} \int_{t_0}^{t_0+\tau} T \, d\tau. \tag{2.9}$$

Spatial averaging is performed horizontally over a surface for a fixed radial position, denoted by $\langle \dots \rangle_s$; over a volume V, denoted by $\langle \dots \rangle_v$; or zonally over constant latitude circles, denoted by $\langle \dots \rangle_\vartheta$. For example, for the temperature field we have

$$\langle T \rangle_s = \frac{1}{A} \int_A T \, dA, \quad \langle T \rangle_v = \frac{1}{V} \int_V T \, dV, \quad \langle T \rangle_\vartheta = \frac{1}{2\pi} \int_0^{2\pi} T \, d\varphi. \tag{2.10}$$

Horizontal averaging is employed to deduce internal field profiles as a function of the radius (e.g., temperature or velocity profiles) in a uniform model, that is furthermore used to compute boundary layer thicknesses. Given that a uniform spherical shell geometry and the thickness of its shell introduce asymmetries in the internal field profiles and boundary layer thickness estimations (Gastine *et al.*, 2015), we confine the horizontal averaging to the equatorial and North Pole regions to remove geometrical influences on the internal field profile estimations. These regions denote the two extreme latitudes in the domain that comprise the minimum and maximum radius ratios, and are integrated for elements that situate within an, arbitrarily chosen, small range of $\Delta\vartheta = 8°$.

The heat transfer efficiency as expressed by the Nusselt number is defined by the ratio of total heat transport, from both convection and conduction, to the transport of heat from conduction alone. For the uniform shell, the Nusselt number at the outer boundary is computed with

$$Nu = \frac{\chi Q D}{\rho c_p \kappa \Delta T} = \frac{\left. \dfrac{d\overline{\langle T \rangle_s}}{dr} \right|_{r=r_o}}{\left. \dfrac{d\overline{T_c}}{dr} \right|_{r=r_o}}, \tag{2.11}$$

using the time and horizontally averaged temperature field at the boundary and the conductive temperature profile T_c, which is obtained for a stationary flow ($\boldsymbol{u} = 0$) from the solution of the heat equation (Equation 2.3), given by

$$\frac{d}{dr}\left(r^2\frac{dT_c}{dr}\right) = 0, \quad T(r_i) = 1, \quad T(r_o) = 0. \tag{2.12}$$

This yields the analytical expression for the conductive temperature profile in a uniform shell

$$T_c(r) = \frac{r_i}{D}\left(\frac{r_o}{r} - 1\right). \tag{2.13}$$

We numerically compute the conductive temperature profile for the non-uniform domain by linearly projecting the uniform conductive temperature profile T_c onto the non-uniform grid using Equation 2.6. The governing equations are evolved in time with $Ra = 0$ to converge to a stable conductive temperature profile. Hence, the Nusselt number at the outer surface S_o can be computed using

$$Nu = \frac{\int_{S_o} \hat{\boldsymbol{n}} \cdot \nabla\overline{T}\, dS_o}{\int_{S_o} \hat{\boldsymbol{n}} \cdot \nabla\overline{T}\, dS_o\Big|_{Ra=0}}. \tag{2.14}$$

We furthermore compute the temperature gradient at mid-depth

$$\beta_T = \frac{d\langle\overline{T}\rangle_s}{dr}\bigg|_{r=r_m}, \tag{2.15}$$

where $r_m = (r_i + r_o(\vartheta))/2$. It is noted that the temperature gradient is computed at the respective mid-depths of the shell at the polar and equatorial latitudes for the non-uniform analyses. The dimensionless kinetic energy density is given by

$$\mathcal{E}_k = \frac{1}{2V}\int_V \boldsymbol{u}\cdot\boldsymbol{u}\, dV = \frac{1}{2}\left\langle \boldsymbol{u}\cdot\boldsymbol{u}\right\rangle_v. \tag{2.16}$$

The flow speed is characterised by the Reynolds number, given by

$$Re = \frac{\hat{U}D}{\nu} = \frac{U^{\mathrm{rms}}}{Ek} = \frac{\left(2\,\overline{\mathcal{E}}_k\right)^{1/2}}{Ek} \tag{2.17}$$

where $\hat{U}$ is the dimensional characteristic velocity, U^{rms} the characteristic non-dimensional rms velocity, $U^{\mathrm{rms}} = \left(V^{-1}\int_V \overline{\boldsymbol{u}\cdot\boldsymbol{u}}\, dV\right)^{1/2}$. We further extract the convective Reynolds number, Re_c, from the Reynolds number by omitting the axisymmetric zonal flow component u_φ in Equation 2.17, by transforming the velocity vector from a Cartesian coordinate frame to a spherical one, resulting in

$$Re_h = \frac{\overline{\left\langle\sqrt{u_\theta^2 + u_\varphi^2}\right\rangle_v}}{Ek}. \tag{2.18}$$

We further analyse the heat flux distribution at the outer surface between the area inside and outside the tangent cylinder for both geometries (see Figure 2.1). Following Amit *et al.* (2020), we define this mean heat flux contrast as

$$q^{\,i/o} = \frac{\langle\overline{q}\rangle_s^i - \langle\overline{q}\rangle_s^o}{\langle\overline{q}\rangle_s^i + \langle\overline{q}\rangle_s^o}, \tag{2.19}$$

where q is the heat flux at the outer boundary, and the indices i and o denote the surfaces inside and outside the tangent cylinder respectively. It must be noted that the surface average $\langle\ldots\rangle_s^{i,o}$ is only applied at either the inner or outer surface area of the tangent cylinder, as opposed to the full spherical surface area. The sign of the heat flux contrast denotes whether the heat flux is higher inside (i.e., positive), or outside (i.e., negative) the tangent cylinder. To measure the heterogeneity of the heat flux distribution, the extrema of the latitudinal heat flux profile, $\langle\overline{q}\rangle_\vartheta$ is used to define the mean heterogeneity expressed as

$$q^* = \frac{\max\left[\langle\overline{q}\rangle_\vartheta\right] - \min\left[\langle\overline{q}\rangle_\vartheta\right]}{2\langle\overline{q}\rangle_s}, \tag{2.20}$$

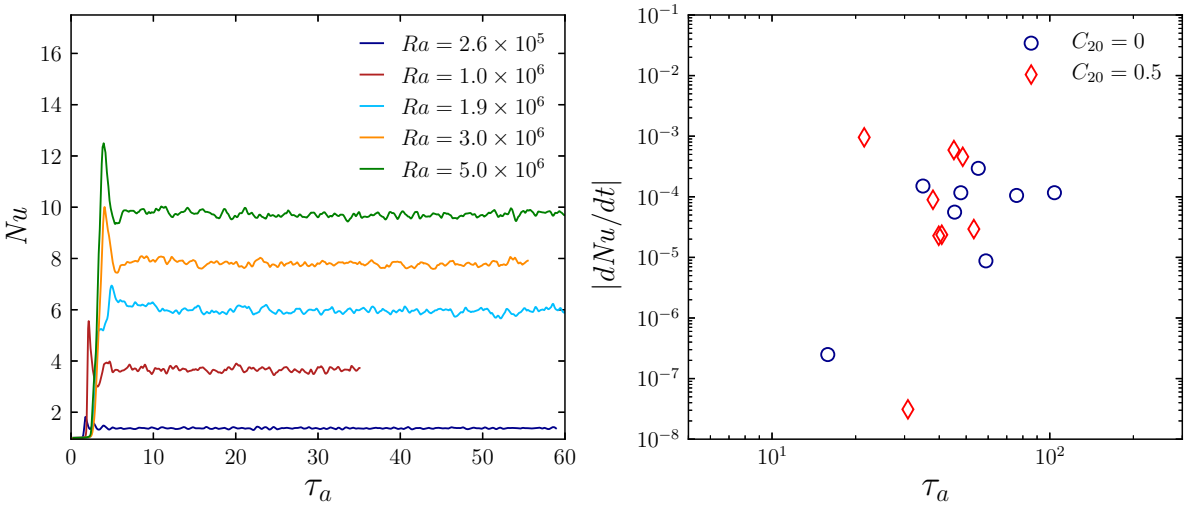

Figure 2.3: Temporal evolution of the Nusselt number for selected uniform geometry simulations (a) and mean temporal behaviour of Nusselt number (b), $|dNu/dt|$, plotted against the advection time unit τ_a to demonstrate converge properties. Colours in (a) denote the Rayleigh numbers of the respective simulations as shown in the legend. Colours and symbols in (b) denote the domain geometry with blue circles representing uniform and red diamonds representing non-uniform domains.

where all quantities are computed for the outer boundary at $r = r_o$. Traditional heat flux heterogeneity calculations predetermine heat flux extrema over the full boundary as input parameter. In our model, we measure the time-averaged heat flux that hence likely still contain localised high amplitude horizontal heterogeneities that may not accurately describe the global heat flux distribution. Therefore we follow Amit *et al.* (2020) by zonally averaging the heat flux to filter out any local deviations that arise from finite averaging and/or simulation times. Large heterogeneities denote strong amplitude differences in heat flux, whereas a zero heterogeneity denotes a perfect homogeneous distribution of the heat flux. Further, the time and zonally averaged, normalised heat flux profile at the outer boundary is given by

$$\langle \overline{q} \rangle_\vartheta^n = \frac{\langle \overline{q} \rangle_\vartheta}{\langle \overline{q} \rangle_s} - 1. \tag{2.21}$$

2.3. Results

In this study, we analyse the influence of the spherical shell geometry in rotating Rayleigh-Bénard convection on the flow and heat transfer behaviour and the applicability of heat transfer scaling laws. To analyse the various dynamical regimes (e.g., see Gastine *et al.*, 2016), we simulated 16 cases by varying the strength of thermal forcing, ranging from the weakly non-linear regime to the transitional regime, where rotational effects remain present (see Figure 2.2). The Rayleigh number is therefore varied between $1.6 \times 10^5 \leq Ra \leq 5.0 \times 10^6$, with $Ek = 3 \times 10^{-4}$ and $Pr = 1$. Table 2.1 lists the simulations performed in this study and summarises the most relevant output parameters.

Figure 2.3 (a) shows typical behaviour of the Nusselt number for selected simulations of the uniform model, which is similar to the non-uniform behaviour. Here, we introduce the advection time scale τ_a to physically characterise the mean time scale for a fluid parcel to traverse length scale D, with characteristic velocity U^{rms}. Every simulation is started from an initial static flow, $\boldsymbol{u} = 0$, with a conductive temperature profile (see Section 2.2.5) that is perturbed using a low degree and order spherical harmonic signal that vanishes at the boundaries to destabilise the system (see Appendix B.3.2). After the initial perturbation, the fluid behaviour is characterised by a delayed response in convective motion, followed by a sharp increase in heat transfer as identified by the Nusselt number that overshoots its statistical, time-averaged values. After the initial transient has passed, chaotic oscillations are generally found about this time-averaged mean, upon which the averaging operations are performed. We demonstrate the convergence of the averaged diagnostics with the Nusselt number in Figure 2.3 (b) from the average time rate-of-change, i.e., dNu/dt, taken over the time period after this initial transient. Generally, the averaged Nusselt numbers and other diagnostics quantities are computed for more than

Case	Ra	Nu	Re_c	Re	Ro	$\tilde{\epsilon}_U$	η_k	β_T	$q^{i/o}$	q^*
S_1	1.6×10^5	1.11	4.3	8.8	2.65×10^{-3}	1.35×10^{-3}	9.03×10^{-2}	−0.93	−0.09	0.17
S_2	2.6×10^5	1.38	10.4	19.6	5.89×10^{-3}	7.76×10^{-3}	5.84×10^{-2}	−0.85	−0.24	0.49
S_3	4.3×10^5	1.85	19.4	37.9	1.14×10^{-2}	2.93×10^{-2}	4.19×10^{-2}	−0.74	−0.42	0.76
S_4	7.0×10^5	2.71	33.8	65.4	1.96×10^{-2}	9.47×10^{-2}	3.12×10^{-2}	−0.61	−0.51	0.80
S_5	1.0×10^6	3.66	49.0	92.6	2.78×10^{-2}	2.12×10^{-1}	2.55×10^{-2}	−0.46	−0.43	0.71
S_6	1.9×10^6	5.96	83.5	159.1	4.77×10^{-2}	7.50×10^{-1}	1.86×10^{-2}	−0.28	−0.11	0.21
S_7	3.0×10^6	7.79	116.5	221.8	6.65×10^{-2}	1.62×10^{0}	1.54×10^{-2}	−0.22	0.02	0.13
S_8	5.0×10^6	9.69	162.6	308.2	9.25×10^{-2}	3.45×10^{0}	1.27×10^{-2}	−0.19	0.07	0.21
P_1	1.6×10^5	1.23	5.8	10.4	3.11×10^{-3}	2.28×10^{-3}	7.93×10^{-2}	−0.85	−0.38	0.67
P_2	2.6×10^5	1.49	10.4	19.0	5.69×10^{-3}	8.17×10^{-3}	5.77×10^{-2}	−0.80	−0.49	0.88
P_3	4.3×10^5	2.05	19.3	34.9	1.05×10^{-2}	2.93×10^{-2}	4.19×10^{-2}	−0.55	−0.61	0.99
P_4	7.0×10^5	2.96	33.8	59.3	1.78×10^{-2}	9.35×10^{-2}	3.13×10^{-2}	−0.30	−0.59	0.88
P_5	1.0×10^6	3.82	46.8	84.6	2.54×10^{-2}	2.06×10^{-1}	2.57×10^{-2}	−0.23	−0.43	0.70
P_6	1.9×10^6	6.05	82.5	153.0	4.59×10^{-2}	7.78×10^{-1}	1.84×10^{-2}	−0.11	−0.13	0.24
P_7	3.0×10^6	7.66	116.5	215.0	6.45×10^{-2}	1.69×10^{0}	1.52×10^{-2}	−0.08	−0.03	0.10
P_8	5.0×10^6	9.39	163.9	297.8	8.93×10^{-2}	3.57×10^{0}	1.26×10^{-2}	−0.06	0.00	0.14

Table 2.1: Summary of results from direct numerical simulations at $Ek = 3\times10^{-4}$ in a uniform spherical shell with $C_{20} = 0$ denoted by case numbers S_j, and non-uniform spherical shells with $C_{20} = 0.5$ denoted by case numbers P_j. The definitions for each of the output parameters can be found in Section 2.2.5.

30 advection time units with at the minimum 10 units and comprise trends that are in overall less than 10^{-3}. We will consistently apply these symbols and colours in the subsequent work to denote results with blue circles, ○, for uniform shells and with red diamonds, ◇, for non-uniform (i.e., $C_{20} = 0.5$) shells. For mathematical expressions, we make this distinction clear with superscripts u and nu, for the uniform and non-uniform geometries respectively. Due to the lack of sufficient data points to provide confident scaling relations, Appendix A.2 describes the estimations of thermal and Ekman boundary layer thicknesses using the time and horizontally averaged temperature, $\langle\overline{T}\rangle_s$, and horizontal velocity profiles, $\langle\overline{Re}_h\rangle_s$.

2.3.1. Flow field behaviour

The range of simulated rotating Rayleigh-Bénard convection regimes is demonstrated in Figure 2.4 with the temperature anomaly (i.e., $\overline{T} - \langle\overline{T}\rangle_s$) and axial vorticity (i.e., $\omega_z = \nabla_z \times \boldsymbol{u}$) fields shown for both geometries. Three cases of Ra are visualised that are representative of the various flow morphologies found in the studied parameter space. At low Ra (leftmost column), heat is transported via thermal convection columns that are aligned with the axis of rotation and convection is only active in the vicinity outside the tangent cylinder (i.e., equatorial region) where convection is expected to onset in spherical shells (Busse & Cuong, 1977; Dormy *et al.*, 2004; Zhang & Busse, 1987). Due to the weak buoyancy force relative to rotation, the flow dynamics are closely described by a quasi-geostrophic flow driven by the first order balance between the pressure gradient and Coriolis force (Davidson, 2013). As postulated by the Taylor-Proudman theorem (Davidson, 2013), these flows are (nearly) invariant in the direction of the rotation axis and hence move preferentially parallel to the equatorial plane. The curvature of the domain causes outward travelling columns to decrease their height, which breaks the Taylor-Proudman theorem and gives rise to thermal Rossby waves that travel in the prograde direction (i.e. direction of rotation) (Busse, 2002; Zhang, 1992). As these columns are inclined to conserve potential vorticity (PV) (i.e., analogue to conservation of angular momentum), this decrease in height requires a decrease in the columns' relative vorticity and cause the columns to tilt in the prograde direction (Busse, 2002; Zhang, 1992), as clearly shown in (a) and (d). This prograde deflection is weaker in the non-uniform model, see (g) and (j), where heat is transported in a shorter distance in the equatorial region and has locally a higher Ro_c as it is inversely related to D (see Equation 2.5). Furthermore, a higher azimuthal wavenumber measured at the equator, m, of the Taylor columns was found for the non-uniform shell,

with $m = 52$, compared to the azimuthal wavenumber for the uniform shell geometry, with $m = 44$. The critical wavenumber at onset scales with the circumference ratio of the inner shell radius with respect to the outer shell radius (Al-Shamali *et al.*, 2004), which is in agreement with the increased radius ratio for the non-uniform shell geometry at the equator.

For the intermediate Ra case (middle column), convection migrates to higher latitudes and columnar structures remain dominant in the equatorial regions ((e) and (k)), albeit that the axial coherence of these flow structures weaken. Near the equator in (b) and (h), warm thermal plumes form at the inner boundary equator as axially aligned structures with thin sheet-like warmer tails surrounded by a sea of colder fluid and develop mushroom-like heads that diverge at the outer boundary (e.g., Gastine *et al.*, 2015; Shishkina & Wagner, 2008). We find that the polar region in the non-uniform geometry convects for this Ra in (h), whereas the poles remain subcritical and dormant for the uniform geometry shown in (b). This can be explained by the local value of D which increases the local Rayleigh number with a cubic relation, $Ra_{loc} \sim D^3$, and decreases the local Ekman number with inverse quadratic relation, $Ek_{loc} \sim D^{-2}$. As the critical Rayleigh number follows the relation $Ra_c \sim Ek^{-4/3}$ (Chandrasekhar, 1961) in the limit of $Ek \to 0$, the local critical Rayleigh at the pole increases roughly by a factor of $1.5^{2\cdot(4/3)} \approx 2.95$, which is lower than the increase in local Rayleigh number by a factor of $1.5^3 = 3.375$. Hence, the polar region in the non-uniform geometry reaches more quickly the local critical Rayleigh number caused by the increase in shell depth.

In the highest simulated case of Ra (rightmost column), convection is vigorous at all latitudes (see (c) and (i)) and clearly demonstrates the weakening, yet still pertinent influence of rotation on heat transport. Heat is transported throughout the fluid domain with distinct differences in flow structure and behaviour between the equatorial and higher latitude regions. As shown in (f) and (l), vortices are dominantly present in mid to high latitudes, and in (c) and (i) we find large vertically elongated plume structures near the equator and smaller cellular structures at higher latitudes. These vortices are correlated with thermal plumes. Cyclonic vortices (i.e., rotating in direction of planetary rotation) are associated with regions of convergent flows where plume structures are formed. Complying with the conservation of mass, a rising (sinking) plume at the inner (outer) boundary requires the horizontal inflow of fluid towards the plume to replace the upward (downward) travelling fluid. The plume acquires positive vorticity from the feeding converging horizontal flow as conserves its angular momentum (e.g., Julien *et al.*, 1996). Further, the employed rigid mechanical boundary condition gives rise to Ekman boundary layers in rotating fluids that slow the horizontal flow down, causing it to spiral radially towards the center of the plume and thus supply a stronger convergent flow (Julien *et al.*, 1996) and additionally throttle the radial heat transport via Ekman pumping (Julien *et al.*, 2016; Plumley *et al.*, 2016). This is clearly shown in the polar region of the non-uniform geometry in (k) where axially aligned columnar structures have positive vertical vorticity in converging zones where plumes structures develop. At mid-depth, the sign of vertical vorticity changes where the vertical transport from a rising plume changes its role to supply horizontal flow towards plumes at the opposite boundary.

In Figures 2.5 and 2.6, time and zonally averaged temperature and velocity fields are shown for respectively the uniform and non-uniform geometries for the full range of Ra considered in this work. We show the temperature field, $\overline{T}$ in (a-e), the temperature anomaly with respect to the conductive state, $\overline{T} - T_c(r)$ in (f-j), the zonal flow velocity component, u_φ in (k-o), and the radial flow velocity component, u_r in (p-t).

With increasing Ra for both geometries, the temperature fields shown in (a-j) demonstrate the migration of convection starting at only the equator to higher latitudes until convection is present throughout the fluid domains. This migration is also associated with the transition from equatorial cooling, where heat is more efficiently transported in the equator, to polar cooling, where heat is more efficiently transported in the poles (Amit *et al.*, 2020). The interior temperature shown in (a-e) furthermore approaches an isothermal state with large temperature gradients located at both spherical boundaries. In (k-o), strong signatures of zonal flow components are found in both geometries and increase in magnitude with the increase of Ra. Prograde equatorial jets are generally found outside the tangent cylinder whereas retrograde jets are found near or inside the tangent cylinder. For (k-m) in the uniform geometry, the direction of zonal flows alternate with cylindrical radius (i.e., radius from center sphere and parallel to equatorial plane) with a persistent strong retrograde jet at cylindrical radius at mid-depth, i.e., $r = (r_i + r_o)/2$. A similar zonal flow distribution is found for the non-uniform geometry shown in (k-l), where alternating zonal flows are found with cylindrical radius from the equator. Interestingly, in (k) of the non-uniform geometry an internal weak prograde jet develops in the lowest

Ra model near the middle of the shell at the equator (i.e., $r = [r_i + r_o(\pi/2)]/2$), which is completely surrounded by retrograde zonal flows near the equator. With increasing Ra for the uniform domain shown in (n-o), two zonal jets develop that comprise a strong prograde equatorial jet outside the tangent cylinder and a retrograde jet at a higher latitude located inside the tangent cylinder. The zonal flow structures are similar for the non-uniform geometry as shown in (m-o), where prograde equatorial jets persistently form outside the tangent cylinder with, however, much higher speeds than the retrograde jet situated at smaller cylindrical radii. As discussed for the instantaneous 3D fields shown in Figure 2.4, the onset of convection is associated with prograde tilted convection columns that decrease their relative vorticity when travelling radially outwards. The tilt of these columns give rise to Reynolds stresses that transport momentum flux in the fluid and drive large scale zonal flows (e.g., Aurnou *et al.*, 2008, 2007; Aurnou & Olson, 2001; Busse, 1994). Reynolds stresses cause prograde angular momentum flux to be transported with outward travelling flows and retrograde angular momentum flux to be transported with inward travelling flows, hence generating the prograde jets at the equatorial region and retrograde jets at higher latitudes near or inside the tangent cylinder (e.g., Aurnou *et al.*, 2007). The radial velocity fields shown in (p-t) indicate the migration of equatorial-only flows to higher latitudes and demonstrate the increase of convective vigour (i.e., increasing Ra) with increasing radial speeds. For high Ra shown in (s) and (t) of both geometries, the persistent strong zonal flows in the equatorial region are found associated with relatively lower radial velocities in this region. These equatorial jets inhibit convective mixing at the equator such that heat transport becomes more effective in the polar region (Aurnou *et al.*, 2008) (see Section 2.3.5). In the polar region, the thermal forcing finally overcomes the rotational constraint and vigorously transports heat with radial circulation patterns reminiscent of localised Hadley circulation cells.

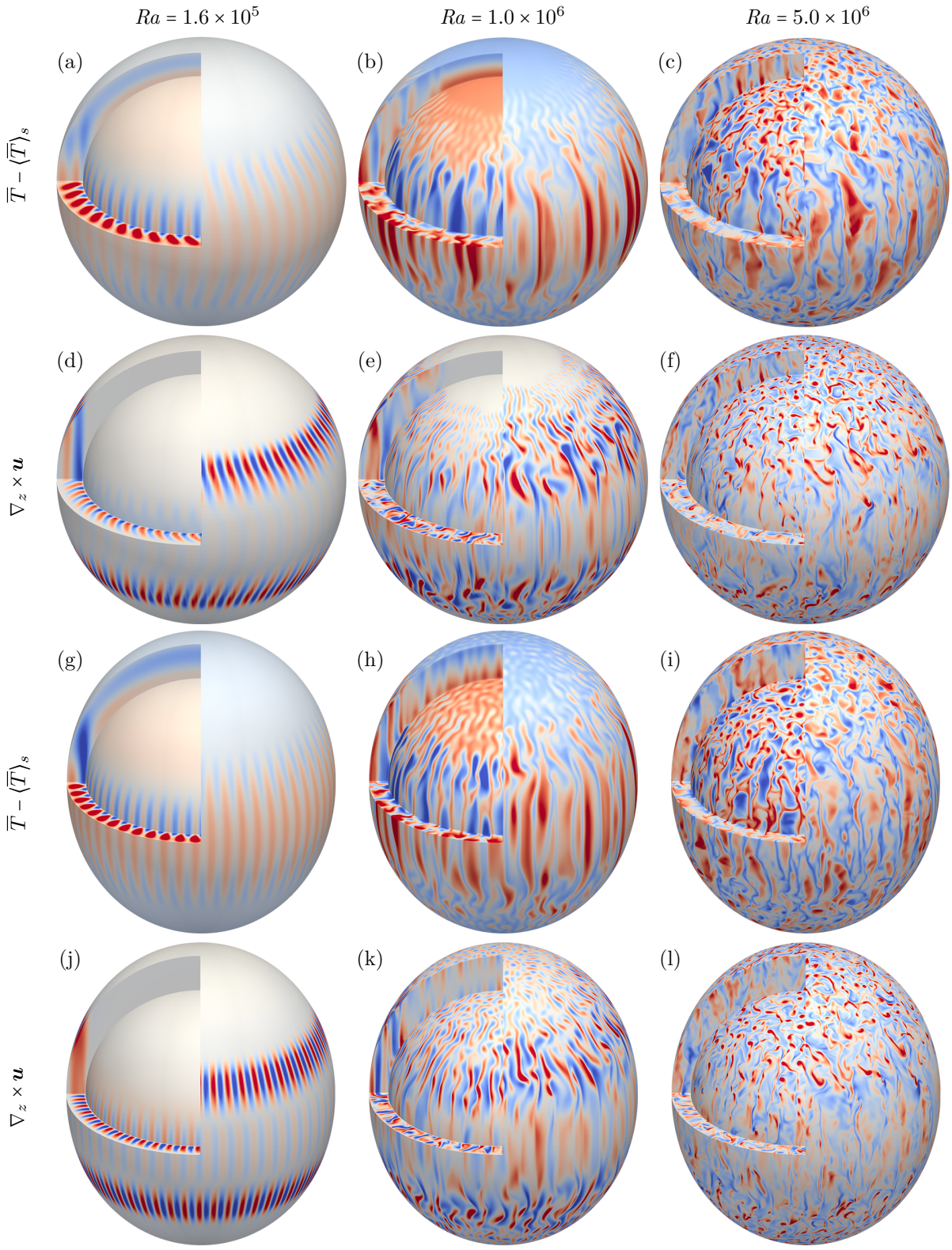

Figure 2.4: Three-dimensional instantaneous fields displaying the inner and outer core boundaries, and the meridional and equatorial slices of the temperature anomaly and axial vorticity for a thermal forcing range depicting characteristic behaviour throughout this study. The top two rows (a-f) demonstrate the results in the uniform domain and the bottom two rows (g-l) demonstrate the non-uniform domain with $C_{20} = 0.5$. Here, we depict the temperature anomaly given by $\overline{T} - \langle \overline{T} \rangle_s$ in (a-c) and (g-i) and the vorticity component in direction of rotation axis $\omega_z = \nabla_z \times \boldsymbol{u}$ in (d-f) and (j-l). Red/Blue indicate positive/negative components for both temperature anomaly and axial vorticity fields. The temperature and vorticity fields are obtained from the same time instant for a given domain geometry such that direct comparisons can be made between temperature and vorticity fields.

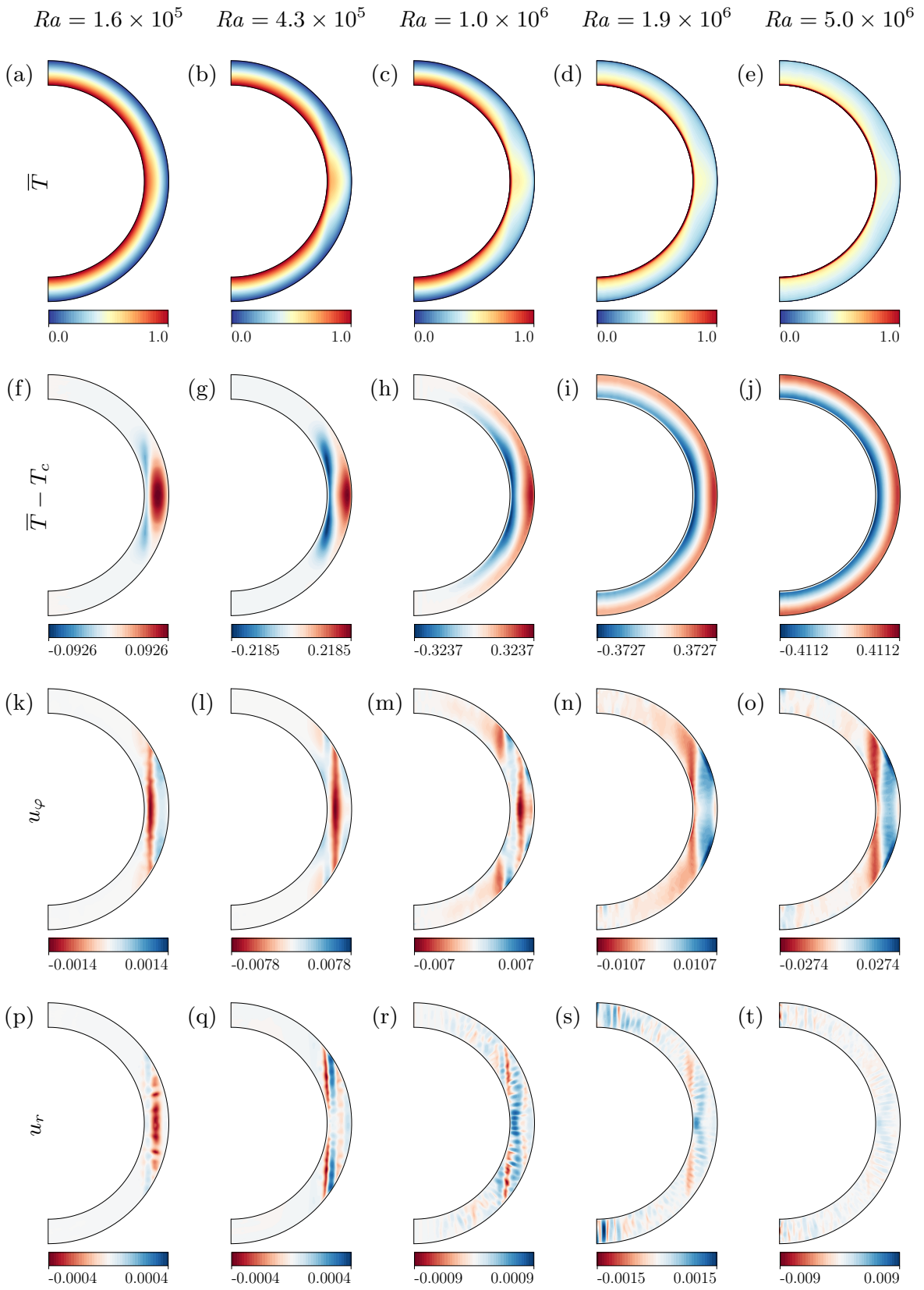

Figure 2.5: Time and zonally averaged meridional fields for the uniform model. From left to right, the Rayleigh number is increased from the lowest considered value just above critical, $Ra = 1.6 \times 10^5$, towards the highest considered value where rotational influences approach a subdominant role with $Ra = 5 \times 10^6$. From top to bottom, we show the temperature field (a-e), $\overline{T}$, the temperature difference with the conductive profile (i.e., equivalent to $Ra = 0$) (f-j), $\overline{T} - T_c$, the zonal (k-o), u_φ, and the radial (p-t), u_r, velocity components. The non-dimensional magnitudes of each field are given in the colourbar beneath each meridional slice.

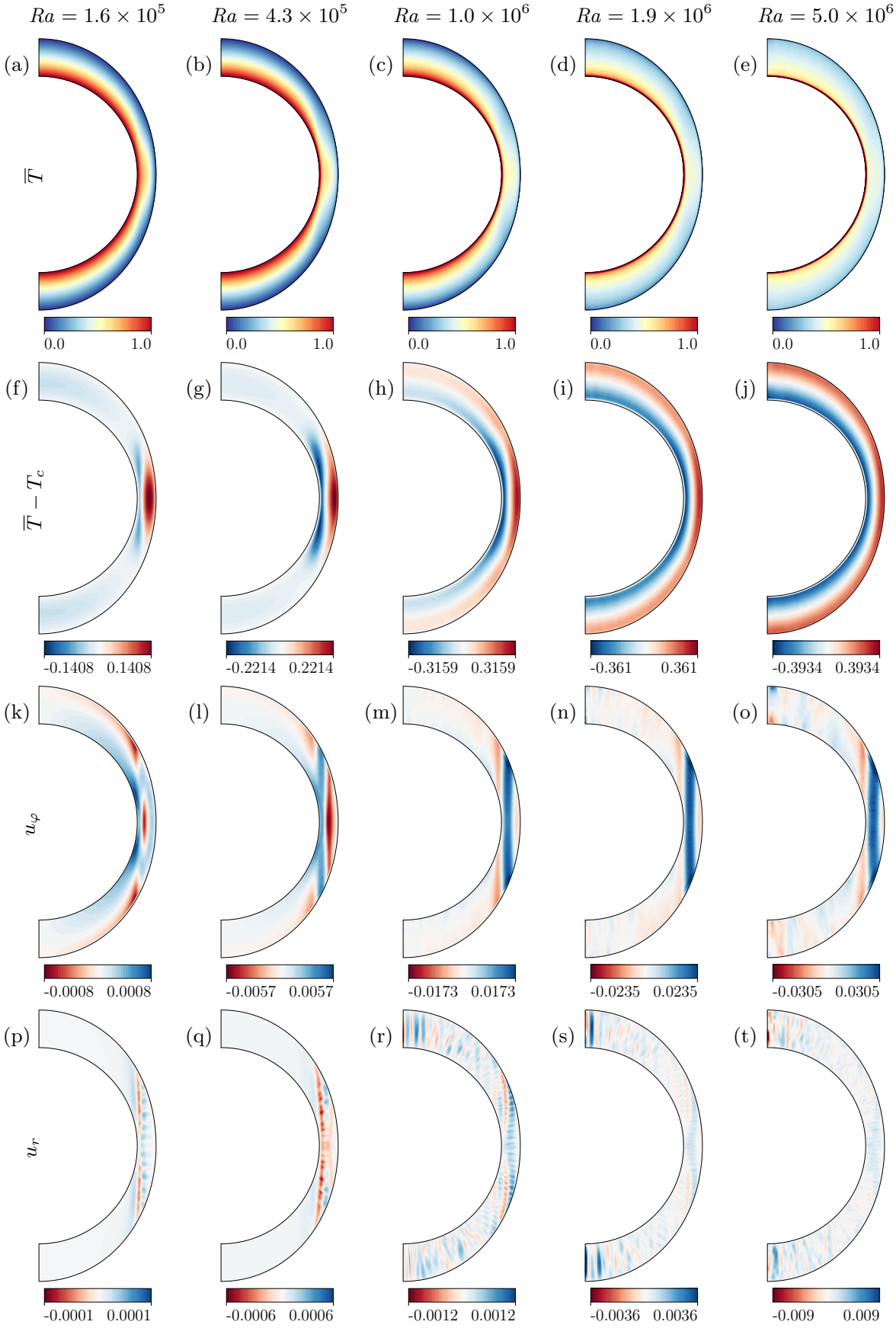

Figure 2.6: Time and zonally averaged meridional fields for the non-uniform model. From left to right, the Rayleigh number is increased from the lowest considered value just above critical, $Ra = 1.6 \times 10^5$, towards the highest considered value where rotational influences approach a subdominant role with $Ra = 5.0 \times 10^6$. From top to bottom, we show the temperature field (a-e), $\overline{T}$, the temperature difference with the conductive profile (i.e., equivalent to $Ra = 0$) (f-j), $\overline{T} - T_c$, the zonal (k-o), u_φ, and the radial (p-t), u_r, velocity components. The non-dimensional magnitudes of each field are given in the colourbar beneath each meridional slice.

2.3.2. Heat transfer scaling

The global heat transfer results are shown in Figure 2.7 (a) with colour and symbol indicating the uniform and non-uniform geometries. The variable meridional thickness $D(\vartheta)$ in the non-uniform domain introduces variable local Rayleigh and Ekman numbers. We incorporate this change in non-dimensional numbers using the convective Rossby number Ro_c, that quantifies the relative influence between Coriolis and buoyancy (see Equation 2.5). This is shown by the red shaded region that ranges accordingly with a minimum magnitude at the pole(s) and maximum magnitude at the equator as $Ro_c \sim D^{-1}$. Furthermore, the black solid line shows the heat transfer data from non-rotating simulations with $\chi = 0.8$ in a uniform spherical shell geometry determining the theoretical heat transfer upper limit for rotating spherical shell convection (see Appendix A.3). On the whole, the behaviour of the Nusselt number curve with increasing Rayleigh numbers shows similar characteristics as found in previous studies on rotating convection in spherical shell (e.g., Gastine *et al.*, 2016; Long *et al.*, 2020; Mound & Davies, 2017) and in plane layer geometries (e.g., Cheng *et al.*, 2015; King *et al.*, 2009). Just after onset of convection, where $Ra \gtrsim Ra_c$, the Nusselt number increases proportionally with the Rayleigh number, which is described by the weakly non-linear regime (Gastine *et al.*, 2016). With increasing Rayleigh numbers the curve is described by the transitional regime (Gastine *et al.*, 2016) where the Nusselt number increases more rapidly as demonstrated by the steeper slope, and upon even further increase in Rayleigh number, the slope levels off in the direction of the non-rotating heat transfer curve. As shown in the previously mentioned studies (e.g., Gastine *et al.*, 2016; Long *et al.*, 2020; Mound & Davies, 2017), we hypothesise that the Nusselt number curve for our rotating convection spherical shell model shall conform to the non-rotating curve as the rotational influence becomes negligible with further increase of the Rayleigh number. Nonetheless, it is noted that the range of Rayleigh numbers in our study does not incorporate the asymptotic non-rotating regime, considering that we observe notable rotational influence for the complete parameter range studied (see e.g., Figure 2.4). Differences in heat transfer behaviour is found between the two geometries. Up to roughly $Ra = 1.9 \times 10^6$ or $Ro_c \approx 0.41$, the Nusselt number for the non-uniform domain is higher than the uniform domain, which is associated with predominant equatorial heating (see Section 2.3.1), which is stronger in the non-uniform domain. This transitions into a lower Nusselt number when polar convection becomes more effective with higher Ro_c.

The relative difference between the Nusselt number estimations for the two geometries is displayed in Figure 2.7 (b). Close to onset, the Nusselt number of the non-uniform model is enhanced by roughly 10% and decreases for $Ra \geq 7.0 \times 10^5$. When $Ra > 1.9 \times 10^6$, this relation transitions in favour of a higher Nusselt number for the uniform model, where heat transport is more efficient in the polar region (e.g., Amit *et al.*, 2020) (see Section 2.3.5). This transition from equatorial to polar convective modes were well described in Amit *et al.* (2020) by the transitional Rayleigh number Ra_T, $Ra_T = 10Ek^{-3/2}$ (Amit *et al.*, 2020; King *et al.*, 2012), demarcating the zones of dominant equatorial heat transport, for $Ra/Ra_T < 1$, and zones of dominant polar heat transport, for $Ra/Ra_T > 1$. The scaling of Ra_T predicts the transition from quasi-geostrophic towards weakly rotating convection regimes, based on boundary layer stability analysis (King *et al.*, 2012). The attenuation of heat transport at the polar region for the non-uniform model can be explained by the reduction of Ro_c as it scales to shell thickness by $Ro_c \sim D^{-1}$ (see Equation 2.5). This further highlights that the competition between the Ekman and Rayleigh number in the polar region provides two interesting perspectives. First, we found that for the thicker shell the onset of convection is found earlier as Ra_c increases less than the local increase in Ra due to the increased thickness (see Section 2.3.1), which demonstrates that onset is controlled by fluid viscosity. Second, the combination of Coriolis and buoyancy in the thicker shell describe an overall less effective heat transport as Ro_c is decreased compared to a thinner shell, indicating that the interior bulk fluid behaviour is well described by the force balance, which is independent of viscous and thermal diffusivities, between rotation and buoyancy. Since we expect that heat transport homogenises in the asymptotic non-rotating regime for spherical shell domains (e.g. Gastine *et al.*, 2016), we hypothesise that the Nusselt number estimations for both geometries converge with increasing Ra.

The transitional regime is described by the steeper heat transfer curve highlighted in Figure 2.8 and is associated with increasing buoyancy force relative to the Coriolis force, such that the stabilising role of rotation gradually succumbs to convection. In this range of supercriticalities, rotating convection heat transfer scales much steeper than ordinary non-rotating spherical shell convection (e.g., Cheng *et al.*, 2015; Gastine *et al.*, 2015). The scaling relation for this transitional regime is linearly fitted using a normalisation of the critical Rayleigh number $Ra_c = 1.02 \times 10^5$ estimated for a shell of radius ratio $\chi = 0.8$ (Al-Shamali *et al.*, 2004; Amit *et al.*, 2020). Estimation of the critical Rayleigh number in the

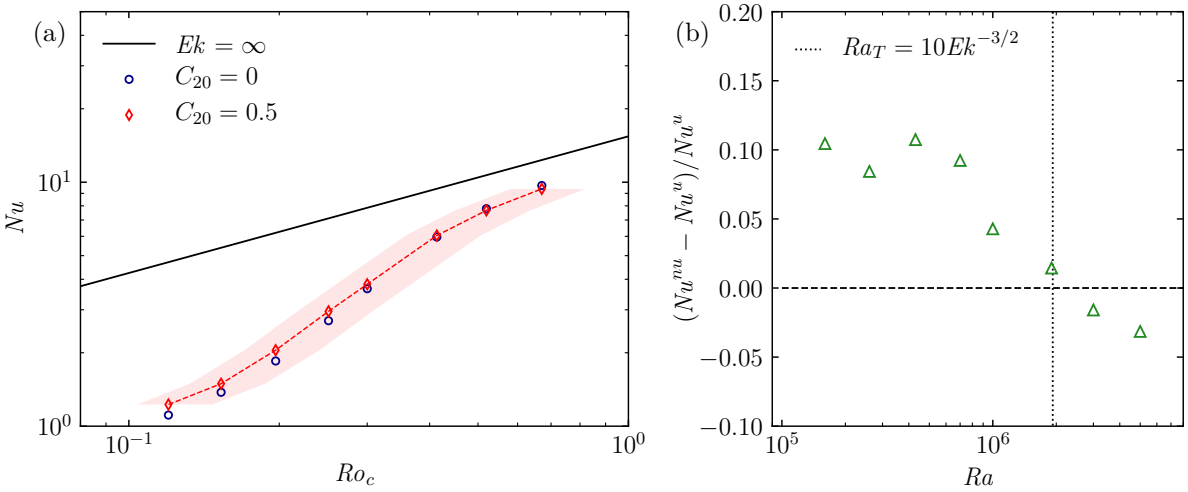

Figure 2.7: Relation Nusselt and convective Rossby numbers for a constant Ekman number $Ek = 3 \times 10^{-4}$ for the two shell geometries denoted by colour and shape (a), and the relative difference between the Nusselt estimates of both geometries (b). In (a), the solid black line is the effective Nusselt upper boundary for a given Rayleigh number found in non-rotating convection, given by $Nu = 0.164Ra^{0.280}$ (see Appendix A.3). The shaded red area demarcates the range of effective convective Rossby numbers introduced by the variable shell thickness $D(\vartheta)$ as it scales by $Ro_c \sim D^{-1}$ (see Equation 2.5). The leftmost value is associated with poles for for $D = 1.5$ and the rightmost value with the equator for $D = 0.75$. In (b), the relative difference in Nusselt number estimations from (a) are computed between the two domains and displayed by the green triangles. The vertical dotted line shows the transitional Rayleigh number, Ra_T, from King *et al.* (2012), indicating that this parameter roughly describes the 'transition' where Nu becomes higher in the uniform model compared to the non-uniform model.

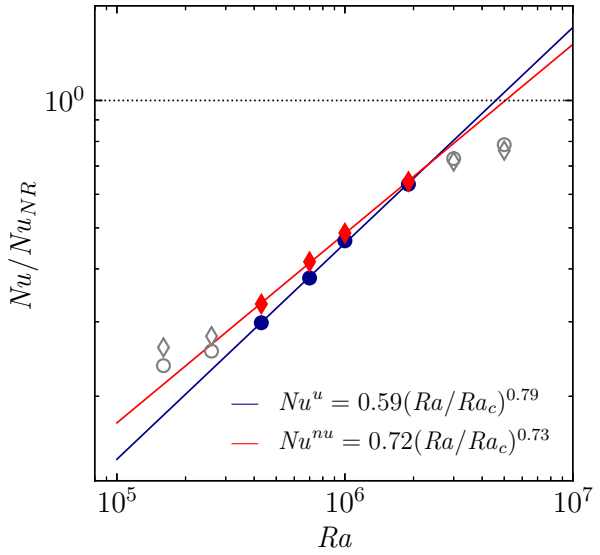

Figure 2.8: Normalised Nusselt number as a function of the Rayleigh number. The non-rotating Nusselt number normalised this study's rotating Nusselt number for the uniform model with $Nu_{NR} = 0.164Ra^{0.280}$ (see Appendix A.3) and the critical Rayleigh number Ra_c is obtained from Al-Shamali *et al.* (2004); Amit *et al.* (2020) to normalise the curve fit. We demarcate the 'transitional' regime inside $1.5 \leq Nu \leq 7.5$ (e.g., Gastine *et al.*, 2016; Julien *et al.*, 2012). Grey empty symbols demonstrate excluded data points in least square fit. The horizontal dotted line is the normalised non-rotating Nusselt number.

non-uniform model is an interesting endeavour, however this was not the aim of this work. By scaling the $Nu - Ra$ relation for the non-uniform geometry with the same Ra_c for the uniform geometry, only the prefactor constant will change in the estimation process. This yields the following heat transfer scaling relations for the uniform and non-uniform models respectively,

$$Nu^u = 0.594(Ra/Ra_c)^{0.790}, \qquad Nu^{nu} = 0.724(Ra/Ra_c)^{0.727}. \tag{2.22}$$

Here, only the Nusselt numbers higher than 1.5 and lower than 7.5 are considered for the fitting using the unweighed least squares method. The scaling exponents are in good agreement with the findings of Long *et al.* (2020) who found an exponent of 0.72 for $Ek = 3 \times 10^{-4}$. We further find that the slope of the scaling is slightly steeper for the uniform spherical shell compared to the non-uniform shell, which can be explained by the slower progression of heat transfer from equatorial to polar modes. That is, the variable shell thickness $D(\vartheta)$ enhances the heat transfer in the equatorial region (i.e., $D(\vartheta) < 1$) as the convective Rossby number scales as $Ro_c \sim D^{-1}$, and oppositely diminishes the heat transfer in the polar region (i.e., $D(\vartheta) < 1$).

2.3.3. Flow speed scaling

In attempt to determine and compare the dominant interior flow force balances, we look at the scaling behaviour of the convective flow speeds using the convective Reynolds numbers (see Section 2.2.5). Rotationally constrained flow is considered geostrophic when the pressure gradient is completely balanced by the Coriolis force. These flows are effectively constrained to two dimensions and are invariant in the direction of the rotation axis as postulated by the Taylor-Proudman theorem (Davidson, 2013). The Taylor-Proudman constraint must be broken to enable the transport of heat via thermal convection. A force balance between the viscous, Coriolis and Archimedean (i.e., buoyancy) forces (VAC) is found when the viscous force has a comparable magnitude to the Archimedean force (Gastine *et al.*, 2016; King *et al.*, 2013; King & Buffett, 2013). In a similar fashion, the Coriolis-Inertial-Archimedean (CIA) force balance is found when this constraint is broken as a result of inertia. For either triple-force balance assumptions, the differences only lie in the characteristics length scale of the flow, where the VAC follows $l \sim Ek^{1/3}D$ and CIA is described by the Rhines convection scaling $l \sim Ro^{1/2}D = (Re_c Ek)^{1/2}$ (Gastine *et al.*, 2016; King *et al.*, 2013; King & Buffett, 2013). The typical flow speed scaling of the VAC force balance (Gastine *et al.*, 2016; King *et al.*, 2013; King & Buffett, 2013) is given by

$$Re_c \sim Ra_Q^{1/2} Ek^{1/2}, \tag{2.23}$$

where $Ra_Q = Ra(Nu - 1)$ is the heat flux based Rayleigh number. The scaling following a CIA force balance (Gastine *et al.*, 2016; King *et al.*, 2013; King & Buffett, 2013) is given by

$$Re_c \sim Ra_Q^{2/5} Ek^{1/5}. \tag{2.24}$$

Since our parameter study only varies the magnitude of Ra for a fixed value of Ek, the least squares curve fitting is performed on $Re_c = \alpha Ra_Q^{\beta}$, where prefactor α incorporates the Ekman number and exponent β gives an indication on the appropriate force balance scaling. We find the following fitted curves for respectively the uniform and non-uniform geometries (see Figure 2.9)

$$Re_c^u = 0.0499\, Ra_Q^{0.463}, \qquad Re_c^{nu} = 0.0399\, Ra_Q^{0.475}. \tag{2.25}$$

Both curve fits are in marginally better agreement with the VAC force balance compared to the CIA balance, however it must be noted that the scaling exponents for Ra_Q are similar for both force balance models (i.e., 0.5 and 0.4 for VAC and CIA respectively). Particularly in the range $Re_c \leq 50$, the curve has a steeper slope compared to larger convective Reynolds numbers where we find a closer estimate of the 1/2 scaling exponent with, $Re_c^u = 0.0380\, Ra_Q^{0.486}$ and $Re_c^{nu} = 0.0364\, Ra_Q^{0.482}$. It is expected that the CIA scaling is not approached as the viscous boundary layers considerably influence the bulk fluid for large Ekman numbers (King *et al.*, 2013). Other studies (e.g., Gastine *et al.*, 2016; Long *et al.*, 2020) find similar agreement of the VAC force balance for relatively low magnitudes of Re_c and similar Ekman numbers, and approach the CIA force balance for large Re_c and small Ek where dissipation in the fluid bulk dominates.

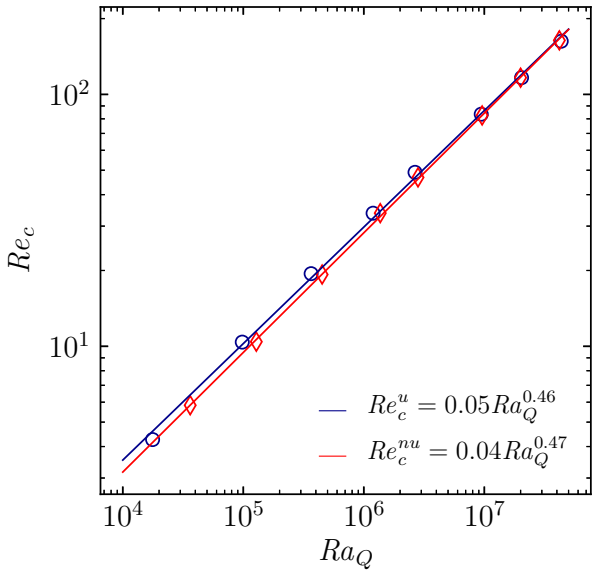

Figure 2.9: Convective Reynolds number scaling for the uniform and non-uniform models. The horizontal axis shows the flux-based Rayleigh number, $Ra_Q = Ra(Nu - 1)$. The curve fitted results are shown in the bottom right-hand corner with blue and red lines denoting the least squares fitted curves for the uniform and non-uniform models respectively. This is furthermore indicated by the superscripts of Re_c, with u indicating uniform and nu indicating non-uniform models.

2.3.4. Interior heat transfer

The interior fluid mixing driven by convection is demonstrated by the time and zonally averaged temperature profiles shown in Figure 2.10 (a) for the uniform geometry. As opposed to non-rotating convection, the turbulent transport of heat in the bulk fluid is constrained by the Coriolis force and convection is not occurring at all latitudes for low Ra. The temperature profiles for these partially convective cases are therefore similar to the purely conductive profile which is nearly linear (see Equation 2.13). With increasing Ra, the influence of rotation decreases, convection onsets at higher latitudes and stronger temperature gradients arise at the inner and outer boundaries. These boundary regions comprising large temperature gradients describe the thermal boundary layers that predominantly transfer heat through conduction (King *et al.*, 2012). This increase in thermal forcing is accompanied by a gradual decrease of the thermal gradient $-\beta_T$ at mid-depth (i.e., $r = (r_i + r_o)/2$), shown in Figure 2.10 (b), from nearly 1 for the conductive profile, to approximately 0.2 for $Ro_c = 0.67$. Beyond this value, the temperature gradient is anticipated to diminish for an isothermalised interior fluid bulk that is well-mixed, whenever the rotational influence becomes negligible in a non-rotating convection regime (e.g., Gastine *et al.*, 2016, 2015). Furthermore, as $-\beta_T$ decreases, the temperature drop in the thermal boundary layers increases, the boundary layer thickness decreases, and the rotating model approaches a regime where the heat transfer is predominantly characterised by both inner and outer thermal boundary layers with strong convective mixing occurring in the interior bulk fluid (Gastine *et al.*, 2016).

As employed above, the horizontally averaged interior profiles in a uniform spherical shell geometry are traditionally obtained by horizontally averaging the time-averaged solution fields (following Equation 2.10). Given the dependence of shell thickness on ϑ for the non-uniform model, we separately look at the local temperature profiles in the polar and equatorial regions (see 2.2.5). To make direct comparison's with the uniform model possible, the same methodology of analysing the two regions separately is applied to the uniform domain as displayed in Figure 2.11. Comparing Figures 2.10 and 2.11, it is clear that steeper temperature profiles are found at the equator compared to the poles, which onset for higher Ra.

Figure 2.12 shows the temperature profile for the non-uniform geometry at the equator (a) and the pole (b) at mid-depths of the local shell thickness. These temperature profiles are largely similar across the two geometries (see Figures 2.11 and 2.12). Convection onsets first in the equatorial region, is more developed in this region, and convective mixing is continuously increased with Ra as the interior temperature approaches an isothermal state. This progression of isothermalising the interior bulk fluid is demonstrated with $-\beta_T$ as shown in Figure 2.13. This indicates that the asymptotic non-rotating regime (i.e., $\beta_T = 0$) is closely approached in the equatorial region for both geometries, whilst strong

rotational effects impede vigorous interior mixing in the polar region. Here, the equatorial region behaves similar across the two geometries, but the polar region shows larger differences. The conductive profile at the pole in the non-uniform case is accompanied with a lower β_T compared to the uniform model and onsets for lower Ro_c. Based on the above findings, it must be noted that the traditional horizontal averaging process shown in Figure 2.10 highlights a dampening effect on the estimated temperature profile and subsequently the interior temperature gradient. Since not all latitudes convect in the studied parameter range, temperature gradients tend to be maximised at the equator and minimised at the poles, which could lead to misguiding interpretations in global temperature distribution and gradients at the boundaries used for scaling analysis of the thermal boundary layer.

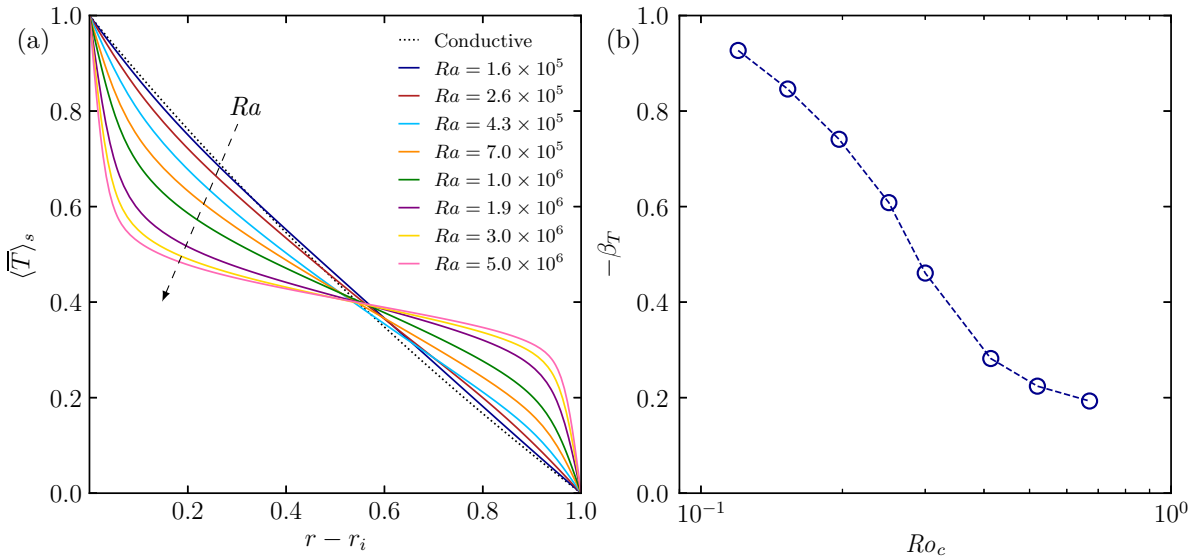

Figure 2.10: Interior heat transfer characterisation of the uniform model using the time and zonally averaged temperature profile (a) and the associated temperature gradient at mid-depth (i.e., $r = (r_i + r_o)/2$) (b). The arrow indicates the progression of the temperature profile with increasing thermal forcing of Ra.

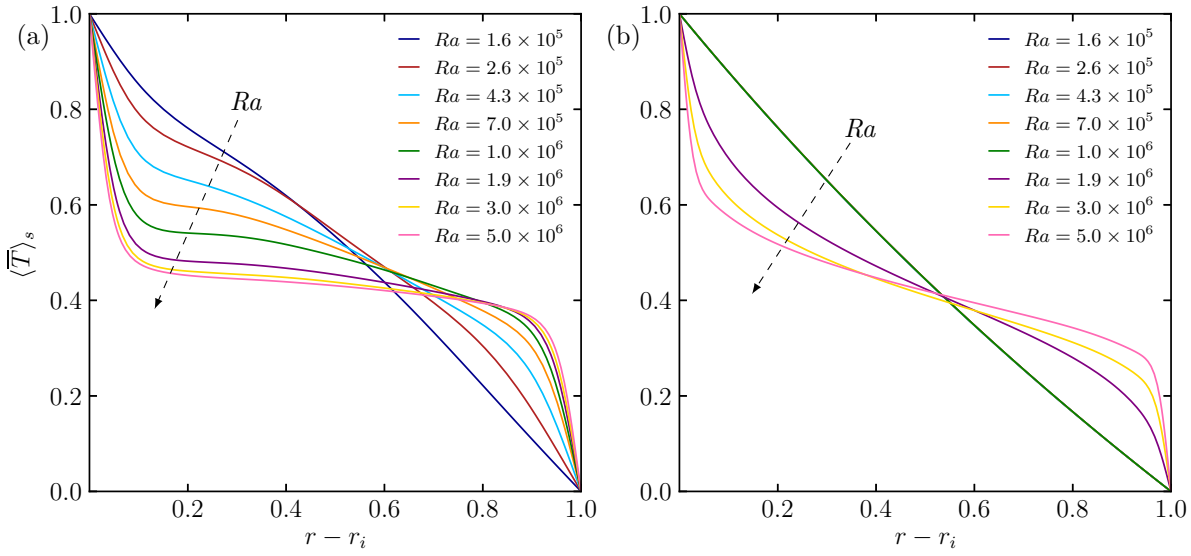

Figure 2.11: Interior temperature profiles averaged in time and spatially of the uniform model at the equator (a) and the North Pole (b) to allow direct comparison with the non-uniform temperature profile. The arrows indicate the progression of the temperature profile with increasing thermal forcing of Ra.

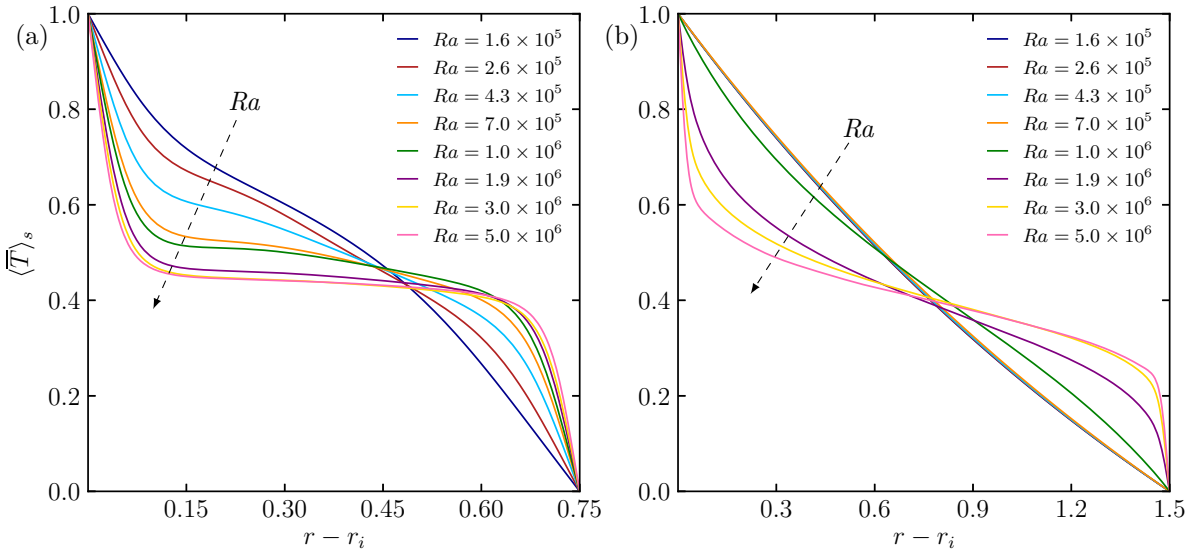

Figure 2.12: Interior temperature profiles averaged in time and spatially of the non-uniform model at the equator (a) and the North Pole (b). The arrows indicate the progression of the temperature profile with increasing thermal forcing of Ra.

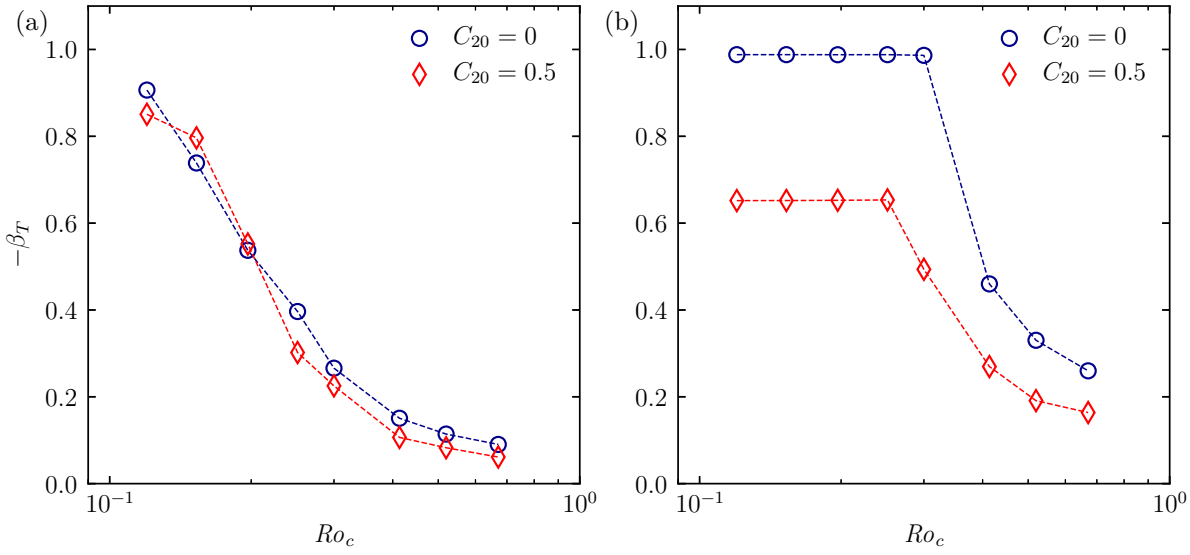

Figure 2.13: Interior temperature gradients for the uniform and non-uniform models at mid-depth (i.e., $r(\vartheta) = (r_i + r_o(\vartheta))/2$ for the non-uniform model and $r = (r_i + r_o)/2$ for the uniform model) from the time and spatially averaged temperature profiles in Figure 2.12 at the equator (a) and North Pole (b). The domain geometry is indicated by colour and symbol, with blue circles denoting the uniform geometry, and red diamonds denoting the non-uniform geometry.

2.3.5. Outer boundary heat flux

Previously we analysed the influence of shell geometry on the global behaviour of the Nusselt number with increasing Ra. To better characterise the interior heat transport behaviour associated with these global diagnostics, we analyse the non-dimensional heat flux distribution measured at the outer boundary of both domains.

Figure 2.14 shows the normalised zonally averaged heat flux distributions (see Equation 2.21) for both the uniform and non-uniform shells. For uniform cases with $Ra \leq 7.0 \times 10^5$, a relative increase in heat flux is observed at the equatorial region for increasing Ra. Notably, these cases exhibit a purely conductive mode at high latitudes. This is especially apparent for $Ra \leq 4.3 \times 10^5$, where the tangent cylinder clearly demarcates the region of convection and conduction. Upon further increase of Ra, the rotational constraint on convection is overcome at the polar regions. These cases remain however strongly influenced by rotation, as indicated by the columnar structures are formed in alignment with the axis of rotation (see e.g., Figure 2.4). This alignment promotes convective heat transport in the direction of the rotation axis, and due to the stronger equatorial zonal flows, convective heat transfer is more inhibited near the equatorial regions (Aurnou *et al.*, 2008). Because of this, heat is more efficiently transported in the polar region relative to the equatorial region for the two highest Ra cases.

The non-uniform heat flux distribution follows a similar pattern where convection first onsets at the equatorial region approximately bounded by the tangent cylinder, and increases in strength in this region with Ra for $Ra \leq 7 \times 10^5$. Note that the non-uniform profiles show a variable heat flux at the polar regions for low Ra. This is explained by the conductive heat flux that varies meridionally in a non-uniform shell, as opposed to latitude-independent conductive heat flux profile for the uniform shell (see Equation 2.13). As a result of this latitude-dependent heat flux distribution, larger differences between polar to equatorial heat fluxes are measured. For $Ra \geq 1.0 \times 10^6$, convection in the polar region onsets earlier in the non-uniform domain than the uniform domain, followed by a transition to (slightly) more efficient heat transfer at the poles compared to the equator with increased Ra.

Figures 2.15 (a) and (b) compare the heat fluxes between the two geometries for a common Ra, given by $\Delta q = q^u - q^{nu}$, with positive values marking regions where heat fluxes are higher in the uniform domain. On the whole, the impact of domain geometry in the non-uniform model is visible in the conductive heat flux curves as dT/dz (see Equation 2.11) is decreased at the poles and increased at the equator. This results in the decrease and increase of the heat flux at respectively the poles and equator for a conductive state, which is depicted by the positive Δq in the polar regions where the polar heat flux is higher for the uniform geometry. In the lower range of Ra (Figure 2.15 (a)), convection occurs mainly in the equatorial region, except for $Ra = 1.0 \times 10^6$ where convection onsets at the poles for only the non-uniform model. Here, increasing Ra from $Ra = 1.6 \times 10^6$ to $Ra = 7.0 \times 10^6$, is associated with stronger differences in Δq caused by the more effective equatorial heating in the non-uniform domain. In the range $7.0 \times 10^5 \leq Ra \leq 3.0 \times 10^6$, a maximum in the heat flux curve appears at the equator. This is explained by a wider heat flux profile at the equatorial region for the non-uniform model, caused by the flattened geometry in this region (see Figure 2.1), and narrower profile for the uniform model, thus giving rise to the local maximum and two minima at the equatorial region. For the simulations with $Ra = 1.0 \times 10^6$ and $Ra = 1.9 \times 10^6$, the polar regions measure similar heat fluxes across the two domains, which is caused by the delayed onset of convection at the poles for the uniform model. With further increase of Ra, the increased thickness at the pole of the non-uniform domain lowers Ro_c, resulting in a continuously increasing difference in heat flux at the polar region, whilst this difference in heat flux remains similar in the equatorial region. Interestingly, Δq approaches zero for high Ra at the latitudes for which the shell thickness in the non-uniform geometry equals the uniform shell thickness, as rotational influence on flow structures becomes secondary. That is, at $D(\vartheta) = D = 1$, for co-latitudes $\vartheta = \cos^{-1}(\pm(1/3)^{1/2}) \approx [0.955, \pi - 0.955]$ (see Equation 2.6), heat transport likely becomes comparable when approaching a non-rotating regime.

To further analyse the heat flux transitioning from equatorial bounded heat transfer at relatively low Ra to enhanced heat transfer at the polar regions, we show the heat flux contrast that compares heat flux contributions based on the tangent cylinder demarcation in Figure 2.16 (a) (see Equation 2.19). Here, negative values indicate more efficient heat transfer at the equatorial region (i.e., outside the tangent cylinder) and positive values indicate more efficient heat transfer at the polar region (i.e., inside the tangent cylinder). Figure 2.16 (b) represents the heat flux heterogeneity at the outer surface boundary (see Equation 2.20) where the magnitude measures the amount of latitudinal heat flux variation. With the polar regions convectively dormant for $Ra \leq 4.3 \times 10^5$, equatorial heat transfer becomes more efficient

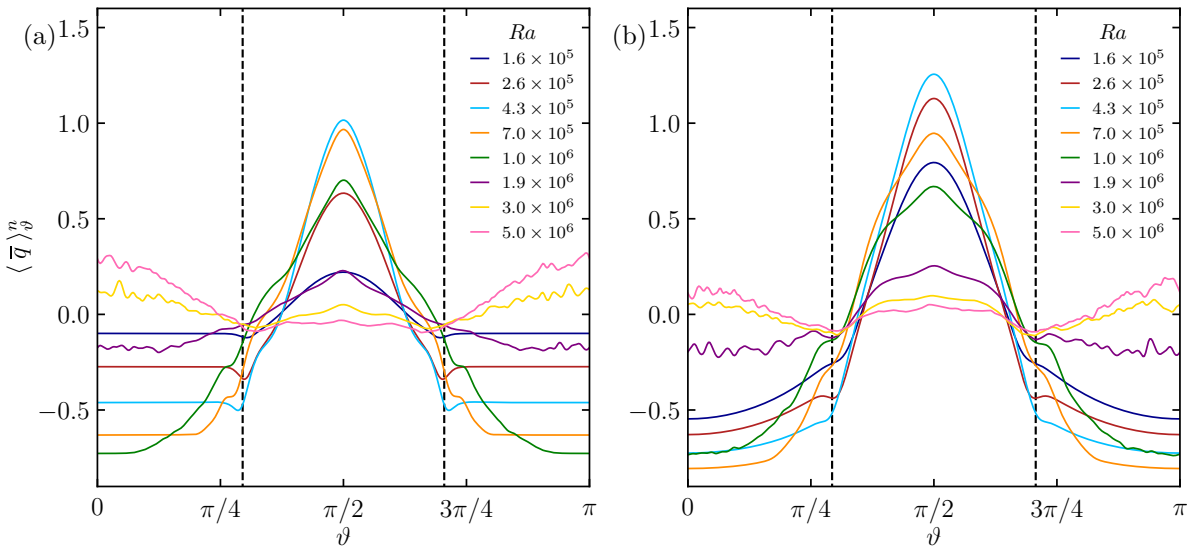

Figure 2.14: Time and zonally averaged normalised heat flux profiles for uniform (a) and non-uniform (b) spherical shell geometries using Equation 2.21. The tangent cylinder angle ϑ_c, unique to each geometry, is shown by the black dashed vertical lines.

with increasing Ra in the form of convective columns exclusively outside the tangent cylinder (Figure 2.14). Up to $Ra \approx 7 \times 10^5$ for the uniform model and $Ra \approx 4.3 \times 10^5$ for the non-uniform model, the peak values of equatorial heat transfer are reached, as demonstrated by the gradual increase of the heat flux contrast in Figure 2.16 (a). After these maxima, convective motions gradually become more prominent inside the tangent cylinder, which reduces the heat flux contrast. A similar behaviour is naturally found for the heat flux heterogeneity in (b), that increases from onset to its maximum amplitude at the regime where equatorial heat transfer is most dominant. Consistent with Amit *et al.* (2020), the heat flux contrast and heterogeneity both reduce in magnitude with increasing Ra when higher latitudes overcome the rotational constraint and start to convect (see e.g., Figure 2.14). Interestingly, the heat flux contrast changes sign when full sphere convection in the uniform domain is achieved, i.e., $Ra = 1.9 \times 10^6$, thereby demonstrating the strong preference of convective columns to align with the axis of rotation and enhance heat transport in this direction. In contrast, the heat flux contrast for the non-uniform geometry suggests a change in sign only for $Ra > 5.0 \times 10^6$, even though convection is more developed in the poles at lower Ra. The heat flux contrast of polar dominated heat flux regimes is notably smaller than equatorial heat flux dominated regimes and does not suggest a strong increase in magnitude, especially for the non-uniform domain, upon further increase of Ra beyond 5.0×10^6. This can be explained by the still active heat transfer in the equatorial region for regimes where heat transfer is slightly more dominant at the poles, as opposed to the only conductive heat flux contribution of the poles in equatorial dominated regimes. As Ra increases further beyond 5.0×10^6, the Coriolis force becomes ever weaker compared to the buoyancy force, causing the fluid flow to lose its tendency to move in the direction of the rotation axis. The convective system therefore approaches non-rotating Rayleigh-Bénard convection and assumes a more homogeneous distribution of outer boundary heat fluxes such that both the heat flux contrast and heterogeneity approach 0 for $Ra > 5 \times 10^6$ (e.g., Amit *et al.*, 2020).

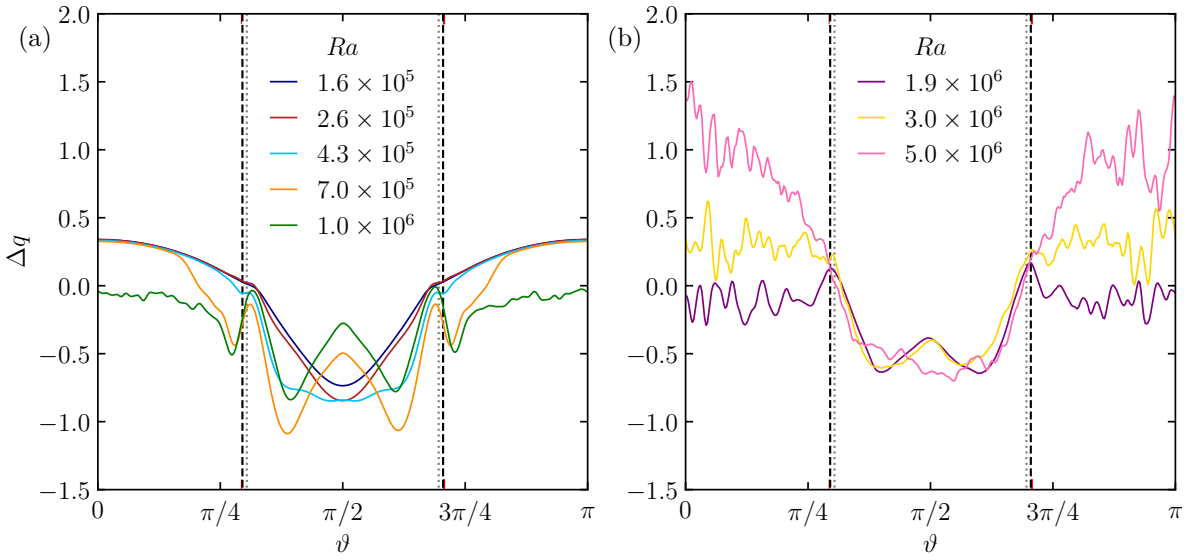

Figure 2.15: Comparison of non-dimensional heat flux profiles between the uniform and non-uniform geometries. The magnitude of the difference is given by $\Delta q = q^u - q^{nu}$, where heat flux profiles q^u is associate with the uniform and q^{nu} with non-uniform geometries. Cases with a conductive-only mode in the pole of the uniform geometry are shown on the left (a) and cases that are fully convecting are shown on the right (b). The tangent cylinder angle ϑ_{tc} is shown for the uniform shell by the black dashed vertical lines. The non-uniform tangent cylinder angle differs only slightly, as shown by the red axis ticks on the top and bottom. The dotted grey vertical lines mark the co-latitudes where the shell thickness is equal to 1 for both geometries.

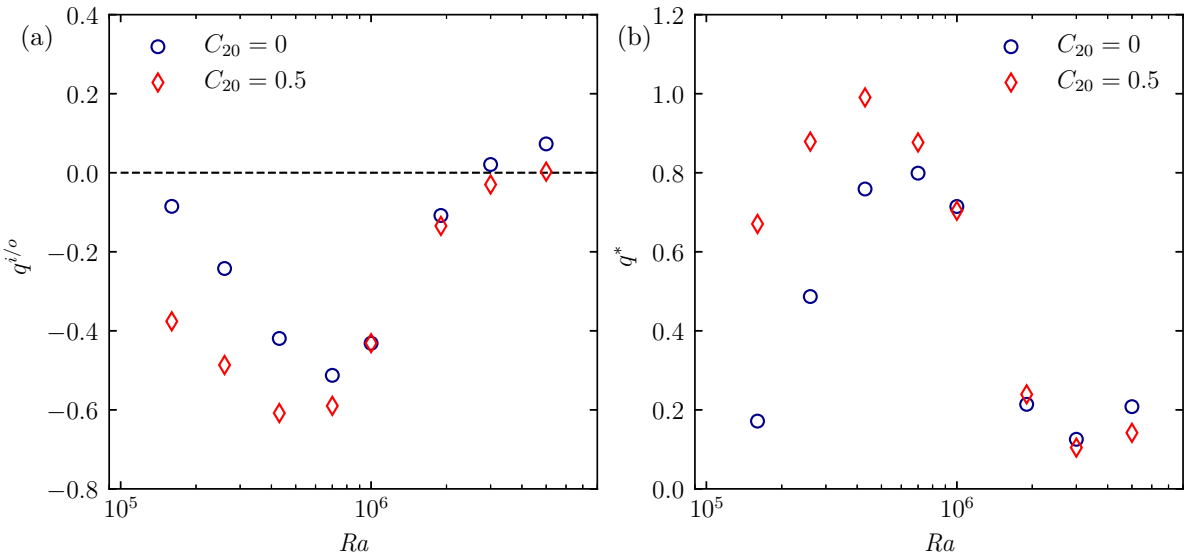

Figure 2.16: Relative contributions of outer boundary heat flux between regions outside and inside the tangent cylinder (a) using Equation 2.19 and the heat flux heterogeneity measurement (b) using Equation 2.20. Colour and symbol denote the model geometries as indicated in the legend and the horizontal dashed black line in (a) divides the equatorial (negative, outside cylinder) and polar (positive, inside tangent cylinder) dominated heat flux regions.

2.4. Conclusions

In this study we presented a model for rotating thermal convection in a non-uniform spherical shell geometry that better approximates the imperfectly shaped interior ocean layer of Enceladus. In particular, we focussed on the effects of domain geometry on flow structure and heat transfer behaviour by simulating varying flow regimes for the range of Rayleigh numbers, $1.6 \times 10^5 \leq Ra \leq 5.0 \times 10^6$, for constant Ekman, $Ek = 3 \times 10^{-4}$, and unity Prandtl numbers. This parameter space recovered previously identified flow regimes (e.g., Gastine *et al.*, 2016), from onset of convection with the weakly non-linear regime to flows that become less affected by rotation in the transitional regime. In this range, we further find flow behaviour that is reminiscent of the non-rotating regime, where the influence of rotation gradually diminishes in favour of strong buoyancy.

Our results of the uniform model demonstrate that, with increasing Ra, convection onsets at the equator and migrates to a fully convecting domain that gradually becomes less affected by rotation. As identified by previous studies (e.g., Gastine *et al.*, 2016; Long *et al.*, 2020) flows initially follow the predicted quasi-geostrophic flows aligned with the rotation axis, where heat is transported efficiently to the equatorial regions, succeeded by a transitional regime where rotation strongly influences convection throughout the spherical domain. Consistent with literature, we find that enhanced heat transfer efficiency is characterised by a steep $Nu - Ra$ scaling with an exponent of 0.79, and flows are best characterised by the force balance between viscosity, buoyancy and Coriolis (VAC) for the lower range of Ra with $Re_c = 0.038 Ra_Q^{0.49}$. Beyond $Ra = 1.0 \times 10^6$, strong zonal flows inhibit heat transfer in this region and focus this energy towards the polar regions where heat transfer becomes more efficient and is likely further enhanced by Ekman pumping effects associated with rigid mechanical boundary conditions. Asymptotic behaviour towards a non-rotating regime is suggested by the $Nu - Ra$ relation, the diminishing internal temperature gradient β_T and outer boundary heat flux contrast.

The non-uniform model exhibits similar regime development with low-Ra associated with dominant equatorial convection to marginally more effective polar convection modes at high Ra. In comparison to the uniform model, heat transfer scaling in the transitional regime is found less effective with a shallower $Nu - Ra$ scaling exponent of 0.73, although the interior flow at low supercriticalities can similarly be described by the triple force balance VAC with $Re_c = 0.036 Ra_Q^{0.48}$. Due to the deformation of the domain, heat fluxes were found universally higher at the equatorial region compared to the non-uniform geometry, resulting in enhanced integrated heat flux estimations for equatorial-only convective systems. Further, with increasing Ra an increasingly stronger heat transport is measured at the polar region for the uniform domain compared to the non-uniform domain caused by the larger shell thickness in this region, which explains the shallower transitional heat transfer scaling. Projections of the heat flux contrast and heterogeneity for the non-uniform model for high Ra beyond the present parameter space suggest weaker overall polar heat transfer and it approaches more readily a homogeneous distribution of heat across the outer surface. In the context of the Enceladan ocean, Čadek *et al.* (2019) estimated a meridional heat flux distribution with strong polar amplitudes more than twice the magnitude of the equatorial minimum. Hence, our results of the non-uniform model may indicate that stronger polar and weaker equatorial convective transport is required to favour polar heating and equatorial cooling in the context of a long-term stable Enceladan ocean, for instance by strong ocean floor heat flux heterogeneity (Choblet *et al.*, 2017*a*; Liao *et al.*, 2020).

Several limitations and opportunities of this study should be considered. The parameter space lacks sufficient range and density for a confident scaling analysis allowing for predictions to astrophysical parameter regimes. Nor did we perform simulations near the non-rotating regime Ra, leaving an estimation of asymptotic behaviour to high Ra undetermined. With decreasing Ek, a rapidly rotating flow regime is anticipated comprising thin axial flow structures that more efficiently transport heat possibly caused by the dominant role of Ekman pumping in the polar regions (Cheng *et al.*, 2015; Gastine *et al.*, 2016; Julien *et al.*, 2016; Stellmach *et al.*, 2014). We analysed the influence of one dominant long wavelength thickness profile (i.e., $C_{20} = 0.5$) that is symmetric with respect to the equator. Breaking the symmetry of this domain can provide unique insights into (local) flow structure development and its relation to heat transfer efficiency. The subsurface oceans in icy moons, including Enceladus, are likely saline (Khurana *et al.*, 1998; Mitri *et al.*, 2014; Postberg *et al.*, 2011; Zimmer *et al.*, 2000) and could influence the convective behaviour if the oceans are stratified (Radko, 2013). In this study, we assume a vigorously convecting ocean such that any transient stratification is quickly dissolved into a well-mixed, unstratified ocean. Shallow layers at the boundaries are likely more prone to double-diffusive convection

caused by brine rejection from freezing and fresh-water influx from a melting ice layer (Goodman *et al.*, 2004; Melosh *et al.*, 2004). Due to water's negative expansivity property from melting temperature up to ~ 4 degrees (at 1 bar pressure), fresh melt water could form a buoyant lens on top of the warm convecting bulk fluid (Melosh *et al.*, 2004). Enceladus' characteristic degree-2 zonal ice shell thickness profile (Čadek *et al.*, 2019, 2016; Hemingway & Mittal, 2019) and the predicted strong heat flux injected into the ocean (Choblet *et al.*, 2017*a*; Liao *et al.*, 2020) suggests that this thin layer likely does not prevent heat transport to the ice shell. Nevertheless, assuming that the variable ice shell thickness is actively maintained via oceanic heat transport, large regions of ice accretion and melt could be sustained for respectively the equatorial and polar regions, thereby imposing meridional circulation cells (Lobo *et al.*, 2020).

Mechanical forces are important for the generation of heat to keep the subsurface ocean liquid, may provide turbulent instabilities (e.g., precessional, librational or tidal instabilities) and could enforce ocean circulation (e.g., Cébron *et al.*, 2010*b*; Grannan *et al.*, 2017; Lemasquerier *et al.*, 2017; Reddy *et al.*, 2018; Rovira-Navarro *et al.*, 2019). The collective influence of these external forces with thermal convection on ocean circulation remains uncertain. Further work on this problem can be done by considering each of the prior mentioned mechanical forces in combination with thermal convection. Another interesting direction for icy moon subsurface ocean dynamics is combining our model with the effects of a heterogeneous ocean floor heat flux that could promote localised heat transfer at the polar regions (Choblet *et al.*, 2017*a*; Liao *et al.*, 2020) and help answer the question whether ocean circulation and/or heterogeneous ocean floor heat flux control regional melting and freezing of the overlying ice shell.

Exploration of the subsurface oceans in icy moons remain inherently difficult as the outer ice shell inhibits the direct observations of the oceans and in-situ observations (e.g., with landers) are currently only proposed (e.g., Pappalardo *et al.*, 2013). Two missions are planned to explore the icy satellites in the Jovian system that could allow for better characterisation of the subsurface oceans in relation to our results. Both ESA's JUICE and NASA's Europa Clipper missions will help constrain the thickness profile of Europa's ice shell layer and the characteristics of the underlying subsurface ocean. Temperature variations at the surface of the moon and ice shell thickness variations, measured respectively with thermal imaging and ice-penetrating radar observations, can help characterise the ice-ocean system by locating active sites where strong oceanic heat transport can induce regions of strong melt and enforce transport of heat through the ice shell via conduction or solid-state convection (e.g., Bruzzone *et al.*, 2013; Hayne *et al.*, 2017; Soderlund *et al.*, 2020). Furthermore, strong ocean current could potentially be detected via magnetic field observations from the induced magnetic field conducted through the ocean, and thus further constrain oceanic flows in future models (Tyler, 2011; Vance *et al.*, 2020).

3

Conclusions and recommendations

This work presented the development of a numerical tool suitable to simulate rotating thermal convection in deformed spherical shell domains using a spectral element solver. In these domains, we solved the Boussinesq equations for an ocean described by a variable meridional thickness profile and no-slip isothermal boundaries. In this framework we adopted the dominant shape of the predicted subsurface ocean of Enceladus with a degree-2 zonal harmonic deformation where the ocean in the poles is substantially deeper than in the equator. We explored the influence of deformed spherical shells on heat transfer behaviour and flow structure development across several flow regimes controlled by the magnitude of thermal forcing. Below, we describe the main conclusions of this work (Section 3.1) and provide recommendations for further work on this topic (Section 3.2).

3.1. Conclusions

To identify the effects of domain geometry, we have simulated a uniform geometry with constant shell thickness with a radius ratio of $\chi = 0.8$ and a deformed geometry with the same mean shell thickness. By varying the degree of thermal forcing with Ra, we gradually decrease the relative influence of rotation (i.e., by increasing Ro_c) and analyse the effects on flow behaviour and heat transport. In relation to previous work, we provided a new dimension to study icy moon ocean dynamics by introducing a topographical influence and we envision further improvements by incorporating conditions that are more representative of the icy moon under study.

Convection onsets outside the tangent cylinder in the equatorial region for both geometries in the form of convection columns that are characterised by thermal Rossby waves. With increasing thermal forcing, we find that the region of convection increases gradually from the equator towards higher latitudes until the domain is fully convecting. The transition to this fully convecting stage is marked by the transition where convection becomes dominant in the polar region for the uniform geometry. Due to the larger thickness in the polar region for the non-uniform geometry, convection is found to onset with lower Ra. Strong zonal flows develop in both geometries with increasing Ra, characterised by a prograde equatorial jet outside the tangent cylinder and a retrograde jet inside the tangent cylinder. With the highest thermal forcing cases, the combination of strong zonal jets impeding radial outflow at the equator and cellular-like heat transport at the poles gives rise to a strong relative polar heat transport.

In the transitional regime, where convection gradually occurs at higher latitudes with increasing Ra, we found that global heat transfer scaling for both geometries is in agreement with literature. Here, heat transfer is most efficient where the highest scaling exponent found in the $Nu - Ra$ relation. Due to the impeding impact of the thicker shell height at the poles in the non-uniform geometry, this heat transfer was found slightly diminished compared to the uniform geometry. In both geometries, scaling of the flow speed, Re_c, indicated that the internal fluid flow is described by a triple-force balance between viscosity, buoyancy and Coriolis (VAC).

With the results found in the current parameter space, the projected behaviour towards higher Ra of the heat flux contrast and heterogeneity suggests that weaker variability remains for the non-uniform geometry compared to the uniform geometry. This projection further suggests that the non-uniform

geometry diminishes large asymmetries found in heat flux distribution, where strong differences in polar or equatorial cooling are dampened. We therefore predict that stronger heat transport, for instance via ocean floor heat flux heterogeneity (Choblet *et al.*, 2017*a*; Liao *et al.*, 2020), would be required in the polar region to enforce melting at the poles and freezing at the equator.

With the current parameter space, we were limited in analysing the heat transfer scaling behaviour in detail. Global diagnostic scaling of the heat transfer and interior flow speeds indicate that both geometries behave similar and projections to the non-rotating regime for high Ra suggest that both geometries converge to identical heat transfer behaviour as the interior flow convects radially and homogenises the heat transfer to the outer boundary. Thermal and Ekman boundary layer behaviour is an important diagnostic property to characterise heat transfer which we briefly explored in Appendix A.2. In this parameter space, only a fraction of the boundary layer thickness estimations showed a consistent trend that are in good agreement with literature (e.g., Gastine *et al.*, 2016; King *et al.*, 2013, 2012). Interestingly, we demonstrated that dividing the domain into local regions of the pole and equator gives different estimates. This difference could be explained by the variation in convective vigour and preferred direction of rising currents at different latitudes caused by rotation. This divided approach could potentially improve current methods to characterise heat transfer locally in regimes that are influenced by rotation, as opposed to the characterisation of boundary layers averaged across the complete sphere.

The development of the model presented one of the main challenges faced in this study. We developed a numerical tool to simulate rotating thermal convection in a complex domain using a spectral element solver. The spectral element method combines the high-order accuracy of the spectral method that is commonly used in geophysical fluid dynamics models, and the flexibility of the finite element method to handle complex geometries. This is accompanied by low dispersion and dissipation errors, fast convergence properties and efficient domain decomposition relevant for parallel computing. A series of problems were simulated for testing, verification and validation of the code as described in detail in Appendix B. With this work we have demonstrated the capability of our numerical tool to handle traditional geophysical fluid dynamics problems (e.g., rotating Rayleigh-Bénard convection) and to simulate fluid flows in complex geometries that are not possible with the industry-standard spectral method codes. Further development of the code presents exciting novel research with the implementation of heterogeneous heat flux boundary conditions and mechanical forcings that drive fluid flow, in combination with complex shell geometries to approach more geophysically relevant conditions.

3.2. Recommendations

We provided a new approach to simulate geophysical fluid problems where topographical influences are modelled to determine more localised influences on flow and heat transfer behaviour. To build on this endeavour and complement our work on characterising Enceladus' ocean, below we provide recommendations for new directions to be tackled in future work.

- **Extended parameter space with Ra and Ek**

  The model incorporates thickness variations that roughly approximate the Enceladan ocean and is symmetric with respect to the equatorial plane. The range of Rayleigh numbers in this study prevented the exploration of the non-rotating flow regime, causing an incomplete view of the flow structure development from near onset to highly supercritical flows. Similarly, only one Ekman number was studied which prohibits the extrapolation of flow regimes to geophysical values. Further work must be performed that increases the parameter space of both the Rayleigh and Ekman numbers, which demands more computational resources to resolve smaller flow structures associated with increasing Ra and decreasing Ek. A rapidly rotating regime is for instance expected for $Ek < 10^{-4}$, where strongly axialised columnar convection persists with highly efficient heat transfer characteristics (Gastine *et al.*, 2016). Furthermore, near onset the lowest simulated supercritical value of the Rayleigh number is estimated at roughly 1.6 times the critical Rayleigh number (Amit *et al.*, 2020). Future work could analyse the influence of the non-uniform shape(s) on the magnitude of Ra_c and the location of where convection onsets. We found that convection similarly onsets at the tangent cylinder intersection with the equator for the non-uniform model compared to the uniform model (e.g., Dormy *et al.*, 2004). Given that Ra_c in uniform spherical shells is controlled

by the shell thickness (Al-Shamali *et al.*, 2004), we hypothesise that Ra_c for a uniform shell with a thickness equivalent to the equatorial thickness of a non-uniform model is the same for this non-uniform shell. Given the strong polar heat fluxes at Enceladus, it would be interesting to explore the impact of shape and heterogeneous thermal boundary conditions on the location of onset and the associated mode(s) of convective instability (e.g., onset in spheres is characterised by thermal Rossby waves).

- **Exploration of domain perturbation parameters**
  Further work can be focussed on the investigation of differing harmonic domain perturbations (i.e., variations of n and m in C_{nm}), including that of a broken symmetry with respect to the equatorial plane, and the parameter exploration of varying the amplitudes of the shape perturbation (i.e., magnitude of C_{nm}). This could pose improved insights into the impact of shell geometry on flow behaviour and comparability with the moon's predicted shape (Čadek *et al.*, 2019; Hemingway & Mittal, 2019). In a similar framework, Rovira-Navarro *et al.* (2020) studied the tidal response of low degree ocean thickness variations of subsurface oceans and found variations in resonant modes introduced by the non-uniform geometry. Evonuk (2015) explored the influence of equatorial ellipticity (i.e., degree of flattened shape from circular) on the convective flow patterns in a rotating 2D domain, thereby finding shifts in flow regimes caused by degree of ellipticity.

- **More realistic boundary conditions**
  Large amplitude, long wavelength heterogeneous ocean floor boundary heat flux is further anticipated to strongly influence ocean circulation in Enceladus (Choblet *et al.*, 2017*a*). Simulations of thermal convection in spherical shell domains have shown that lateral boundary heat flux heterogeneities can impose strong variations in ocean circulations compared to isothermal boundaries (e.g., Amit *et al.*, 2015; Gibbons *et al.*, 2007; Mound & Davies, 2017; Olson, 2016). Our model could be used as a framework to combine both shell thickness and boundary temperature heterogeneities to assess the individual and combined influence of both parameters on flow structures and heat transfer behaviour. Furthermore, heat is transported towards and away from the ice shell. Stefan-type boundary conditions at this ice-ocean interface can account for water phase changes to improve the dynamic interaction between the ice shell and ocean and model the stability of the ice shell's topography from thermal modifications (e.g., Favier *et al.*, 2019*b*).

- **Collective geophysical force model**
  Time-varying mechanical forces, induced from gravitational interactions, are present in the dynamical system of an icy moon orbiting their host planet alongside their sister satellites. This could greatly influence the internal flow behaviour of the fluid (Lissauer & De Pater, 2013; Reddy *et al.*, 2018; Soderlund *et al.*, 2020). Combining mechanical forces (i.e., precessional, librational and tidal) with rotating thermal convection into one single model could be a compelling direction that is of interest for the study of many geophysical objects. For instance, Vormann & Hansen (2020) combined precessional flow with thermal convection in an ellipsoidal shell container and Reddy *et al.* (2018) combined tidal, librational and precessional mechanical forces to study dynamo action in full ellipsoidal containers.

- **Scaling behaviour of boundary layers**
  In this work we have attempted to analyse boundary layer thicknesses and assess their relation towards theoretical arguments. Despite the limited range where scaling relations are found comparable to previous work, we find that polar and equatorial scaling behave differently for a given Ra, caused by rotation. We apply the traditional method of computing temperature and velocity profiles to the uniform domain, which can conceal or dampen local variations in velocity and temperature distributions and thus affect scaling estimates. To explore whether localised analyses of the boundaries are more appropriate, future work must analyse boundary layer thicknesses in relation to *local* estimates of the Nusselt number and convective Reynolds number. This approach is contrary to our study's global estimates of Nu and Re_c in the uniform domain. It can also further improve comparisons made between rotating plane-layer and spherical shell convection problems.

A

Supplementary materials

The manuscript is supplemented by additional information and results in this study. First, in Appendix A.1 a summary of the diagnostics associated with the resolution of the model(s) is given in the form of a table. Second, due to limited amount of data for a confident scaling analysis, we report on the boundary layer thickness behaviour in reference to theoretical predictions (Appendix A.2). Finally, non-rotating simulations were performed and are briefly described in Appendix A.3.

A.1. Summary of results

A brief summary of all simulations are given below in Table A.1, displaying the important diagnostic quantities associated with domain resolutions. For all simulations, the Prandtl and the Ekman numbers are kept fixed at 1 and 3×10^{-4}, respectively. The definitions of the various diagnostics are described in Section 2.2.5. The mesh resolutions are given by the horizontal N_h and radial N_r element counts and the polynomial order p of the Lagrange type. Thermal and Ekman boundary layer thicknesses and the number of grid points in the boundary layers for the non-uniform domain are given for the equatorial region since this region is generally more developed and is convective throughout the parameter range studied and thus provides a better proxy. Δh is the mean grid width for the respective domain where we assume an isometric distribution of unique grid points throughout the spherical domains (i.e., $\Delta x = \Delta y = \Delta z$).

Case	$N_r \times N_h$	p	$\eta_k/\Delta h$	δ_T^i	δ_T^o	δ_E^i	δ_E^o	N_T^i	N_T^o	N_E^i	N_E^o
S_1	10×864	7	2.05	1.71×10^{-1}	1.27×10^{-1}	2.90×10^{-2}	2.29×10^{-2}	18	16	6	5
S_2	10×864	7	1.33	1.48×10^{-1}	1.01×10^{-1}	2.72×10^{-2}	2.38×10^{-2}	17	13	6	5
S_3	10×864	7	0.95	1.29×10^{-1}	7.81×10^{-2}	2.55×10^{-2}	2.35×10^{-2}	16	11	5	5
S_4	10×864	7	0.71	9.79×10^{-2}	7.92×10^{-2}	2.31×10^{-2}	2.27×10^{-2}	13	12	5	5
S_5	10×864	12	0.99	8.45×10^{-2}	7.82×10^{-2}	1.97×10^{-2}	2.00×10^{-2}	20	19	7	7
S_6	14×3456	7	0.75	6.27×10^{-2}	6.08×10^{-2}	1.79×10^{-2}	1.88×10^{-2}	16	15	8	8
S_7	14×3456	8	0.71	5.08×10^{-2}	4.95×10^{-2}	1.66×10^{-2}	1.77×10^{-2}	14	14	8	9
S_8	14×3456	9	0.66	4.18×10^{-2}	4.13×10^{-2}	1.57×10^{-2}	1.68×10^{-2}	15	15	8	9
P_1	10×864	9	2.32	8.57×10^{-2}	2.36×10^{-1}	2.72×10^{-2}	8.24×10^{-2}	20	33	11	19
P_2	10×864	9	1.68	6.60×10^{-2}	1.24×10^{-1}	2.66×10^{-2}	4.38×10^{-2}	15	23	10	13
P_3	10×864	9	1.22	6.28×10^{-2}	9.46×10^{-2}	2.60×10^{-2}	3.46×10^{-2}	15	21	10	12
P_4	10×864	11	1.12	6.21×10^{-2}	8.64×10^{-2}	2.58×10^{-2}	3.31×10^{-2}	18	24	12	14
P_5	22×4374	8	1.49	5.88×10^{-2}	7.96×10^{-2}	2.47×10^{-2}	2.95×10^{-2}	30	36	20	21
P_6	22×4374	8	1.07	5.56×10^{-2}	6.68×10^{-2}	2.44×10^{-2}	2.83×10^{-2}	30	34	20	21
P_7	22×4374	9	0.99	5.13×10^{-2}	5.90×10^{-2}	2.35×10^{-2}	2.65×10^{-2}	32	34	22	23
P_8	22×4374	10	0.91	4.58×10^{-2}	5.13×10^{-2}	2.20×10^{-2}	2.46×10^{-2}	34	36	23	24

Table A.1: Summary of results related to numerical resolutions employed in the simulations. We characterise results associated with a uniform spherical shell with $C_{20} = 0$ denoted by case numbers S_i, and non-uniform spherical shells with $C_{20} = 0.5$ denoted by case number P_i.

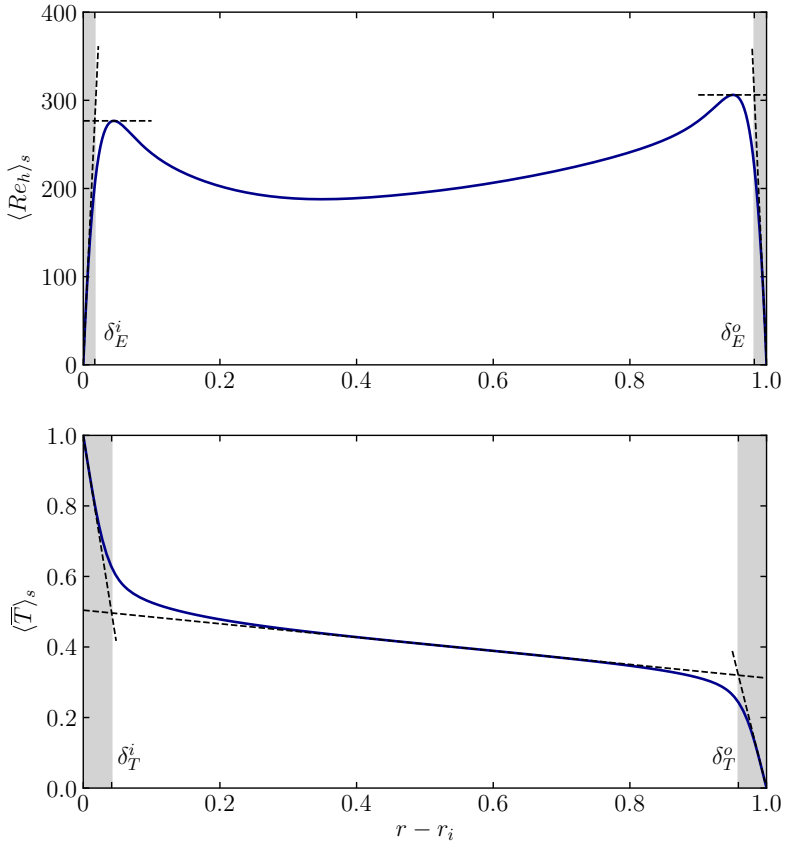

Figure A.1: Ekman (a) and thermal (b) boundary layer estimations using the time and horizontally averaged horizontal velocity, $\langle Re_h \rangle_s$, and temperature, $\langle \overline{T} \rangle_s$, fields. The linear intersection method is demonstrated by the intersection of the dashed lines. Boundary layer thicknesses are indicated with the shaded regions and denoted by δ with indices T or E indicating temperature or Ekman boundary layer type respectively and superscripts i, o indicating the location at inner, outer boundary. The interior profiles were used from the uniform model with $Ra = 5 \times 10^6$.

A.2. Thermal and Ekman boundary layer scaling

A.2.1. Boundary layer estimation technique

The estimation of boundary layer thicknesses is generally performed using the time and horizontally averaged temperature and horizontal velocity fields (e.g., Gastine *et al.*, 2016, 2015; King *et al.*, 2013, 2012; Long *et al.*, 2020). For both boundary layer types (i.e., Ekman and thermal), we employ a linear intersection method that is commonly applied in (rotating) convection studies and is found to follow theoretically predicted scaling laws (e.g., Gastine *et al.*, 2016, 2015; Long *et al.*, 2020) (see Figure A.1). The thermal boundary layer thickness is found by the intersection of the linear fit of the temperature profile at the middle of the shell $r = (r_i + r_o)/2$ and the linear fit at the boundaries. Similarly, the Ekman boundary layer thickness is found by the intersection of the linear fit at the boundary and the nearby maxima of $\langle \overline{Re_h} \rangle_s$ of the respective boundary. We denote the boundary layer thickness by δ, the type by the index with δ_T for thermal and δ_ν for viscous (i.e., non-rotating model) or δ_E for Ekman boundary layers. Note that the viscous boundary layer is similar to the Ekman boundary layer as they both are associated with the viscous dissipation of the fluid velocity. As mentioned in Section 2.2, the non-uniform domain introduces additional horizontal asymmetries in boundary layer thickness estimations. Hence, we separately capture the time and horizontally averaged temperature and horizontal velocity fields for localised regions at the pole and equator.

A.2.2. Thermal boundary layers

For non-rotating convection, heat transfer can be assumed to be transferred through conduction in the thermal boundary layers (King *et al.*, 2012). With sufficient thermal forcing, the interior fluid is vigorously mixed and reaches an isothermal state such that (almost) the entire temperature drop ΔT is

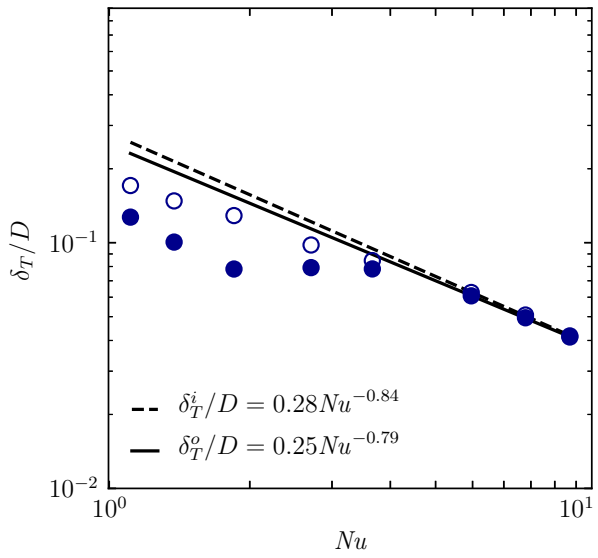

Figure A.2: Thermal boundary layer estimations using the slope intersection technique applied to the temperature profiles as shown in Figure 2.10 for the uniform model. Marker filling highlights the boundary layer thickness at the inner boundary (empty) and outer boundary (filled). The dashed and solid lines denote the scaling estimates of respectively the inner and outer thermal boundary thicknesses.

controlled inside the two thermal boundary layers (e.g., Gastine *et al.*, 2015; King *et al.*, 2012). Given that heat is transferred by conduction in these layers, the Nusselt number can be used to predict the boundary layer thicknesses for a given temperature gradient at the boundaries (Gastine *et al.*, 2015),

$$\frac{\delta_T}{D} \sim Nu^{-1}. \tag{A.1}$$

For rotating convection, the thermal boundary layers are expected to additionally depend on the Ekman and Rayleigh numbers as they strongly influence the temperature profile and consequently the boundary layers thickness estimations (Gastine *et al.*, 2016; King *et al.*, 2012). Figure A.2 shows the thermal boundary layer estimations for the inner (empty symbols) and outer (filled symbols) boundaries for the uniform models and Figure A.3 shows this for the polar (a) and equatorial (b) regions. For low Nu, the outer boundary layer thickness highlights a poor estimation that can be explained by the relatively shallow temperature gradients at the outer boundary compared to the steeper gradients at the inner boundary and thus introduces stronger uncertainties in the estimation process. The inner boundary shows a continuous decreasing trend up to $Nu < 4$, after which both inner and outer boundaries converge to similar thickness trends. Contrary to similar rotating spherical shell convection studies (e.g., Gastine *et al.*, 2016; Long *et al.*, 2020), the inner and outer boundaries do have similar thicknesses as opposed to a larger expected thickness at the outer boundary. This can be explained by the smaller radius ratios (i.e., thicker shells) employed in the aforementioned studies where spherical asymmetries are enhanced, and possibly a relatively low range of Nu where asymmetries may not have been fully developed. Gastine *et al.* (2015) found that these asymmetries, that affect thermal boundary layer thicknesses, diminish with increasing radius ratios as the influence of the domain curvature vanishes in the limit $\chi \to 1$. We fit the inner and outer boundary layer thicknesses for the higher range of $Nu > 4$, yielding the scaling relation for the uniform model

$$\frac{\delta_T^i}{D} = 0.280Nu^{-0.835}, \qquad \frac{\delta_T^o}{D} = 0.251Nu^{-0.793}. \tag{A.2}$$

The slightly shallower slopes of the boundary layer thickness, compared to the non-rotating scaling slope of −1, and the prefactor magnitudes are both in good agreement with similar spherical shell studies (Gastine *et al.*, 2016; Long *et al.*, 2020). The non-uniform scaling is similarly performed on $Nu > 4$, yielding the polar scaling relations

$$\frac{\delta_T^i}{D} = 0.973Nu^{-1.659}, \qquad \frac{\delta_T^o}{D} = 0.257Nu^{-1.103}. \tag{A.3}$$

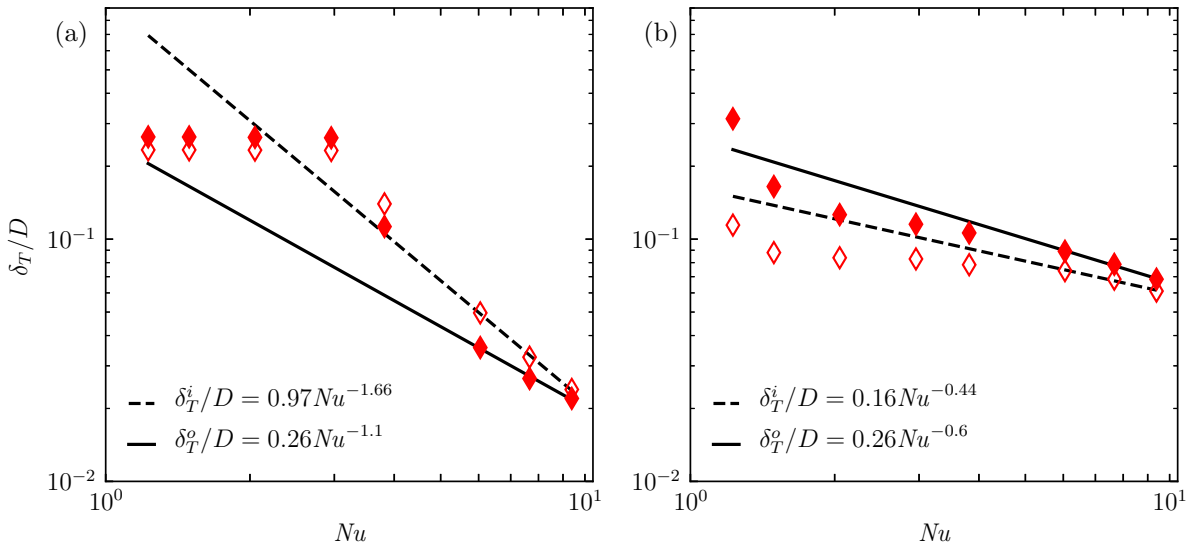

Figure A.3: Thermal boundary layer estimations using the slope intersection technique applied to the temperature profiles as shown in Figure 2.12 for non-uniform model in the polar (a) and equatorial (b) regions. Marker filling highlights the boundary layer thickness at the inner boundary (empty) and outer boundary (filled). The dashed and solid lines denote the scaling estimates of respectively the inner and outer thermal boundary thicknesses.

and the equator scaling relations,

$$\frac{\delta_T^i}{D} = 0.164Nu^{-0.439}, \qquad \frac{\delta_T^o}{D} = 0.265Nu^{-0.602}. \tag{A.4}$$

In the non-uniform domain, thermal boundary layers in the polar region scale much steeper than anticipated, as opposed to a shallower scaling behaviour at the equator. In a plane-layer study where the rotation axis is aligned with the gravity vector, analogous to the polar region, King *et al.* (2013) found a good agreement with the predicted scaling in the same range of Ra and Ek. This could suggest that rotationally aligned convection in the polar region scales better with the predicted scaling. Nevertheless, the range of applicable boundary thickness measurements is limited and further increase of Ra is needed to find a confident trend to assess this hypothesis.

A.2.3. Viscous boundary layers

To find the Ekman boundary layer, we analyse the time and horizontally averaged horizontal velocity profile $\langle \overline{Re}_h \rangle_s$ where we apply the linear intersection technique. Figure A.1 shows a typical horizontal velocity profile that demonstrates the no-slip boundary conditions visualised by the diminishing velocity at both inner and outer boundaries. Close to the boundaries, strong velocity gradients exist that describe the Ekman boundary layers in the rotating convection problem. Some small radial distance from the boundaries, a peak value of horizontal velocity is found which bounds the bulk fluid that has a lower mean horizontal velocity profile. Naturally, with larger thermal forcing the fluid convects more vigorously, resulting in higher overall velocities and stronger gradients at the boundaries. With no-slip mechanical boundary conditions, the viscous boundary layers are expected to assume a laminar profile and are of Prandtl-Blasius type (e.g., Stevens *et al.*, 2010). In a non-rotating convection problem, the viscous boundary layer can be approximated by the first order force balance between the inertia of the bulk fluid and the viscous effects found in the viscous boundary layer. Applying this assumption in the momentum equation, yields

$$\boldsymbol{u} \cdot \nabla \boldsymbol{u} \sim \nu \nabla^2 \boldsymbol{u}, \tag{A.5}$$

$$\frac{U_c^2}{D} \sim \frac{\nu U_c}{\delta_\nu^2}, \tag{A.6}$$

$$\frac{\delta_\nu}{D} \sim Re_c^{-1/2}, \tag{A.7}$$

where we non-dimensionalise the velocity by the characteristic convective velocity U_c, the fluid bulk length scale by shell thickness D, and the viscous boundary layer length scale by its thickness δ_ν. With the addition of rotation in the problem, the force balance in the Ekman boundary layer can be described by the Coriolis force and viscous effects in the boundary layer, yielding

$$2\boldsymbol{\Omega} \times \boldsymbol{u} \sim \nu \nabla^2 \boldsymbol{u}, \tag{A.8}$$

$$2U\Omega \sim \frac{\nu U}{\delta_E^2}, \tag{A.9}$$

$$\frac{\delta_E}{D} \sim Ek^{1/2}. \tag{A.10}$$

However, since all simulations are run with one value of the Ekman number, $Ek = 3 \times 10^{-4}$, this scaling cannot be tested in the present study. Figure A.4 shows the Ekman boundary layer estimations for the uniform model and Figure A.5 shows this for the non-uniform model in the polar (a) and equatorial (b) regions. We again use similar formatting where we consider inner (empty symbols) and outer (filled symbols) boundary estimations separately. Similar to the thermal boundary layer estimations, the weak velocity gradients at the boundaries for low Re_c are not suitable for accurate boundary layer thickness estimations, which is demonstrated by the initial increasing trend of outer boundary layer thickness up to $Re_c < 10^2$. Upon further increase of Re_c, the outer boundary layer thickness becomes larger than the inner boundary and both inner and outer boundary thicknesses decrease with a roughly constant slope. The polar region in the non-uniform domain shows a shallow decreasing trend when convection onsets in this region. In reference to the shallow initial scaling of the interior boundary in the uniform model, the similar shallow polar scaling suggests that convection is similarly not well-developed. A steeper slope is found at the equator where thermal convection is more developed compared to the poles and approaches the scaling of the uniform model. Linear fits were made on the higher range $Re_c \geq 130$, yielding the scaling relations for the uniform model

$$\frac{\delta_E^i}{D} = 0.048 Re_c^{-0.196}, \qquad \frac{\delta_E^o}{D} = 0.044 Re_c^{-0.167}, \tag{A.11}$$

and non-uniform models at the pole

$$\frac{\delta_E^i}{D} = 0.019 Re_c^{-0.128}, \qquad \frac{\delta_E^o}{D} = 0.020 Re_c^{-0.134}, \tag{A.12}$$

and at the equator

$$\frac{\delta_E^i}{D} = 0.073 Re_c^{-0.157}, \qquad \frac{\delta_E^o}{D} = 0.113 Re_c^{-0.215}. \tag{A.13}$$

Notably, the shallow slopes of these scaling relations do not agree with the $-1/2$ slope expected for non-rotating scaling prediction. Similar to other scaling studies (Gastine *et al.*, 2016; Long *et al.*, 2020), the boundary layer thickness does not seem to depend on Re_c, but these studies do however find good agreement with a dependence on $Ek^{1/2}$ where the fluid is controlled by the Coriolis force balance with the fluid bulk inertia. Given this study's similar scaling behaviour of the Ekman boundary thickness on Re_c with other work, our model is potentially similarly strongly influenced by Coriolis, where the viscous effects in the boundary layer are balanced by the Coriolis force in the bulk fluid. Nevertheless, future work is needed to study the scaling with Ek on Ekman layer thicknesses.

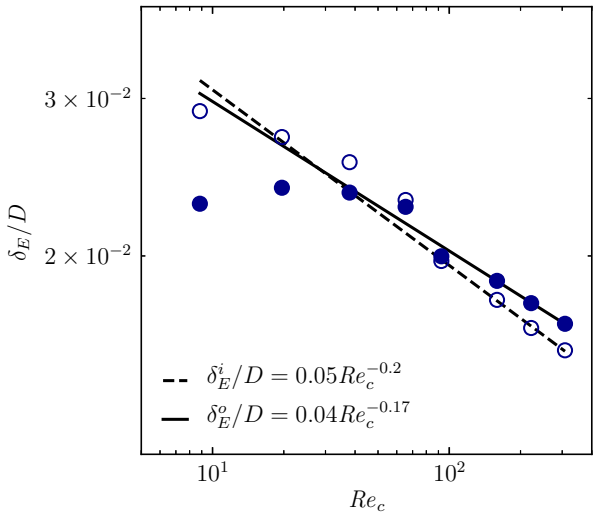

Figure A.4: Ekman boundary layer estimations using the slope intersection technique applied to the horizontal velocity profiles for uniform model. Symbol filling highlights the boundary layer thickness at the inner boundary (empty) and outer boundary (filled). The dashed and solid lines denote the scaling estimates of respectively the inner and outer thermal boundary thicknesses.

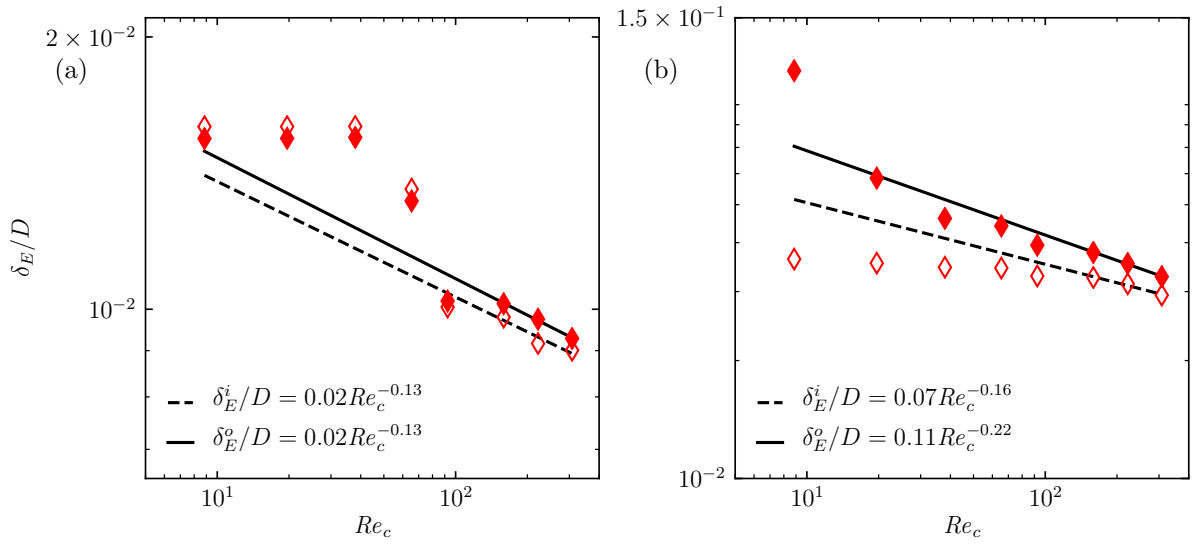

Figure A.5: Ekman boundary layer estimations using the slope intersection technique applied to the horizontal velocity profiles for non-uniform model in the polar (a) and equatorial (b) regions. Symbol filling highlights the boundary layer thickness at the inner boundary (empty) and outer boundary (filled). The dashed and solid lines denote the scaling estimates of respectively the inner and outer thermal boundary thicknesses

A.3. Supplementary non-rotating simulations

To estimate the behaviour of the non-rotating regime in the rotating model, we simulated a non-rotating model for a range of Rayleigh numbers. Here, the Boussinesq equations are non-dimensionalised using $D = r_o - r_i$ for length scale, ΔT for temperature scale, viscous dissipation time D^2/ν as time scale, leading to ν/D as velocity scale and $\rho_o \nu^2/D^2$ as pressure scale. The non-dimensional Boussinesq equations are then given by

$$\nabla \cdot \boldsymbol{u} = 0, \tag{A.14}$$

$$\frac{\partial \boldsymbol{u}}{\partial t} + \boldsymbol{u} \cdot \nabla \boldsymbol{u} = -\nabla P + \nabla^2 \boldsymbol{u} + \frac{Ra}{Pr} \frac{\boldsymbol{r}}{r_o} T, \tag{A.15}$$

$$\frac{\partial T}{\partial t} + \boldsymbol{u} \cdot \nabla T = \frac{1}{Pr} \nabla^2 T. \tag{A.16}$$

We simulated 5 cases for $\chi = 0.8$ for Rayleigh numbers ranging between $6.0 \times 10^4 \leq Ra \leq 3.0 \times 10^6$ and recorded the Nusselt number, given by equation 2.11, and the Reynolds number given by,

$$Re = \frac{\hat{U} D}{\nu} = U^{rms}, \tag{A.17}$$

where we again use the rms velocity, U^{rms}, as the characteristic velocity (see section 2.2). The results are summarised in Table A.2 and shown in Figure A.6 below. We find a $Nu - Ra$ scaling relation,

$$Nu = 0.1639 Ra^{0.2801}. \tag{A.18}$$

This relation agrees well with the predicted 2/7 scaling behaviour found theoretically (Shraiman & Siggia, 1990) and experimentally in the same range of Ra (Castaing *et al.*, 1989; Cheng *et al.*, 2015), including spherical shell domains (Gastine *et al.*, 2015).

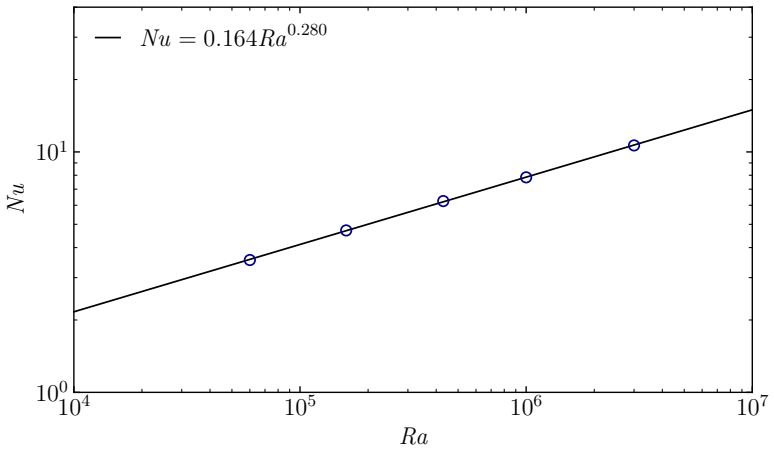

Figure A.6: Nusselt versus Rayleigh number in a non-rotating uniform spherical shell model with $\chi = 0.8$. Symbols denote the results from simulations as given in Table A.2 and the solid black line denotes the estimated least-square fit.

Ra	Nu	Re	$N_r \times N_h$	p
6.0×10^4	3.55	48.5	10×864	7
1.6×10^5	4.72	81.5	10×864	7
4.3×10^5	6.24	135.3	10×864	7
1.0×10^6	7.84	205.5	10×864	12
3.0×10^6	10.64	353.3	14×3456	8

Table A.2: Brief summary of non-rotating simulation results for a uniform model with radius ratio of $\chi = 0.8$.

B

Numerical tools

In this appendix, we give a description of the important steps taken to understand, develop and test the numerical code that solves the spherical shell convection problem. Section B.1 provides an overview of the numerical method selected to simulate this problem. We further elaborate on the chosen code and its numerical methods. Before we model thermal convection in a rotating spherical shell, a series of problems were formulated to learn how to manipulate the numerical code to simulate fluid phenomena (Section B.2). We then describe the development, initiation and testing of thermal convection in a spherical shell domain in Section B.3.

In the learning stages of using Nek5000, the code was exclusively run on a personal computer with 4 cores using MPI (Intel quad-core i7-6700HQ processor). Progressively, the numerical problems increased in dimension, as well as in numerical resolutions, requiring significantly more computational resources. Simulations of the three-dimensional Taylor-Green vortex problem, and the spherical shell models were primarily performed on the university high performance cluster (HPC12) from the Aerodynamics, Wind Energy, Flight Performance and Propulsion (AWEP) department. Data processing was performed with Nek5000 and Python and visualisations were made primarily using the Python MatPlotLib library and Paraview (https://www.paraview.org/). Further, as will be explained later in Section B.1.3, numerical integration of the solutions is obtained using Gaussian quadrature. For this Maple, a math software application, is employed to find quadrature weights from the first derivative of Legendre polynomials.

B.1. Numerical method

To simulate rotating convection in a non-uniform shell, a numerical method must be selected that is able to solve the system of fluid dynamical equations in a complex domain (see Section 1.1.1). We have chosen to solve the governing equations using the Spectral Element Method (SEM). This method is a companion/implementation of the Finite Element Method (FEM), where the unknowns are expressed at discrete, non-uniformly spaced spectral nodes and high-order polynomial basis functions. The SEM combines the high-order accuracy of the Spectral Method (SM) and handling of complex geometries of the FEM. Further, the high-order accuracy in SEM provides low dispersion and dissipation errors, rapid convergence properties and allows for efficient domain decomposition in parallel computing (Karniadakis & Sherwin, 1999).

B.1.1. Basic concepts of the spectral element method

For brevity, we assume a solution value in the form $u = u(\boldsymbol{x}, t)$ and the governing equation defined in domain Γ to be given in the form

$$\mathcal{L}(u) = f \qquad \text{in} \qquad \Gamma, \tag{B.1}$$

where $\mathcal{L}$ denotes an operator on variable u (e.g., $\nabla^2(\dots)$) and f is an arbitrary function. The above form describes the *strong* form of the governing equation, meaning that the solution is satisfied at every nodal point in the domain. To find an approximate solution $\hat{u}$, the method of weighted residuals is

employed where a finite set of N basis functions $\phi(\boldsymbol{x})$ is introduced

$$u \approx \hat{u} = \sum_{j=0}^{N} a_j \phi_j, \tag{B.2}$$

where a_j are the unknown expansion coefficient and ϕ_j constitutes a set of orthogonal basis functions. There are two types of functions used to 1) approximate the solution and 2) to verify its approximation. Trial functions ϕ_j are basis functions that describe the solution of the governing equation(s). Test or weighting functions w, on the other hand, are the functions that test whether the combination of trial functions indeed closely approximates and therefore satisfies the differential equation(s) and imposed boundary conditions. Nek5000 uses the Galerkin method where the weighting functions are the same as the choice of basis functions. All basis functions are required to satisfy the boundary conditions and the residual must be orthogonal to the weight functions. As $\hat{u}$ will not be exactly equal to u, a residual is defined when inserting $\hat{u}$ into the governing equation

$$\mathcal{R} \equiv \mathcal{L}(\hat{u}) - f. \tag{B.3}$$

The objective of the numerical method is then to minimise the residual $\mathcal{R}$ for domain Γ whilst satisfying the imposed boundary conditions. The method of weighted residual enforces that the projection of the residual, in domain Γ, on the set of weight functions is equal to zero

$$\int_{\Gamma} \left[\mathcal{L}(\hat{u}) - f \right] w \, d\Gamma = 0. \tag{B.4}$$

The above form is known as the *weak form* of the governing equation, which is also commonly referred to as the *variational form*. Equivalently, the discretised variational form is found by substituting B.2 and $w = \phi$ in B.4

$$\sum_{j=0}^{N} a_j \int_{\Gamma} \left[\hat{\mathcal{L}}(\phi_j) \right] \phi_i \, d\Gamma = \int_{\Gamma} f \phi_i \, d\Gamma, \quad i = 0, \ldots, N. \tag{B.5}$$

The weak form is satisfied and applied at discrete points in finite subspaces for which we can use a discrete differential operator $\hat{\mathcal{L}}$. That is, a differential of ϕ can be expressed by a discrete difference equation.

B.1.2. Nek5000: A spectral element solver

We have selected the SEM code Nek5000 (https://nek5000.mcs.anl.gov/) to solve the incompressible Navier-Stokes equations in a complex domain. Nek5000's spectral element method implementation formulates the variables in the weak form, using the method of weighted residuals and the Galerkin method, with Lagrange interpolation polynomials as basis functions. These polynomials are discretised on a Gauss-Lobatto-Legendre grid for individual elements. A semi-implicit time integration method is used, where the viscous and linear terms are solved implicitly and the convective (non-linear) term explicitly. The k-order Backward Difference Formula (BDF_k) and Extrapolation scheme (EXT_k) are then the respective implicit and explicit methods employed. Nek5000 currently accepts second or third order accurate time integration schemes, $k = 2$ or 3. The interested reader is referred to Deville *et al.* (2002) for a broader coverage on the numerical methods used in Nek5000.

B.1.3. Gaussian quadrature

To discretise and solve the integral (variational) form of the weighted-residual formulation, Nek5000 employs the Gauss-Legendre quadrature rule

$$\int_{-1}^{1} \phi(\boldsymbol{x}) dx = \sum_{j=0}^{N} b_j \phi(x_j), \tag{B.6}$$

where the approximate solution is found at discrete points x_j for the trial function ϕ with weights b_j. Nek5000 uses the Lagrange interpolation polynomials for $\phi(x)$. The quadrature points of the interpolation Lagrange polynomial are determined by the Gauss-Lobatto-Legendre (GLL) points, which are found using Legendre polynomials L_N of degree N. The GLL points, x_j, are given by the roots of the derivative of L_N

$$x_j \equiv L'_N(x) = 0 \quad j = 1, \ldots N - 1, \tag{B.7}$$

including the end points $x_0 = -1$ and $x_N = 1$. Further, the associated weights b_j are given by (Canuto *et al.*, 2007)

$$b_j = \frac{2}{N(N+1)} \frac{1}{\left[L_N(x_j)\right]^2} \quad j = 0, \ldots, N. \tag{B.8}$$

To clarify the practical implementation in Nek5000, a fluid domain Γ is subdivided into a finite number of N subdomain elements Γ^e. These elements are non-overlapping, and, because of the GLL nodal point distribution, the solution values at the element boundaries are equal for neighbouring elements, therefore satisfying the C^0 continuity. In three dimensions, a variable $u(\boldsymbol{x})$ is then locally described in Γ^e by

$$u(\boldsymbol{x})|_{\Gamma^e} = u(x, y, z)|_{\Gamma^e} = \sum_{i=0}^{N} \sum_{j=0}^{N} \sum_{k=0}^{N} a^e_{ijk} h_i(r) h_j(s) h_k(t), \tag{B.9}$$

with the expansion coefficients a_{ijk}, the Lagrange interpolation basis functions h_{ijk} of order N, and the affine transformation coordinates (r, s, t) in $\hat{\Gamma} = [-1, 1]^3$ for $(N+1)^3$ nodal points. Hence, the coordinates in Γ^e in Cartesian space are linearly projected onto a grid with the underlying GLL spacing upon which the expansion coefficients are solved.

B.2. Benchmarking canonical fluid flows

The aim of this thesis is to study rotating convection in a complex geometry, characteristic to the subsurface ocean of Enceladus. In order to accomplish this, a set of tools was developed using Nek5000 where the development followed a stepwise strategy. The problem was divided into separate sub-problems, which in turn were benchmarked and tested. First, the buoyancy force was introduced with the traditional Rayleigh-Bénard convection problem in a two-dimensional domain (Section B.2.1). The code's numerical behaviour is tested with the analytical solution to the two-dimensional Taylor-Green vortex problem in Section B.2.2. Further, the Coriolis forcing introduced by implementing a rotating frame of reference, was benchmarked using the three-dimensional Taylor-Green vortex problem (Section B.2.3). Finally, the benchmarked elements culminated to benchmarking rotating convection in a spherical shell with the numerical results of Amit *et al.* (2020) in Section B.3.

B.2.1. Rayleigh-Bénard convection in 2D

Rayleigh-Bénard convection describes the canonical problem of a fluid situated between two plates with a sufficient unstable temperature difference to initiate convection. The fluid is heated from below and cooled at the top, creating an unstable system that onsets convection once the fluid's Rayleigh number equals (or exceeds) the critical Rayleigh number Ra_c, estimated on the order of $\mathcal{O}(10^3)$ (Chandrasekhar, 1961). This system is described by the Boussinesq approximation as described in Section 1.1.2. The Boussinesq equations are non-dimensionalised with box height D as length scale, the thermal diffusion time D^2/κ as time scale, temperature difference ΔT between the two plates as temperature scale and $\rho_o \kappa^2 / D^2$ as the pressure scale

$$\frac{\partial \boldsymbol{u}}{\partial t} + \boldsymbol{u} \cdot \nabla \boldsymbol{u} = -\nabla P + Ra\, Pr\, T\, \hat{\boldsymbol{e}}_y - Pr\, \nabla^2 \boldsymbol{u}, \tag{B.10}$$

$$\nabla \cdot \boldsymbol{u} = 0, \tag{B.11}$$

$$\frac{\partial T}{\partial t} + \boldsymbol{u} \cdot \nabla T = \nabla^2 T, \tag{B.12}$$

where $\hat{\boldsymbol{e}}_y$ is the unit vector in the vertical direction. The fluid is now described by the non-dimensional Rayleigh, $Ra = \alpha g_o \Delta T D^3 / \nu\kappa$, and Prandtl, $Pr = \nu/\kappa$, numbers. These equations are solved in the domain $0 \leq x, y \leq 1$, where the bottom and top boundaries are isothermal, impenetrable, and have no-slip conditions (see Figure B.1). We impose an adverse temperature gradient of $\Delta T = T_{bottom} - T_{top} = 1$, and the vertical boundaries are periodic. To promote thermal convection, the Rayleigh number was set larger than the critical Rayleigh number. The Prandtl number is set to 1. We tested the implementation of the Boussinesq approximation in Nek5000 by comparing the results with a different code, Diablo (DNS In A Box Laptop Optimized) (https://github.com/johnryantaylor/DIABLO). We refer to the Fortran version of Diablo, as the Matlab version was privately distributed by its author. Diablo is a light model

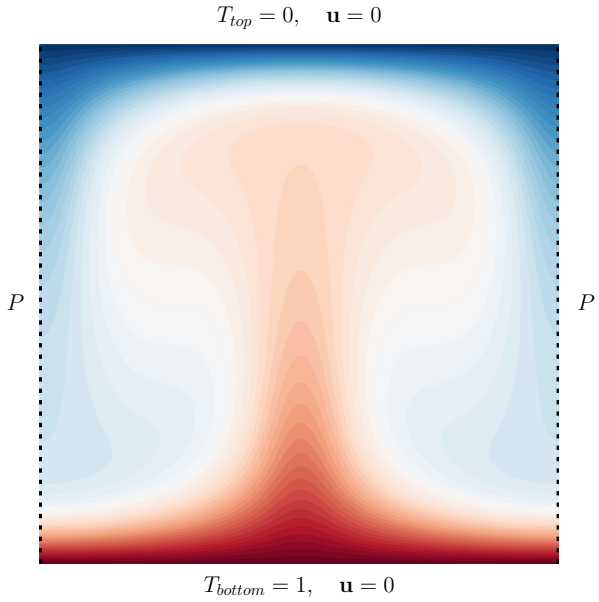

Figure B.1: Temperature field and domain definition of Rayleigh-Bénard convection in a 2D periodic domain from an example temperature field with $Ra = 5 \times 10^4$. A schematic is provided to denote the temperature and velocity boundary conditions, and the periodic P boundaries at the vertical sides of the domain.

that solves the incompressible Navier-Stokes equations on a regular grid with a second order accurate finite difference method. We solve the problem in Nek5000 using 400 elements at polynomial order 7, and in Diablo for 160×160 nodes in each direction to have comparable spatial degrees of freedom for both models. All other input parameters were kept identical in Diablo and Nek5000. The timestep was set variable for both models, with a stability constraint set using Courant-Friedrich-Lewy number of 0.4. Further, the fluid was initialised without motion and with an unstable linear temperature field. To initialise convection, a random perturbation was added.

An important parameter in the Rayleigh-Bénard convection problem is the Nusselt number, which describes the ratio of heat transfer at a surface from convective sources (i.e., convection and conduction), to that of conduction sources alone

$$Nu = \frac{qD}{\kappa \rho_o c_p \Delta T} = \frac{d\overline{T}/dy}{dT_c/dy}, \tag{B.13}$$

where q is the integrated heat flux at the surface boundary, c_p the specific heat capacity of the fluid, and T_c the conductive temperature field. Here $\overline{T}$ denotes the time-averaged temperature field. For the simple box geometry, the conductive temperature field is the solution of

$$\frac{d^2T(y)}{dy^2} = 0, \quad T_{bottom} = 1, \quad T_{top} = 0, \tag{B.14}$$

resulting in,

$$T(y) = 1 - y. \tag{B.15}$$

Three cases of varying degree of thermal forcing are considered with $Ra = 10^4, 5 \times 10^4, 10^5$. The Nusselt number is computed to compare the heat flux at the top boundary of the domain for both models. Results are summarised in Figure B.2. Both Nek5000 and Diablo demonstrate similar heat transfer behaviour for the cases studied. Nek5000 shows a delay in onset compared to Diablo, which is especially noticeable for the least convective case (i.e., $Ra = 10^4$). The magnitude of the Nusselt number increases as the thermal forcing is increased. For increasing Rayleigh numbers, the initial overshoot in Nusselt number increases, followed by increased number of oscillations until a state of equilibrium is reached. A slight difference is found in the Nusselt number at the respective simulation end-times with less than 0.12% absolute difference, possibly caused by solutions that are not fully converged, a small difference in model accuracy and/or the difference in numerical methods used in both codes.

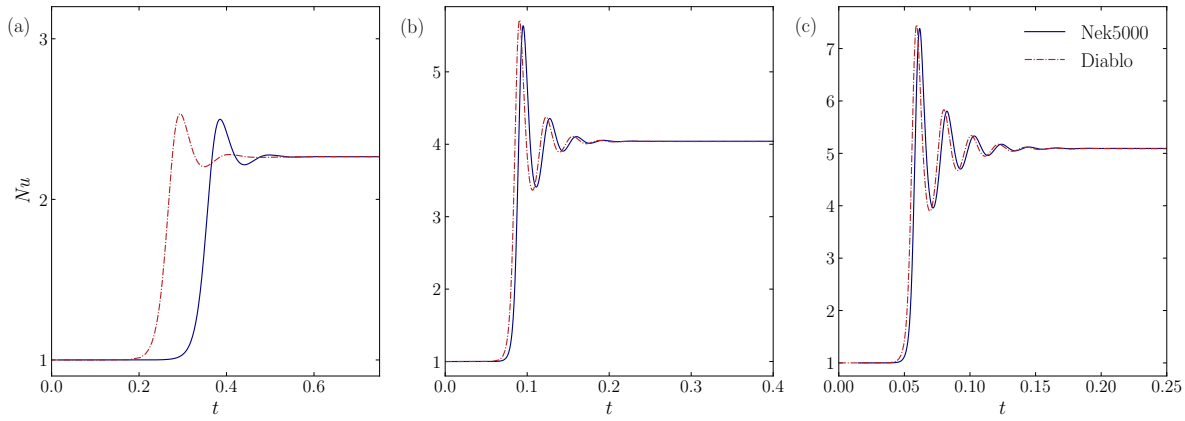

Figure B.2: Nusselt number evolution in Rayleigh-Bénard convection of a Boussinesq fluid for a) $Ra = 100$, b) $Ra = 1000$ and c) $Ra = 10000$. Line styles and colours used for all three figures are shown in the legend of (c).

B.2.2. Taylor-Green vortex in 2D: Convergence analysis

The two-dimensional Taylor-Green vortex problem is one of the few models that has an analytical solution (Canuto *et al.*, 2007), making it a suitable problem for analysing the numerical performance of the SEM code. The main purpose of this analysis is the verification of the code's accuracy of its implemented numerical methods. That is, the order of accuracy of the time integration schemes and the behaviour in accuracy with varying polynomial order p and element count N.

In this particular problem, an incompressible isothermal fluid decays with an exponential rate over time. The fluid equations that will be solved are the dimensional incompressible continuity and momentum equations

$$\nabla \cdot \boldsymbol{u} = 0, \tag{B.16}$$

$$\frac{\partial \boldsymbol{u}}{\partial t} + \boldsymbol{u} \cdot \nabla \boldsymbol{u} = -\frac{1}{\rho} \nabla P + \nu \nabla^2 \boldsymbol{u}, \tag{B.17}$$

where ν is the kinematic viscosity and ρ the fluid density. The Taylor-Green vortex flow field is composed of rotating flows (vortices) in a doubly periodic domain $\Gamma : 0 \leq x, y \leq 1$ with the solution given by

$$\begin{aligned} u(\boldsymbol{x}, t) &= -e^{-8\pi^2 \nu t} \cos(2\pi x) \sin(2\pi y), \\ v(\boldsymbol{x}, t) &= e^{-8\pi^2 \nu t} \sin(2\pi x) \cos(2\pi y), \\ P(\boldsymbol{x}, t) &= -\frac{e^{-8\pi\nu t}}{4} (\cos(4\pi x) + \cos(4\pi y)). \end{aligned} \tag{B.18}$$

The initial conditions in the simulation are found by setting $t_0 = 0$, which has the solution shown in Figure B.3. The box-average kinetic energy is recorded to analyse the code's performance, which is numerical computed using the velocity field in domain Γ

$$\mathcal{E}_k^n(t) = \frac{1}{\Gamma} \int_\Gamma \frac{\boldsymbol{u}(t) \cdot \boldsymbol{u}(t)}{2} \, d\Gamma. \tag{B.19}$$

One finds the analytical expression for the kinetic energy from substituting the velocity components from Equation B.18 into the equation above, yielding

$$\mathcal{E}_k^a(t) = \frac{e^{-16\nu t}}{4}. \tag{B.20}$$

Furthermore, we find the error estimate from the absolute difference between the analytical and numerical solution, given by

$$\text{Error } \mathcal{E}_k = |\mathcal{E}_k^a - \mathcal{E}_k^n|, \tag{B.21}$$

where the analytical and numerical solutions are indicated by indices a and n respectively. The suite of simulations are performed by first defining a baseline model upon which the polynomial order, element

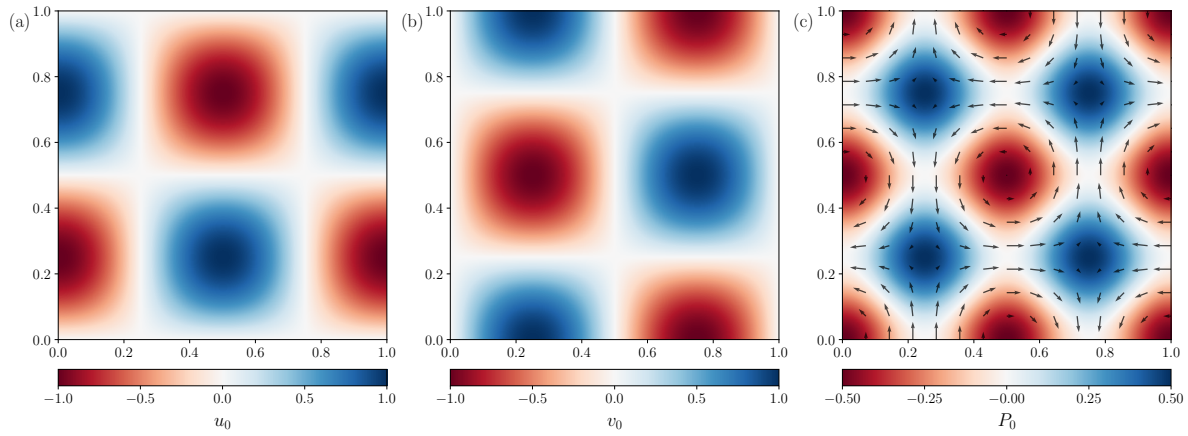

Figure B.3: Taylor-Green vortex problem in doubly periodic space $\Gamma = \{0 \leq x, y \leq 1\}$ visualised for velocity fields (a) u, (b) v and (c) pressure field P at $t = 0$.

count or time integration method is changed. This baseline is defined by a fixed timestep of 10^{-5}, simulation time of 2 time units, 16 elements with polynomial order 4, density $\rho = 1$ and kinematic viscosity $\nu = 10^{-1}$. All baseline simulations are integrated in time with a second order accurate integration scheme. For grid resolution analyses, the element count is increased quadratically, $\{N = i^2 \quad | \quad i = 4, 5, \ldots, 16\}$. For the temporal discretisation analysis, the timestep size is varied with constant logarithmic spacing $\{\Delta t = 10^{-i} \quad | \quad i = 1.0, 1.1, \ldots, 3.0\}$. Figure B.4 shows the results of the convergence analysis for spatial and temporal discretisations.

The time-integration accuracy of the second order method shows a clear second order accurate exponential trend as denoted by the dotted line. Contrarily, the third order accurate scheme initially shows a trend that is even steeper than a third-order exponential trend, followed by a trend that more closely follows a second order trend rather than a third order trend. Further, the third order accurate curve overshoots the absolute error of $\mathcal{O}(10^{-4})$, after which the curve finally follows the same constant error estimate of the second order model. This saturation at 10^{-4} is not indicative of round-off errors as it shows no erratic behaviour in the curve. Rather, it is indicative of a discretisation error, introduced by numerically approximating the governing equations, or an iteration error introduced by the iterative process of converging to a solution for these equations (Tu *et al.*, 2018). The former could be attributed to insufficient resolution of the domain such that further decrements in time step size no longer decreases the order of the error as it is controlled by the spatial resolution. That is, up to $\Delta t \gtrsim 10^{-3}$ the error from spatial resolution is insignificant compared to the larger error from the relatively large time step size. Alternatively, the saturation of the numerical error can be attributed to insufficient solver tolerance for the iterative process of finding a solution in the numerical code. The numerical code solves for the unknowns in an iterative fashion and stops with this process once the unknowns are converged to values within a certain *tolerance*. If this process is stopped prematurely, the solution is not fully converged and errors are introduced.

The spatial convergence behaviour in Figure B.4 (b) shows increasingly smaller errors when increasing the number of elements and also increasing the polynomial order. As one increases either the element count or the polynomial order, the number of spatial degrees of freedom or numerical resolution increases accordingly. This hence increases the numerical accuracy. As expected for a spectral element method, increasing the number of elements has a roughly constant exponential curve associated with it. This constant exponent is steepened (i.e., more negative) when the polynomial order is increased. For polynomial order 5, the numerical error seems to converge to $\mathcal{O}(10^{-7})$ after $N = 10^2$. Both lower polynomial cases have not reached their respective converged solutions.

Figure B.4 (c) demonstrates this impact of increasing the polynomial order more clearly, where the slope of kinetic energy error estimate decreases up to $p \sim 7$. This latter shows that the numerical error exponentially decreases with increasing polynomial order p. It is noted that the error estimates are taken at the final timestep at $t \approx 2$, which is not equal for all simulation as not all timesteps are integer multiples of $t = 2$. This may hence create uncertainties in the error estimate, especially when Δt is large.

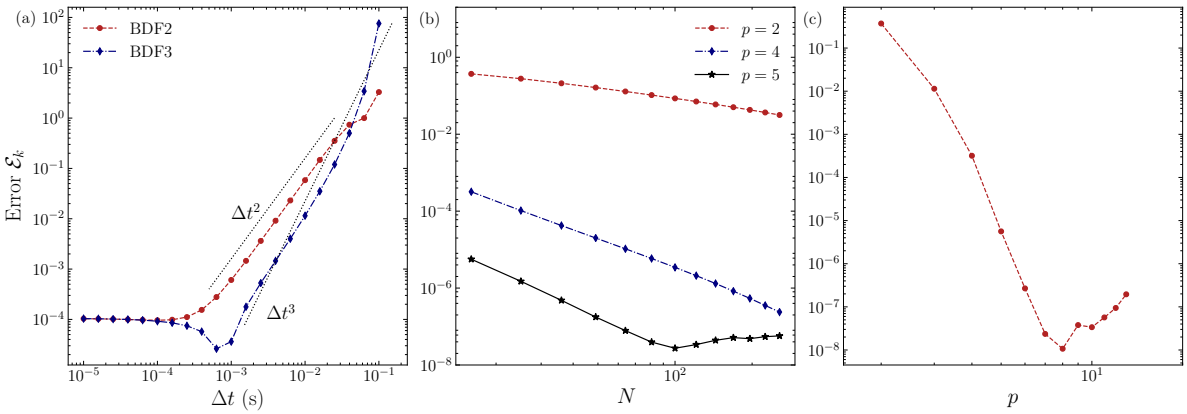

Figure B.4: Absolute error of Kinetic Energy as per Equation B.21 for varying order of timestepping integration schemes (a), number of total elements N (b) and polynomial order p (c). All error estimates were made at the final timestep of the simulation at $t = 2$. BDF2 and BDF3 are the second and third order accurate Backward Difference Formulas used for timestepping.

B.2.3. Taylor-Green vortex in 3D: Validation with rotation

In this third and final benchmark, the Taylor-Green vortex is analysed in three-dimensional space. In particular, the domain is rotating to verify the implementation of Coriolis force in the body-force term of the momentum equation. This problem does not have an analytical solution in its three-dimensional form and shall be compared using solutions from an established code. That is, the solutions will be compared to the results of the same problem with the pseudo-spectral code as used in Pestana & Hickel (2019, 2020). We non-dimensionalise the governing incompressible, isothermal continuity and Navier-Stokes equations in a rotating frame using L as length scale, V_o as velocity scale, L/V_o as time scale and ρV_o^2 as pressure scale, yielding

$$\nabla \cdot \boldsymbol{u} = 0, \tag{B.22}$$

$$\frac{\partial \boldsymbol{u}}{\partial t} + \boldsymbol{u} \cdot \nabla \boldsymbol{u} + \frac{1}{Ro}\,\hat{\boldsymbol{e}}_z \times \boldsymbol{u} = -\nabla \Pi + \frac{1}{Re}\nabla^2 \boldsymbol{u}, \tag{B.23}$$

where Π is the reduced pressure absorbing the centrifugal force, $Re = V_o L/\mu$ is the Reynolds number with μ the dynamic viscosity and $Ro = V_o/(2L\Omega)$ is the Rossby number with Ω the rotational acceleration. The initial conditions of the velocity field are given by

$$\begin{aligned} u &= 0 \\ v &= -V_o \cos\left(\frac{x}{L}\right) \sin\left(\frac{y}{L}\right) \cos\left(\frac{z}{L}\right), \\ w &= V_o \cos\left(\frac{x}{L}\right) \cos\left(\frac{y}{L}\right) \sin\left(\frac{z}{L}\right), \end{aligned} \tag{B.24}$$

where $V_o = L = \rho_o = 1$ in the periodic domain $\Gamma : -\pi \leq x, y, z \leq \pi$. The simulation is run with Reynolds number, $Re = 100$ and was integrated in time from $t_0 = 0$ to $t = 20$. The fluid domain is decomposed into a mesh of 32 elements in every direction for polynomial order $p = 7$ (i.e., 6 Gauss-Lobatto nodes in each direction). The spatial resolution is 192^3 nodes, sharing an identical number of spatial degrees of freedom with the benchmark simulations. As the influence of Coriolis forcing is analysed, three cases are considered: 1. No rotation, 2. slow rotation of $Ro = 1$ and, 3. rapid rotation of $Ro = 0.1$. To quantify the behaviour of the fluid, the kinetic energy density defined in Equation B.19 is computed, as well as the dissipation rate thereof, which is given by

$$\epsilon = -\frac{d\mathcal{E}_k}{dt}. \tag{B.25}$$

This dissipation rate is associated with the enstrophy of the fluid, which is given by the integral of the vorticity squared (Canuto *et al.*, 2007)

$$\zeta = \frac{1}{\Gamma}\int_\Gamma \boldsymbol{\omega} \cdot \boldsymbol{\omega}\, d\Gamma, \tag{B.26}$$

where $\boldsymbol{\omega} = \nabla \times \boldsymbol{u}$ is the vorticity. Then, the dissipation rate of kinetic energy is found by multiplying the enstrophy with the viscosity

$$\epsilon = \nu\zeta. \tag{B.27}$$

To visualise the coherent flow structures of the vortex regions within the fluid, the Q-criterion is computed from the velocity field and visualised for isosurfaces of Q (Hunt *et al.*, 1988). A value of $Q > 0$ defines a region of a vortex, where the magnitude of vorticity exceeds the shear strain rate. This criterion makes the coherent vortical regions within the fluid domain clearly visible. Figure B.5 shows the u-velocity component and the isosurfaces of Q for the non-rotating and rotating case of $Ro = 1$. The value of Q is defined as

$$Q = \frac{1}{2}\left(\|\boldsymbol{\Omega}\|^2 - \|\boldsymbol{S}\|^2\right), \tag{B.28}$$

where $\boldsymbol{S}$ and $\boldsymbol{\Omega}$ are respectively the symmetric and antisymmetric parts of $\nabla\boldsymbol{u}$ with the Euclidean matrix norm given by $\|\boldsymbol{\Omega}\| = \left[tr(\boldsymbol{\Omega}\boldsymbol{\Omega}^t)\right]^{1/2}$, $\|\boldsymbol{S}\| = \left[tr(\boldsymbol{S}\boldsymbol{S}^t)\right]^{1/2}$ (Jeong & Hussain, 1995). The vortices in the Taylor-Green vortex flow were visualised for isosurfaces of $Q = 0.01$ and coloured by the normalised vorticity in the axis of rotation, $\boldsymbol{\omega} \cdot \hat{\boldsymbol{e}}_\Omega / \|\boldsymbol{\omega}\|$.

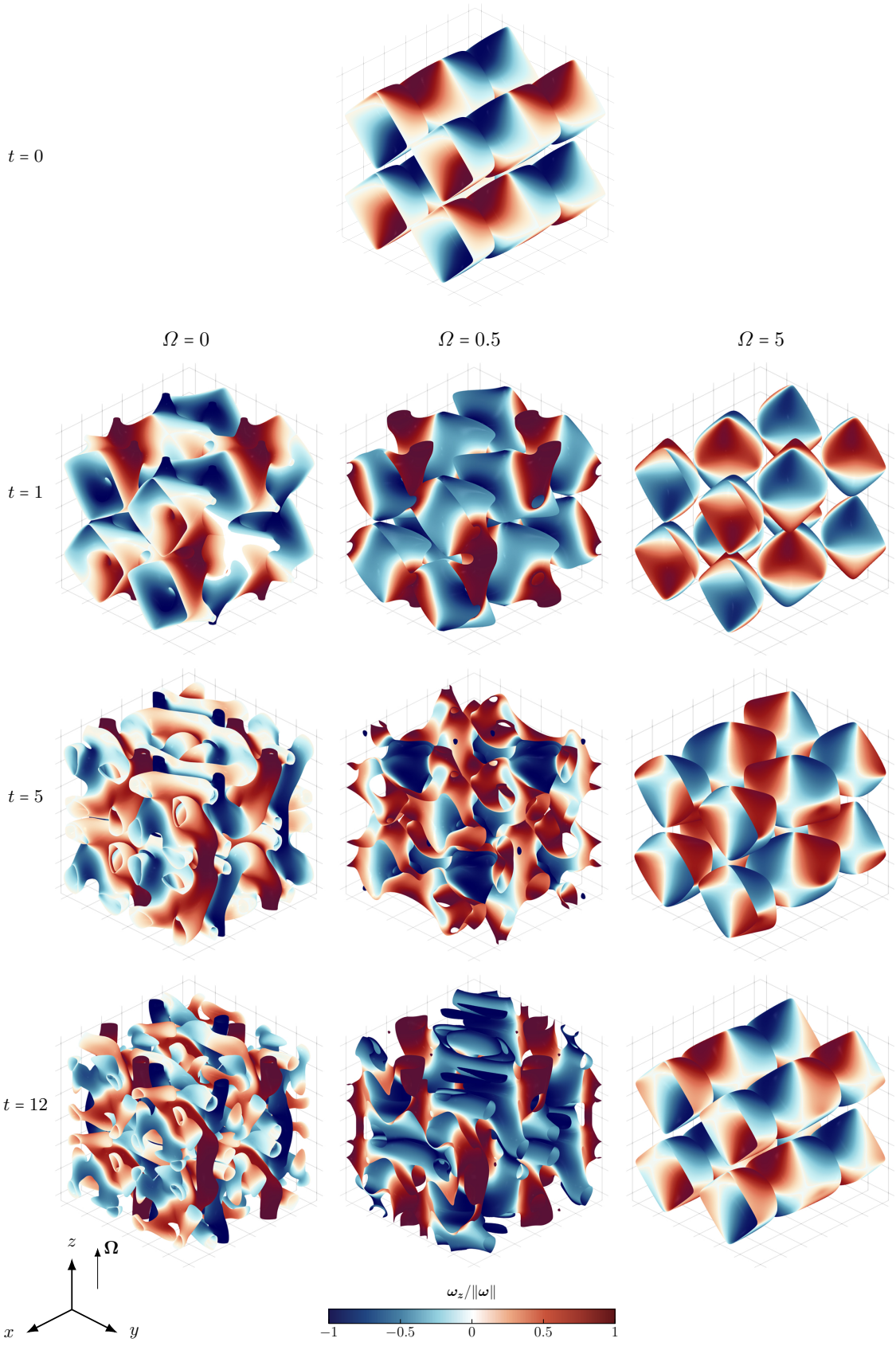

Figure B.5: Three-dimensional Taylor-Green vortex visualisation in the triply periodic domain $[-\pi, \pi]^3$ rotating about the z axis. Isocontours of the Q-criterion for $Q = 0.01$ are coloured by the instantaneous normalised vertical vorticity component $\omega_z/\|\boldsymbol{\omega}\|$. On the top row, the initial condition of the flow field for all cases is shown. The columns from left to right represent three simulation cases with increasing rate of rotation ($\Omega = 1/(2Ro)$) for a $Re = 100$ and the rows indicate three different instances in time. On the left column, the traditional non-rotating Taylor-Green vortex demonstrates gradual increase in turbulent structures. The middle column shows the fluid behaviour for the rotating case of $Ro = 1$, showing similar turbulent structure evolution with time. A repeatable overturning behaviour is observed on the rightmost column for $Ro = 0.1$, where the turbulent structure evolution found in the left two columns is not observed in the rightmost column for the simulated time.

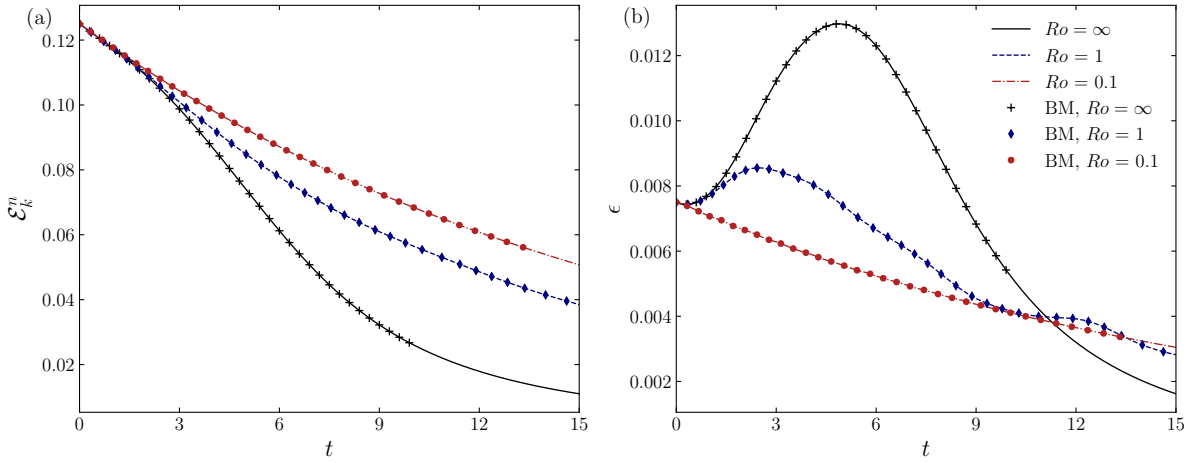

Figure B.6: The volume-averaged kinetic energy (a) and kinetic energy dissipation rate (b) of the Taylor-Green vortex problem. The colour and line styles used for both figures are found in (b). Three cases are considered: 1) non-rotating ($Ro = \infty$) denoted by a solid line, 2) Slow rotation with $Ro = 1$ denoted by a dashed line, and rapid rotation with $Ro = 0.1$ denoted by a dashed-dotted line. The benchmark results (BM) are shown with markers only with the same colour as the simulation results. Note that our simulations are run to $t = 15$, whereas the benchmark data varies between 10 and 14 seconds.

The evolution of kinetic energy and the kinetic energy dissipation rate of all simulations are shown below in Figure B.6. The initial kinetic energy for each problem has an identical magnitude of approximately 0.125 as the initial conditions are identical for all simulations, shown on the left hand side of Figure B.6. Following the temporal evolution of the kinetic energy, it is clear that the non-rotating case shows a more rapid decay, followed by the slowest rotation case of $Ro = 1$, with the lowest energy decay for the highest rotation rate case of $Ro = 0.1$. This difference in rate of decay is also supported in the dissipation rate shown on the right hand side. With the introduction of rotation, the fluid is becoming more organised and thereby inhibiting the isotropic decay of energy (Teitelbaum & Mininni, 2011; Van Bokhoven *et al.*, 2008). As rotation organises the flow, the cascading mechanism of dissipation of energy through smaller scales is becoming more restrained with increasing rotational strength. This causes an overall slower dissipation of energy as shown in the figure above. Naturally, the relation between the kinetic energy and its dissipation rate (i.e., time derivative of kinetic energy) must dictate that any difference observed in one of the two parameters must be visible in both curves. Comparing the Nek5000 solutions with the benchmark, the evolution of the simulated results show similar behaviour across the full simulation periods. That is, there is no apparent time lag in kinetic energy or dissipation rate evolutions, nor are there any apparent differences in magnitudes of the two solution variables. Furthermore, there is no visible divergence between the Nek5000 and the benchmark solutions near the end of the simulation periods, indicating an overall similar evolution of the two parameters from the initial conditions without indication of deviations at later instances in time. The implementation of Coriolis force is hence validated to be correctly implemented in the Nek5000 model.

B.3. Modelling rotating convection in a spherical shell

Here, we test the numerical model for a rotating spherical shell with convection under the Boussinesq approximation. To accomplish this we define a numerical domain of a spherical shell in Section B.3.1 and the appropriate initial and boundary conditions in Section B.3.2. The results of Amit *et al.* (2020), as shown in the respective paper's Table 2, were used for comparison in this section. Amit *et al.* (2020) uses the pseudo-spectral code MagIC (http://magic-sph.github.io/) to solve the problem in a spherical domain. It must be stressed that the respective comparison data is not tested or nor validated and is shall hence only be considered as a reference dataset in this section, as opposed to thoroughly tested industry-standard benchmarks (e.g., Christensen *et al.*, 2001). For convenience, we repeat the problem of rotating convection in a spherical shell as explained in Section 2.2.1.

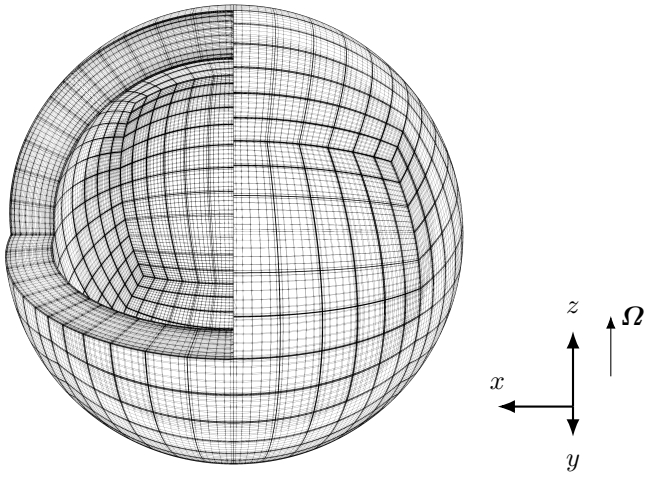

Figure B.7: Numerical domain of a cubed-sphere, spherical shell with 10 radial and 864 horizontal elements with polynomial order 7 for radius ratio $\chi = 0.8$.

B.3.1. Meshing of fluid domain

To simulate a fluid in a SEM, a numerical domain comprising of individual elements must be defined in which the governing equations describing a fluid must be solved; a mesh. In other words, the continuous medium of the fluid must be described by a finite set of elements/gridpoints to simulate the problem. It must be noted that the SEM implemented in Nek5000 only accepts the two-dimensional quadrilateral and three-dimensional hexahedral type elements in its mesh. The former is a simple cell with 4 sides (e.g., a 2D square), and the latter is given by a polyhedron comprising 6 faces, 8 vertices and 12 edges (e.g., a cube). For domains described by simple shapes (e.g., square, box, cylinder, etc.), Nek5000 provides a tool to generate a two or three-dimensional mesh. Given the limited options of element types, discretising a spherical shell x longitudinal and y latitudinal elements, like alternative pseudo-spectral codes, is not possible at the poles as the shape of these three-dimensional elements are not conforming the hexahedral type. Hence, a cubed-sphere grid mesh form the basis for a numerical mesh of a spherical shell domain. This cubed-sphere grid is the projection of a cube, with conformal hexahedral/quadrilateral type elements, to a sphere (see Figure B.7). In this thesis, we considered several meshing software candidates to create such a numerical domain: Ansys ICEM CFD (https://www.ansys.com/), PyMesh (https://pymesh.readthedocs.io/) and GMSH (https://gmsh.info/). All of the aforementioned candidates could be utilsed to create the desired mesh. Despite previous efforts in testing the prior mentioned methods, Vormann & Hansen (2018, 2020) developed a script exclusively for Nek5000 to create the cubed-sphere domain for a spherical shell with arbitrary radius ratio $\chi = r_i/r_o$ (https://github.com/jvormann/Nek5000-Cubed-Sphere). Hence, we exclusively used this latter method for the simulation in spherical shells. Figure B.7 shows the fluid domain for a general spherical shell model containing 8640 elements in total. As visible in Figure B.7, the density of elements/gridpoints in the radial direction is densest near the inner and outer boundaries to support the higher resolution requirements for boundary layer formations. Any deformations from a uniform shell to accommodate the non-uniform shape are handled inside Nek5000 routines by means of a linear coordinate transformation.

B.3.2. Initial and boundary conditions

Boundary and initial conditions are required to fully define the problem and determine the initial state and interaction with the boundaries of the domain. In this study, we have only considered periodic and mechanical (no-slip) boundary conditions. The former connects boundaries to artificially model a domain of infinite extent (e.g., plane layer Rayleigh-Bénard convection in Section B.2.1) and the latter describes that the boundary acts as a wall where flow velocity vanishes, $\boldsymbol{u} = 0$. The boundary conditions chosen for the spherical shell geometry are no-slip, $\boldsymbol{u} = 0$, where the flow velocity vanishes at the inner and outer boundaries and thus simulate physical boundary layers that are valid for a subsurface ocean with bottom sea-floor and an upper ice mantle. It is noted that simulated boundary layers substantially overestimate the geophysical boundary layer thicknesses as the viscosity of the fluid is several orders of

magnitude higher than the geophysical magnitudes (Glatzmaier, 2002).

The initial state of the fluid is imposed for a static fluid $\boldsymbol{u} = 0$, where only the temperature field is to be found from the heat Equation B.38. For a spherically symmetric, uniform shell, the conductive initial temperature profile only depends on the radius. Solving the Laplacian of the temperature field in spherical coordinates gives

$$\frac{d}{dr}\left(r^2 \frac{dT(r)}{dr}\right) = 0 \tag{B.29}$$

and imposing isothermal boundary conditions

$$T(r_i) = 1, \quad T(r_o) = 0 \tag{B.30}$$

yields the temperature profile

$$T(r) = \frac{r_i}{D}\left(\frac{r_o}{r} - 1\right). \tag{B.31}$$

We calculate the conductive temperature profile of the non-uniform domain using the numerical approach. As the numerical domain is projected from a uniform shell to a non-uniform shell, the uniform conductive temperature profile is similarly projected unto the non-uniform grid using the deformation function 2.6. A conductive profile is then found for the non-uniform shell by simulating a fully conductive model (i.e., $Ra = 0 < Ra_c$) until the solution is fully converged.

We follow the implementation of the magnetohydrodynamics MagIC code (http://magic-sph.github.io/) for spherical shell geometries to perturb a conductive temperature field. MagIC uses spherical harmonics to perturb the initial state of the temperature field to initiate unstable convection modes. The perturbation is applied with a radially dependent function

$$T_p(r) = 1 - 3x^2 + 3x^4 - x^6, \tag{B.32}$$

with

$$x = 2r - r_o - r_i, \tag{B.33}$$

where r_i and r_o denote the inner and outer shell radii. In this formulation, a maximum perturbation amplitude is applied at half the ocean shell (i.e., $r = r_i + D/2$) and a zero amplitude at the ocean boundaries. Finally, the profile of the temperature perturbation is defined using the spherical harmonic Y_l^m of degree l and order m (e.g., Arfken *et al.*, 2013) and is given by

$$Y_l^m(\vartheta, \varphi) = \left(\frac{2l}{4\pi}\frac{(l-|m|)!}{(l+|m|)!}\right)^{1/2} P_l^m(\cos\vartheta)\,\Re(e^{Im\varphi}), \tag{B.34}$$

where P_l^m is the associated Legendre polynomial function and $\Re$ the real part of the complex term. This function is multiplied with the perturbation amplitude function in Equation B.32 and the unperturbed conductive temperature field T_c to obtain the temperature perturbation from a solution that satisfies the governing equations. The initial temperature field at $t = 0$ is therefore the sum of the unperturbed temperature profile and the perturbation thereof, which yields

$$T(r) = T_c(r)\left[1 + A \cdot T_p(r)\, Y_l^m(\vartheta, \varphi)\right], \tag{B.35}$$

with A denoting the perturbation amplitude.

B.3.3. A test case of rotating spherical shell convection

We simulate thermal convection of a Boussinesq fluid in a uniform spherical shell rotating with constant rotation rate about $\boldsymbol{\Omega} = \Omega\hat{\boldsymbol{e}}_z$ (see Figure 2.1(a)). The fluid is contained between the inner radius r_i and outer radius r_o, where the radius ratio is defined by $\chi = r_i/r_o$. Gravity is assumed to vary linearly between the bounding radii, normalised by the outer radius surface gravity g_o, such that $\boldsymbol{g} = -(g_o/r_o)\boldsymbol{r}$. The boundaries are impenetrable, no slip and isothermal with an imposed unstable gradient ΔT between the boundaries. It must be noted that the reference dataset does not specify the use of no-slip or stress-free boundary conditions which is discussed hereafter with the findings. The governing Boussinesq equations are non-dimensionalised in length, temperature and time by the shell thickness $D = r_o - r_i$, superadiabatic temperature gradient ΔT and rotation period Ω^{-1} respectively. This results in

$$\frac{\partial \boldsymbol{u}}{\partial t} + \boldsymbol{u}\cdot\nabla\boldsymbol{u} + 2\,\hat{\boldsymbol{e}}_z \times \boldsymbol{u} = -\nabla P + Ek\nabla^2\boldsymbol{u} + Ra^*\frac{\boldsymbol{r}}{r_o}T, \tag{B.36}$$

$$\nabla \cdot \boldsymbol{u} = 0, \tag{B.37}$$

$$\frac{\partial T}{\partial t} + \boldsymbol{u} \cdot \nabla T = \frac{Ek}{Pr} \nabla^2 T. \tag{B.38}$$

The non-dimensional Ekman, modified Rayleigh and Prandtl numbers are introduced, expressed by

$$Ek = \frac{\nu}{\Omega D^2}, \quad Ra^* = \frac{\alpha g_o \Delta T}{\Omega^2 D}, \quad Pr = \frac{\nu}{\kappa}, \tag{B.39}$$

where ν is the kinematic viscosity, κ the thermal diffusivity, α the thermal expansion coefficient, g_o gravitational acceleration at r_o. The modified Rayleigh number is related to the traditional Rayleigh number ($Ra = \alpha g_o \Delta T D^3 / \nu\kappa$) and convective Rossby number by

$$Ra^* = Ra Ek^2 Pr^{-1} = Ro_c^2. \tag{B.40}$$

To compare diagnostics, we record the Reynolds and Rossby numbers, given by

$$Re = \frac{\hat{U} D}{\nu} = \frac{U^{rms}}{Ek}, \quad Ro = \frac{\hat{U}}{\Omega D} = U^{rms}, \tag{B.41}$$

where $\hat{U}$ is the dimensional characteristic velocity, U^{rms} the characteristic non-dimensional rms velocity defined as

$$U^{\mathrm{rms}} = \left(V^{-1} \int_V \overline{\boldsymbol{u} \cdot \boldsymbol{u}} \, dV \right)^{1/2}. \tag{B.42}$$

Further, the advection time is used to physically quantify the time duration for a fluid parcel to traverse distance D with typical velocity U^{rms}. For this analysis, we simulated cases 1 and 3 of Table 2 from Amit *et al.* (2020). That is, case 1 is characterised by $\chi = 0.7$, $Ek = 10^{-3}$, $Ra = 2 \times 10^5$, and case 3 is characterised by $\chi = 0.8$, $Ek = 10^{-3}$, $Ra = 10^6$. Both simulations have a Prandtl number of 1. The pseudo-spectral code MagIC handles the numerical domain differently than Nek5000. MagIC solves the domain in terms of spherical harmonic degrees up to order l_{max} in longitude and latitude, and Chebyshev polynomials in the radial direction. For each radial level, the spherical grid is defined by at least $N_\varphi = 2l_{\max} + 1$, where generally the relation $N_\varphi = 2N_\vartheta$ is used, with N_φ and N_ϑ indicating the number of grid points in longitude and latitude respectively. Further, the numerical resolution may also be described by $l_{\max} = [\min(2N_\vartheta, N_\varphi) - 1]/3$ in order prevents aliasing errors in the simulation. We assume that the latter definition is used, as it describes a higher resolution estimate of the reference dataset. For both cases, Amit *et al.* (2020) uses $l_{\max} = 64$ and 49 radial grid points. Our numerical domain is defined by a cube projected onto a spherical surface (see Section B.3.1), where we use 10 elements in the radial direction and 864 in horizontal direction, with polynomial order of 7. For comparison, our model has 71 radial grid points compared to the 49 used in the reference dataset and we have in total $\approx 3 \times 10^6$ unique gridpoints, compared to the estimated $\approx 9 \times 10^5$ number of unique gridpoints in the reference dataset.

The temporal evolution of the Reynolds number is shown for both simulations in Figure B.8. We average the Reynolds and Rossby numbers after the initial transient until the end of the simulation time: $\tau_a \geq 20$ and $\tau_a \geq 40$ for case 1 and 3 respectively. We estimate the Reynolds and Rossby numbers for case 1 at 40.5 and 0.0405, compared to Amit's estimate of 40 and 0.04. Our estimate of Case 3 is respectively 155.7 and 0.1557 for Reynolds and Rossby numbers, where Amit *et al.* (2020) found the values of 170 and 0.017. As Amit *et al.* (2020) provides only integer values of the physical numbers, we can state that we have found similar results for Case 1, but observe a 9% difference between the Reynolds and Rossby numbers for Case 3. The cause for this notable discrepancy is most likely explained by the uncertainty of mechanical boundary condition used or the difference in numerical resolution between our model and that of Amit *et al.* (2020). Stress-free boundary conditions allow the fluid to have a non-zero tangential velocity at the boundary given by (Livermore *et al.*, 2016)

$$u_r = \frac{\partial}{\partial r}\left(\frac{u_\vartheta}{r}\right) = \frac{\partial}{\partial r}\left(\frac{u_\varphi}{r}\right), \tag{B.43}$$

where u_r, u_ϑ and u_φ are the radial, meridional and zonal velocity components. Because of this condition, viscous dissipation near the boundaries is much lower than no-slip conditions and fluid velocities near the boundary can be substantially larger. This increases the bulk fluid velocity, U^{rms}, accordingly and thus leads to larger Reynolds estimates (see Equation B.41). Contrarily or additionally, resolution

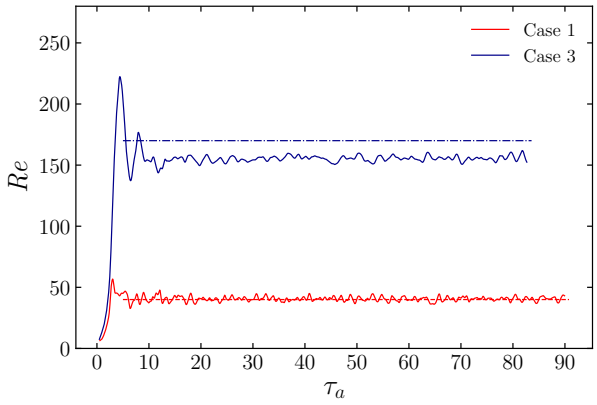

Figure B.8: Reynolds number behaviour for two cases compared to estimates from Amit *et al.* (2020) found in their Table 2 with the same case naming convention. Time is given in terms of advection time units τ_a. The simulated results of our model are denoted by solid lines and that of Amit *et al.* (2020) by dashed-dotted lines of the same colour. The respective estimates from Amit *et al.* (2020) are 40 and 170 for cases 1 and 3.

plays an important variable into sufficiently resolving the smallest length scales that still affect the diagnostic estimations (e.g., Stevens *et al.*, 2010). Gastine *et al.* (2016) simulated a similar model with the same Ekman and Rayleigh numbers, except with a different radius ratio of $\chi = 0.6$ and a quadratic gravity profile $g \sim 1/r^2$. These authors validated the resolution by comparing numerical and analytical expressions of the thermal and viscous dissipation rates which were possible because of this quadratic gravity profile. In that study, the resolution is substantially higher compared to the reference dataset with a maximum harmonic degree of 133 and radial grid points of 81, compared to respectively the 64 and 49 maximum degree and radial grid points employed in Amit *et al.* (2020). Further, Amit *et al.* (2020) estimated Reynolds number indicates higher velocity and thus higher kinetic energy in the system. Based on this, the difference in Reynolds and Rossby estimates for case 3 could further be attributed to under-resolved models for both our simulations and that of Amit *et al.* (2020), such that no accurate comparison could be made. We continue the comparison with the outer boundary heat flux anomaly with respect to the mean heat flux as done in Amit *et al.* (2020), given by

$$\langle \overline{q} \rangle_\vartheta^a = \langle \overline{q} \rangle_\vartheta - \langle \overline{q} \rangle_s \tag{B.44}$$

where the time and zonally averaged heat flux $\langle \overline{q} \rangle_\vartheta$ is vertically offset by the time and surface averaged heat flux $\langle \overline{q} \rangle_s$ (see Section 2.2.5 for description of notations used). Figure B.9 shows the simulated heat flux anomaly curves including the reference curves from Amit *et al.* (2020). This reference data has been extracted using WebPlotDigitizer (https://automeris.io/WebPlotDigitizer). The time and zonally averaged heat flux at the outer boundary $r = r_o$ compares very well with our results and display similar behaviour with variable latitude. That is, for Case 1, the highest heat flux is found at the equator that slowly levels off in magnitude towards the poles. Only minor differences can be spotted with respect to the reference data, as indicated by a slightly higher peak heat flux amplitude for instance. Nonetheless, key spatially dependent characteristics of the outer boundary heat are reproduced in our model. Case 3 shows a polar opposite scenario, where the heat flux is highest at the poles, has two minima near the tangent cylinder (denoted by the vertical dashed lines) and a local maxima at the equator. Here, a larger deviation is also spotted where our model does not reproduce the same contrast of heat flux amplitudes. That is, the minima have a more positive value and the maxima have a less positive value compared to the reference data. This could suggest a less well-resolved thermal boundary layer for the model of Amit *et al.* (2020) where more heat can be transported to the boundary as the motion of the convecting fluid is not sufficiently dissipated (Stevens *et al.*, 2010). Nevertheless, our model does find similar spatial features as the reference dataset where the polar regions are more effective in transfer of heat and the equatorial region, as demarcated by the tangent cylinder, is more inhibited in heat transfer.

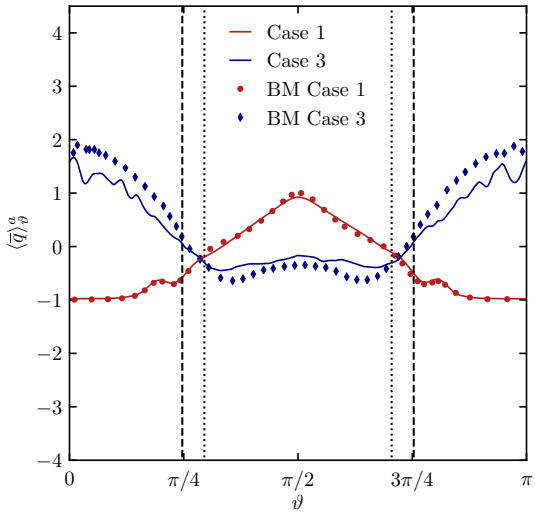

Figure B.9: Heat flux anomaly profiles $\langle\overline{q}\rangle^a_\vartheta$ (see Equation B.44) for the outer boundary $r = r_o$ against the colatitude ϑ. Simulated heat flux profiles are denoted by solid lines and extracted reference data from Amit *et al.* (2020) are denoted by the same coloured symbols obtained using WebPlotDigitizer (https://automeris.io/WebPlotDigitizer). The vertical lines denote the tangent cylinder angles $\vartheta_t = \sin^{-1}(\chi)$ for $\chi = 0.7$ with dashed lines and for $\chi = 0.8$ with dotted lines.

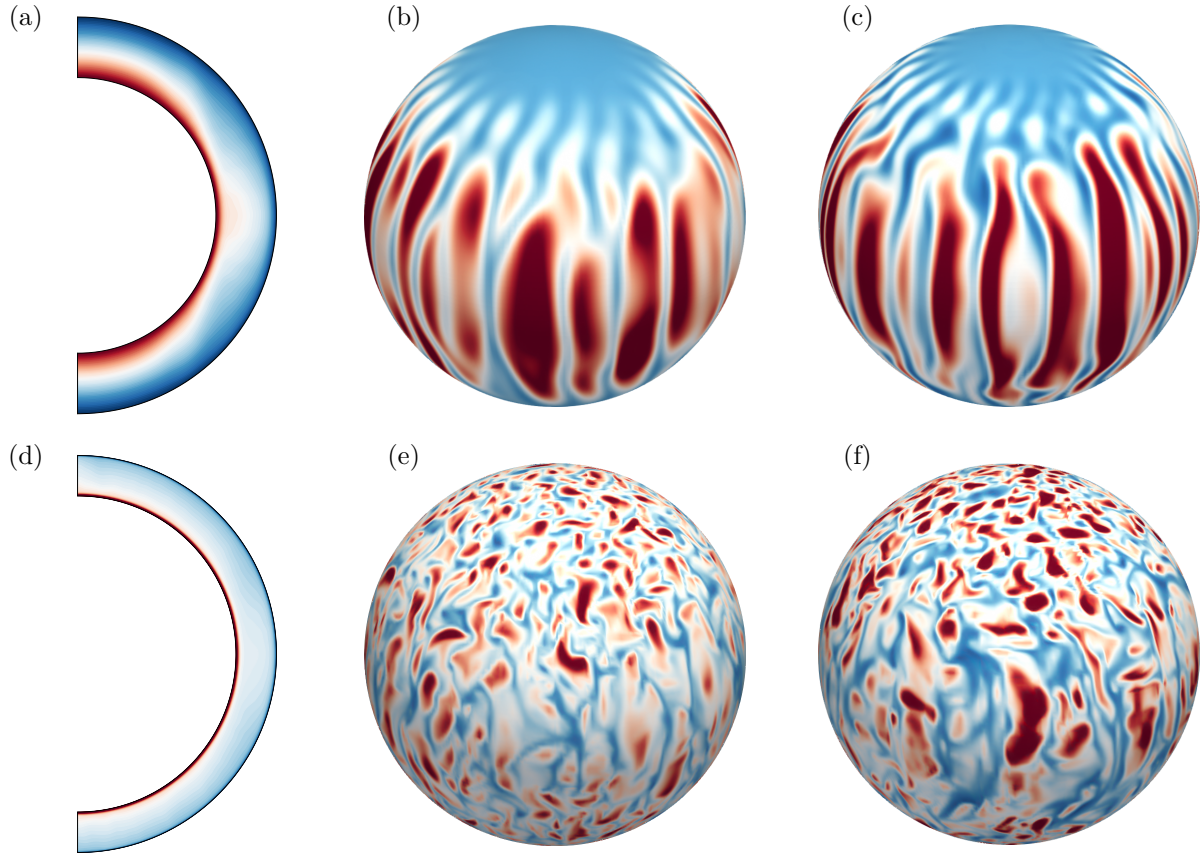

Figure B.10: Zonally and time averaged temperature field (a,d) and inner (b,e) and outer (c,f) boundary heat flux fields. Results of Case 1 is shown on the first row and Case 3 is shown on the second row. Similar to Amit *et al.* (2020), we visualise the heatflux anomaly from the mean heat flux in the two right columns where red denotes positive and blue negative heat flux with respect to the mean (i.e., white). The mean heat flux at the boundaries is computed using the time averaged Nusselt number: $\langle\overline{q}\rangle_s = Nu \cdot q_c/4\pi r^2$, where q_c is the conductive heat flux at the boundary and r is the inner or outer radius. We find the surface integrated conductive heat flux by using Equation B.31 and $q_c = \int_S dT/dr\, dS$ (e.g., see Equation 2.11)

Finally, Figure B.10 shows a selection of figures to visualise the internal temperature profile and inner and outer boundary heat flux anomalies. The first row shows case 1, which clearly favours convective flows near the equatorial and mid-latitude region. The heat flux anomaly fields for case 1 demonstrate the columnar structures aligned with the axis of rotation and inhibited flows at the polar regions. Case 3 on the other hand shows a very turbulent fluid with a nearly isothermalised interior where the temperature gradients are highest near the inner and outer boundaries in (d). Further, the heat flux anomalies show a more chaotic behaviour at the surface boundaries, showing that the increased thermal forcing (i.e., higher Ra) is less affected by the Coriolis force.

Bibliography

Al-Shamali, F., Heimpel, M. & Aurnou, J. 2004 Varying the spherical shell geometry in rotating thermal convection. *Geophysical & Astrophysical Fluid Dynamics* **98** (2), 153–169.

Amit, H., Choblet, G., Tobie, G., Terra-Nova, F., Čadek, O. & Bouffard, M. 2020 Cooling patterns in rotating thin spherical shells — application to titan's subsurface ocean. *Icarus* **338**, 113509.

Amit, H., Deschamps, F. & Choblet, G. 2015 Numerical dynamos with outer boundary heat flux inferred from probabilistic tomography—consequences for latitudinal distribution of magnetic flux. *Geophysical Journal International* **203** (2), 840–855.

Arfken, G. B., Weber, H. J. & Harris, F. E. 2013 *Mathematical methods for physicists a comprehensive guide.*. Amsterdam (Holanda) Elsevier.

Aurnou, J., Heimpel, M., Allen, L., King, E. & Wicht, J. 2008 Convective heat transfer and the pattern of thermal emission on the gas giants. *Geophysical Journal International* **173** (3), 793–801.

Aurnou, J., Heimpel, M. & Wicht, J. 2007 The effects of vigorous mixing in a convective model of zonal flow on the ice giants. *Icarus* **190** (1), 110–126.

Aurnou, J. M. & Olson, P. L. 2001 Strong zonal winds from thermal convection in a rotating spherical shell. *Geophysical research letters* **28** (13), 2557–2559.

Baland, R.-M., Tobie, G., Lefèvre, A. & Van Hoolst, T. 2014 Titan's internal structure inferred from its gravity field, shape, and rotation state. *Icarus* **237**, 29–41.

Batchelor, C. K. & Batchelor, G. 2000 *An introduction to fluid dynamics*. Cambridge university press.

Béghin, C., Randriamboarison, O., Hamelin, M., Karkoschka, E., Sotin, C., Whitten, R. C., Berthelier, J.-J., Grard, R. & Simões, F. 2012 Analytic theory of titan's schumann resonance: Constraints on ionospheric conductivity and buried water ocean. *Icarus* **218** (2), 1028–1042.

Béghin, C., Sotin, C. & Hamelin, M. 2010 Titan's native ocean revealed beneath some 45 km of ice by a schumann-like resonance. *Comptes Rendus Geoscience* **342** (6), 425–433.

Beuthe, M., Rivoldini, A. & Trinh, A. 2016 Enceladus's and dione's floating ice shells supported by minimum stress isostasy. *Geophysical Research Letters* **43** (19), 10–088.

Bills, B. G. & Nimmo, F. 2008 Forced obliquity and moments of inertia of titan. *Icarus* **196** (1), 293–297.

Bruzzone, L., Plaut, J. J., Alberti, G., Blankenship, D. D., Bovolo, F., Campbell, B. A., Ferro, A., Gim, Y., Kofman, W., Komatsu, G. & others 2013 Rime: Radar for icy moon exploration. In *2013 IEEE International geoscience and remote sensing symposium-IGARSS*, pp. 3907–3910. IEEE.

Busse, F. 1994 Convection driven zonal flows and vortices in the major planets. *Chaos: An Interdisciplinary Journal of Nonlinear Science* **4** (2), 123–134.

Busse, F. 2002 Convective flows in rapidly rotating spheres and their dynamo action. *Physics of fluids* **14** (4), 1301–1314.

Busse, F. & Cuong, P. 1977 Convection in rapidly rotating spherical fluid shells. *Geophysical & Astrophysical Fluid Dynamics* **8** (1), 17–41.

Čadek, O., Souček, O., Běhounková, M., Choblet, G., Tobie, G. & Hron, J. 2019 Long-term stability of enceladus' uneven ice shell. *Icarus* **319**, 476–484.

Čadek, O., Tobie, G., Van Hoolst, T., Massé, M., Choblet, G., Lefèvre, A., Mitri, G., Baland, R.-M., Běhounková, M., Bourgeois, O. & others 2016 Enceladus's internal ocean and ice shell constrained from cassini gravity, shape, and libration data. *Geophysical Research Letters* **43** (11), 5653–5660.

Canuto, C., Hussaini, M. Y., Quarteroni, A. & Zang, T. A. 2007 *Spectral methods: evolution to complex geometries and applications to fluid dynamics*. Springer Science & Business Media.

Castaing, B., Gunaratne, G., Heslot, F., Kadanoff, L., Libchaber, A., Thomae, S., Wu, X.-Z., Zaleski, S. & Zanetti, G. 1989 Scaling of hard thermal turbulence in rayleigh-bénard convection. *Journal of Fluid Mechanics* **204**, 1–30.

Cébron, D., Le Bars, M., Leontini, J., Maubert, P. & Le Gal, P. 2010*a* A systematic numerical study of the tidal instability in a rotating triaxial ellipsoid. *Physics of the Earth and Planetary Interiors* **182** (1-2), 119–128.

Cébron, D., Maubert, P. & Le Bars, M. 2010*b* Tidal instability in a rotating and differentially heated ellipsoidal shell. *Geophysical Journal International* **182** (3), 1311–1318.

Chandrasekhar, S. 1961 *Hydrodynamic and hydromagnetic stability*. Oxford: Oxford University Press.

Cheng, J. S., Aurnou, J. M., Julien, K. & Kunnen, R. P. 2018 A heuristic framework for next-generation models of geostrophic convective turbulence. *Geophysical & Astrophysical Fluid Dynamics* **112** (4), 277–300.

Cheng, J. S., Stellmach, S., Ribeiro, A., Grannan, A., King, E. M. & Aurnou, J. M. 2015 Laboratory-numerical models of rapidly rotating convection in planetary cores. *Geophysical Journal International* **201** (1), 1–17.

Choblet, G., Tobie, G., Sotin, C., Běhounková, M., Čadek, O., Postberg, F. & Souček, O. 2017*a* Powering prolonged hydrothermal activity inside enceladus. *Nature Astronomy* **1** (12), 841–847.

Choblet, G., Tobie, G., Sotin, C., Kalousova, K. & Grasset, O. 2017*b* Heat transport in the high-pressure ice mantle of large icy moons. *Icarus* **285**, 252–262.

Christensen, U., Aubert, J., Cardin, P., Dormy, E., Gibbons, S., Glatzmaier, G., Grote, E., Honkura, Y., Jones, C., Kono, M. & others 2001 A numerical dynamo benchmark. *Physics of the Earth and Planetary Interiors* **128** (1-4), 25–34.

Cockell, C., Bush, T., Bryce, C., Direito, S., Fox-Powell, M., Harrison, J., Lammer, H., Landenmark, H., Martin-Torres, J., Nicholson, N., Noack, L., O'Malley-James, J., Payler, S., Rushby, A., Samuels, T., Schwendner, P., Wadsworth, J. & Zorzano, M. 2016 Habitability: a review. *Astrobiology* **16** (1), 89–117.

Collins, G., Head III, J., Pappalardo, R. & Spaun, N. 2000 Evaluation of models for the formation of chaotic terrain on europa. *Journal of Geophysical Research: Planets* **105** (E1), 1709–1716.

Collins, G. C. & Goodman, J. C. 2007 Enceladus' south polar sea. *Icarus* **189** (1), 72–82.

Davidson, P. A. 2013 *Turbulence in rotating, stratified and electrically conducting fluids*. Cambridge University Press.

Deville, M. O., Fischer, P. F., Fischer, P. F., Mund, E. & others 2002 *High-order methods for incompressible fluid flow*, , vol. 9. Cambridge university press.

Dietrich, W., Hori, K. & Wicht, J. 2016 Core flows and heat transfer induced by inhomogeneous cooling with sub-and supercritical convection. *Physics of the Earth and Planetary Interiors* **251**, 36–51.

Dormy, E., Soward, A., Jones, C., Jault, D. & Cardin, P. 2004 The onset of thermal convection in rotating spherical shells. *Journal of Fluid Mechanics* **501**, 43.

Elsasser, W. M. 1939 On the origin of the earth's magnetic field. *Physical Review* **55** (5), 489.

Evonuk, M. 2015 Convection in deformed bodies: The effect of equatorial ellipticity on convective behavior. *Earth and Planetary Science Letters* **430**, 249–259.

Favier, B., Guervilly, C. & Knobloch, E. 2019*a* Subcritical turbulent condensate in rapidly rotating rayleigh–bénard convection. *Journal of Fluid Mechanics* **864**, R1.

Favier, B., Purseed, J. & Duchemin, L. 2019*b* Rayleigh–bénard convection with a melting boundary. *Journal of Fluid Mechanics* **858**, 437–473.

Gastine, T., Wicht, J. & Aubert, J. 2016 Scaling regimes in spherical shell rotating convection. *Journal of Fluid Mechanics* **808**, 690–732.

Gastine, T., Wicht, J. & Aurnou, J. M. 2015 Turbulent rayleigh–bénard convection in spherical shells. *Journal of Fluid Mechanics* **778**, 721–764.

Gibbons, S., Gubbins, D. & Zhang, K. 2007 Convection in rotating spherical fluid shells with inhomogeneous heat flux at the outer boundary. *Geophysical and Astrophysical Fluid Dynamics* **101** (5-6), 347–370.

Gilman, P. A. 1977 Nonlinear dynamics of boussinesq convection in a deep rotating spherical shell-i. *Geophysical & Astrophysical Fluid Dynamics* **8** (1), 93–135.

Gissinger, C. & Petitdemange, L. 2019 A magnetically driven equatorial jet in europa's ocean. *Nature Astronomy* **3** (5), 401–407.

Glatzmaier, G. A. 2002 Geodynamo simulations - how realistic are they? *Annual Review of Earth and Planetary Sciences* **30** (1), 237–257.

Glatzmaier, G. A. 2013 *Introduction to modeling convection in planets and stars: Magnetic field, density stratification, rotation*. Princeton University Press.

Glatzmaier, G. A., Evonuk, M. & Rogers, T. M. 2009 Differential rotation in giant planets maintained by density-stratified turbulent convection. *Geophysical and Astrophysical Fluid Dynamics* **103** (1), 31–51.

Goodman, J. C., Collins, G. C., Marshall, J. & Pierrehumbert, R. T. 2004 Hydrothermal plume dynamics on europa: Implications for chaos formation. *Journal of Geophysical Research: Planets* **109** (E3).

Grannan, A., Favier, B., Le Bars, M. & Aurnou, J. M. 2017 Tidally forced turbulence in planetary interiors. *Geophysical Journal International* **208** (3), 1690–1703.

Guervilly, C., Cardin, P. & Schaeffer, N. 2019 Turbulent convective length scale in planetary cores. *Nature* **570** (7761), 368–371.

Hayne, P. O., Christensen, P., Spencer, J., Abramov, O., Howett, C., Mellon, M., Nimmo, F., Piqueux, S. & Rathbun, J. 2017 Possible nature and detectability of endogenic thermal anomalies on europa. In *Lunar and Planetary Science Conference*, , vol. 48.

Heimpel, M., Aurnou, J. & Wicht, J. 2005 Simulation of equatorial and high-latitude jets on jupiter in a deep convection model. *Nature* **438** (7065), 193–196.

Hemingway, D. J. & Mittal, T. 2019 Enceladus's ice shell structure as a window on internal heat production. *Icarus* **332**, 111 – 131.

Hunt, J. C., Wray, A. A. & Moin, P. 1988 Eddies, streams, and convergence zones in turbulent flows. , vol. Proceedings of the Summer Program 1988.

Iess, L., Jacobson, R. A., Ducci, M., Stevenson, D. J., Lunine, J. I., Armstrong, J. W., Asmar, S. W., Racioppa, P., Rappaport, N. J. & Tortora, P. 2012 The tides of titan. *Science* **337** (6093), 457–459.

Iess, L., Stevenson, D., Parisi, M., Hemingway, D., Jacobson, R., Lunine, J., Nimmo, F., Armstrong, J., Asmar, S., Ducci, M. & others 2014 The gravity field and interior structure of enceladus. *Science* **344** (6179), 78–80.

Jeong, J. & Hussain, F. 1995 On the identification of a vortex. *Journal of fluid mechanics* **285**, 69–94.

Julien, K., Aurnou, J. M., Calkins, M. A., Knobloch, E., Marti, P., Stellmach, S. & Vasil, G. M. 2016 A nonlinear model for rotationally constrained convection with ekman pumping. *Journal of Fluid Mechanics* **798**, 50–87.

Julien, K., Knobloch, E., Rubio, A. M. & Vasil, G. M. 2012 Heat transport in low-rossby-number rayleigh-bénard convection. *Physical review letters* **109** (25), 254503.

Julien, K., Legg, S., McWilliams, J. & Werne, J. 1996 Rapidly rotating turbulent rayleigh-bénard convection. *Journal of Fluid Mechanics* **322**, 243–273.

Karniadakis, G. & Sherwin, S. 1999 *Spectral/hp element methods for computational fluid dynamics*. Oxford University Press.

Khurana, K., Kivelson, M., Stevenson, D., Schubert, G., Russell, C., Walker, R. & Polanskey, C. 1998 Induced magnetic fields as evidence for subsurface oceans in europa and callisto. *Nature* **395** (6704), 777.

King, E., Stellmach, S. & Buffett, B. 2013 Scaling behaviour in rayleigh–bénard convection with and without rotation. *Journal of Fluid Mechanics* **717**, 449–471.

King, E. M. & Buffett, B. A. 2013 Flow speeds and length scales in geodynamo models: the role of viscosity. *Earth and Planetary Science Letters* **371**, 156–162.

King, E. M., Stellmach, S. & Aurnou, J. M. 2012 Heat transfer by rapidly rotating rayleigh–bénard convection. *Journal of Fluid Mechanics* **691**, 568–582.

King, E. M., Stellmach, S., Noir, J., Hansen, U. & Aurnou, J. M. 2009 Boundary layer control of rotating convection systems. *Nature* **457** (7227), 301–304.

Kvorka, J., Čadek, O., Tobie, G. & Choblet, G. 2018 Does titan's long-wavelength topography contain information about subsurface ocean dynamics? *Icarus* **310**, 149–164.

Lemasquerier, D., Grannan, A., Vidal, J., Cébron, D., Favier, B., Le Bars, M. & Aurnou, J. 2017 Libration-driven flows in ellipsoidal shells. *Journal of Geophysical Research: Planets* **122** (9), 1926–1950.

Liao, Y., Nimmo, F. & Neufeld, J. A. 2020 Heat production and tidally driven fluid flow in the permeable core of enceladus. *Journal of Geophysical Research: Planets* **125** (9), e2019JE006209.

Lissauer, J. J. & De Pater, I. 2013 *Fundamental planetary science: physics, chemistry and habitability*. Cambridge University Press.

Livermore, P. W., Bailey, L. M. & Hollerbach, R. 2016 A comparison of no-slip, stress-free and inviscid models of rapidly rotating fluid in a spherical shell. *Scientific reports* **6**, 22812.

Lobo, A. H., Thompson, A. F., Vance, S. D. & Tharimena, S. 2020 A pole-to-equator ocean overturning circulation on enceladus, arXiv: 2007.06173.

Long, R., Mound, J., Davies, C. & Tobias, S. 2020 Scaling behaviour in spherical shell rotating convection with fixed-flux thermal boundary conditions. *Journal of Fluid Mechanics* **889**.

Melosh, H., Ekholm, A., Showman, A. & Lorenz, R. 2004 The temperature of europa's subsurface water ocean. *Icarus* **168** (2), 498–502.

Miesch, M. S. 2005 Large-scale dynamics of the convection zone and tachocline. *Living Reviews in Solar Physics* **2** (1), 1.

Mitri, G., Meriggiola, R., Hayes, A., Lefevre, A., Tobie, G., Genova, A., Lunine, J. I. & Zebker, H. 2014 Shape, topography, gravity anomalies and tidal deformation of titan. *Icarus* **236**, 169–177.

Mound, J. E. & Davies, C. J. 2017 Heat transfer in rapidly rotating convection with heterogeneous thermal boundary conditions. *Journal of Fluid Mechanics* **828**, 601–629.

Murray, C. D. & Dermott, S. F. 1999 *Solar system dynamics*. Cambridge university press.

NEK5000 2019 Version 19.0. 28 december 2019. argonne national laboratory, illinois. Available: http://nek5000.mcs.anl.gov.

Nimmo, F. & Pappalardo, R. 2016 Ocean worlds in the outer solar system. *Journal of Geophysical Research: Planets* **121** (8), 1378–1399.

Noir, J. & Cébron, D. 2013 Precession-driven flows in non-axisymmetric ellipsoids. *Journal of Fluid Mechanics* **737**, 412–439.

Olson, P. 2016 Mantle control of the geodynamo: Consequences of top-down regulation. *Geochemistry, Geophysics, Geosystems* **17** (5), 1935–1956.

Pappalardo, R., Vance, S., Bagenal, F., Bills, B., Blaney, D., Blankenship, D., Brinckerhoff, W., Connerney, J., Hand, K., Hoehler, T. M. & others 2013 Science potential from a europa lander. *Astrobiology* **13** (8), 740–773.

Pedlosky, J. 2013 *Geophysical fluid dynamics*. Springer Science & Business Media.

Pestana, T. & Hickel, S. 2019 Regime transition in the energy cascade of rotating turbulence. *Physical Review E* **99** (5), 053103.

Pestana, T. & Hickel, S. 2020 Rossby-number effects on columnar eddy formation and the energy dissipation law in homogeneous rotating turbulence. *Journal of Fluid Mechanics* **885**.

Plumley, M., Julien, K., Marti, P. & Stellmach, S. 2016 The effects of ekman pumping on quasi-geostrophic rayleigh–bénard convection. *Journal of Fluid Mechanics* **803**, 51–71.

Porco, C., Helfenstein, P., Thomas, P., Ingersoll, A., Wisdom, J., West, R., Neukum, G., Denk, T., Wagner, R., Roatsch, T. & others 2006 Cassini observes the active south pole of enceladus. *science* **311** (5766), 1393–1401.

Postberg, F., Kempf, S., Schmidt, J., Brilliantov, N., Beinsen, A., Abel, B., Buck, U. & Srama, R. 2009 Sodium salts in e-ring ice grains from an ocean below the surface of enceladus. *Nature* **459** (7250), 1098.

Postberg, F., Schmidt, J., Hillier, J., Kempf, S. & Srama, R. 2011 A salt-water reservoir as the source of a compositionally stratified plume on enceladus. *Nature* **474** (7353), 620.

Radko, T. 2013 *Double-diffusive convection*. Cambridge University Press.

Rappaport, N. J., Iess, L., Tortora, P., Anabtawi, A., Asmar, S. W., Somenzi, L. & Zingoni, F. 2007 Mass and interior of enceladus from cassini data analysis. *Icarus* **190** (1), 175–178.

Reddy, K. S., Favier, B. & Le Bars, M. 2018 Turbulent kinematic dynamos in ellipsoids driven by mechanical forcing. *Geophysical Research Letters* **45** (4), 1741–1750.

Rovira-Navarro, M., Gerkema, T., Maas, L. R., van der Wal, W., van Ostayen, R. & Vermeersen, B. 2020 Tides in subsurface oceans with meridional varying thickness. *Icarus* p. 113711.

Rovira-Navarro, M., Rieutord, M., Gerkema, T., Maas, L. R., van der Wal, W. & Vermeersen, B. 2019 Do tidally-generated inertial waves heat the subsurface oceans of europa and enceladus? *Icarus* **321**, 126–140.

Shishkina, O. & Wagner, C. 2008 Analysis of sheet-like thermal plumes in turbulent rayleigh-bénard convection. *Journal of Fluid Mechanics* **599**, 383.

Shraiman, B. I. & Siggia, E. D. 1990 Heat transport in high-rayleigh-number convection. *Physical Review A* **42** (6), 3650.

Soderlund, K. M. 2019 Ocean dynamics of outer solar system satellites. *Geophysical Research Letters* **46** (15), 8700–8710.

Soderlund, K. M., Kalousová, K., Buffo, J. J., Glein, C. R., Goodman, J. C., Mitri, G., Patterson, G. W., Postberg, F., Rovira-Navarro, M., Rückriemen, T. & others 2020 Ice-ocean exchange processes in the jovian and saturnian satellites. *Space Science Reviews* **216** (5), 1–57.

Soderlund, K. M., Schmidt, B., Wicht, J. & Blankenship, D. D. 2014 Ocean-driven heating of europa's icy shell at low latitudes. *Nature Geoscience* **7** (1), 16–19.

Spencer, J., Pearl, J., Segura, M., Flasar, F., Mamoutkine, A., Romani, P., Buratti, B., Hendrix, A., Spilker, L. & Lopes, R. 2006 Cassini encounters enceladus: Background and the discovery of a south polar hot spot. *science* **311** (5766), 1401–1405.

Spiegel, E. A. & Veronis, G. 1960 On the boussinesq approximation for a compressible fluid. *The Astrophysical Journal* **131**, 442.

Stellmach, S., Lischper, M., Julien, K., Vasil, G., Cheng, J. S., Ribeiro, A., King, E. M. & Aurnou, J. M. 2014 Approaching the asymptotic regime of rapidly rotating convection: boundary layers versus interior dynamics. *Physical review letters* **113** (25), 254501.

Stevens, R. J., Verzicco, R. & Lohse, D. 2010 Radial boundary layer structure and nusselt number in rayleigh–bénard convection. *Journal of fluid mechanics* **643**, 495–507.

Stevenson, D. J. 2003 Planetary magnetic fields. *Earth and planetary science letters* **208** (1-2), 1–11.

Teitelbaum, T. & Mininni, P. D. 2011 The decay of turbulence in rotating flows. *Physics of Fluids* **23** (6), 065105.

Thomas, P., Tajeddine, R., Tiscareno, M., Burns, J., Joseph, J., Loredo, T., Helfenstein, P. & Porco, C. 2016 Enceladus's measured physical libration requires a global subsurface ocean. *Icarus* **264**, 37–47.

Tu, J., Yeoh, G. H. & Liu, C. 2018 *Computational fluid dynamics: a practical approach*. Butterworth-Heinemann.

Tyler, R. H. 2011 Magnetic remote sensing of europa's ocean tides. *Icarus* **211** (1), 906–908.

Van Bokhoven, L., Cambon, C., Liechtenstein, L., Godeferd, F. S. & Clercx, H. 2008 Refined vorticity statistics of decaying rotating three-dimensional turbulence. *Journal of Turbulence* **9** (9), N6.

Van Hoolst, T., Baland, R.-M. & Trinh, A. 2013 On the librations and tides of large icy satellites. *Icarus* **226** (1), 299–315.

Vance, S. D., Bills, B. G., Cochrane, C. J., Soderlund, K. M., Gómez-Pérez, N., Styczinski, M. J. & Paty, C. S. 2020 Magnetic induction in convecting galilean oceans. *Earth and Space Science Open Archive* p. 45.

Vormann, J. & Hansen, U. 2018 Numerical simulations of bistable flows in precessing spheroidal shells. *Geophysical Journal International* **213** (2), 786–797.

Vormann, J. & Hansen, U. 2020 Characteristics of a precessing flow under the influence of a convecting temperature field in a spheroidal shell. *Journal of Fluid Mechanics* **891**, A15.

Waite Jr, J. H., Lewis, W., Magee, B., Lunine, J., McKinnon, W., Glein, C., Mousis, O., Young, D., Brockwell, T., Westlake, J. & others 2009 Liquid water on enceladus from observations of ammonia and 40 ar in the plume. *Nature* **460** (7254), 487.

Yoshida, M. 2017 On approximations of the basic equations of terrestrial mantle convection used in published literature. *Physics of the Earth and Planetary Interiors* **268**, 11–17.

Zhang, K. 1992 Spiralling columnar convection in rapidly rotating spherical fluid shells. *Journal of Fluid Mechanics* **236**, 535–556.

Zhang, K. & Liao, X. 2017 *Theory and Modeling of Rotating Fluids: Convection, Inertial Waves and Precession*. Cambridge University Press.

Zhang, K.-K. & Busse, F. 1987 On the onset of convection in rotating spherical shells. *Geophysical & Astrophysical Fluid Dynamics* **39** (3), 119–147.

Zimmer, C., Khurana, K. K. & Kivelson, M. G. 2000 Subsurface oceans on europa and callisto: Constraints from galileo magnetometer observations. *Icarus* **147** (2), 329–347.

Zolotov, M. Y. 2007 An oceanic composition on early and today's enceladus. *Geophysical Research Letters* **34** (23).